Fatigue, Fracture, and Environmentally-Assisted Behavior of Advanced Engineering Materials

A Dissertation Presented for the

Doctor of Philosophy

Degree

The University of Tennessee, Knoxville

Zhi Tang

December 2014

Acknowledgements

First and foremost, I would like to express my sincere gratitude to my major advisor, Prof. Peter K. Liaw, for supporting me academically and financially through his patience, motivation, enthusiasm, and encouragement. I would also like to thank the committee members: Prof. Carl D. Lundin, Prof. Carl J. McHargue, and Prof. Hairong Qi, for their considerable efforts and guidance to my Doctor of Science Degree study.

My sincere thanks also go to Dr. Oleg N. Senkov and Dr. Daniel B. Miracle from Air Force Research Laboratory (AFRL), for contributing their immense knowledge and insightful comments to my study. I would like to thank Dr. Chad M. Parish from the Oak Ridge National Laboratory (ORNL) for microstructural characterization research. I am grateful to Dr. Chuan Zhang and Dr. Fan Zhang from CompuTherm LLC. for their thermodynamic calculations research. I also very appreciate Prof. Jien-Wei Yeh and Dr. Che-Wei Tsai for their fatigue mechanism research, and Prof. Tao Yuan from Ohio University for his modeling. I am also grateful to Prof. Fuqian Yang and Dr. Guangfeng Zhao from The University of Kentucky for their nanoindentation research. I would like to thank Mr. Douglas E. Fielden, and his team, Mr. Larry D. Smith and Mr. Dan Hackworth, at The University of Tennessee (UT), for their help in machining the experiment samples in a timely manner. I also greatly appreciate Dr. Jieshan Hou from the Institute of Metal Research in the Chinese Academy of Sciences, Dr. Andrew Chuang from UT for useful discussions, and gratefully acknowledge Mr. Maneel Bharadwaj, Mr. Max Trend, Dr. Joshua Burgess, Mr. John Bohling, Dr. John Dunlap, and Mr. Greg Jones of UT for technical support.

I am indebted to many of my student colleagues for providing a stimulating and fun environment in which to learn and grow. I am especially grateful to Dr. Gongyao Wang, Dr. Lu

Huang, Mr. Lou J. Santodonato, Dr. Andrew Chuang, Dr. Wei Wu, Mr. Qingming Feng, Mr. Zhinan An, Mr. Wei Guo, Mr. Xie Xie, Mr. Haoling Jia, Mr. Michael Hemphill, Mr. Zhiqian Sun, Mr. Bilin Chen, Mr. Gian Song, Ms. Haoyan Diao, Ms. Shuying Chen, Mr. Rui Feng at UT.

I would like to acknowledge the financial support from the US National Science Foundation (DMR-0909037, CMMI-0900271, and CMMI-1100080), the Department of Energy Office of Nuclear Energy's Nuclear Energy University Program (NEUP) 00119262, and the Department of Energy, Office of Fossil Energy, National Energy Technology Laboratory (NETL) DE-FE-0008855.

Lastly and most importantly, I would like to dedicate my thesis to my parents, Dasheng Tang and Qiaohua Wang, for their love, encouragement, and support in all my pursuits.

Abstract

The objective of the present study is to provide a fundamental understanding of fatigue, fracture, and environmentally-assisted behavior of high-entropy alloys (HEAs). The work involves fatigue, fracture, and environmentally-assisted behavior of a new kind of advanced engineering materials, called HEAs. Three tasks are studied: (1) microstructures and fracture mechanisms of HEAs, (2) fatigue failure and life prediction of HEAs, and (3) corrosion and environmentally-assisted behavior of HEAs.

In the first task, microstructural stability and fracture mechanism of the AlCoCrFeNi alloy are studied and compared with thermodynamic calculations. In the second task, high-cycle fatigue-failure mechanisms of the cold-rolled Al0.5CoCrCuFeNi alloy are explored, and the experimental results are used to develop lifetime-prediction capabilities and safety models for future applications. In the third task, a single-phase Al0.3CoCrFeNi alloy is computational-alloyed-designed and developed, and electrochemical-polarization and fatigue-environmentally-assisted behavior are investigated.

Intellectual merit

The current study of fatigue fracture on HEAs advances the fundamental understanding of the mechanisms of the fatigue fracture and environmentally-assisted behavior of HEAs, which is a very new area. The experimental approaches provide the critical information for the mechanistic study of the heat-treatment effects, such as hot isostatic pressing (HIP), annealing, cold rolling, and forging, on microstructures and mechanical properties of HEA systems. This research program have a transformative impact on the research, development, and applications of HEAs. The goal

is accomplished by utilizing the strength at The University of Tennessee (UT)'s mechanical behavior and failure analysis of advanced structural alloys, and materials processing. UT is well equipped with the synthesis equipment, mechanical-testing instruments, and microstructural-characterization tools. The synergetic efforts facilitate the effectiveness and success of the proposal research.

Broader impacts

The current research on fatigue-fracture and environmentally-assisted behavior of HEAs enriches the research and teaching efforts on advanced materials at UT. The presentations at professional conferences and the publications in academic journals achieve the wide national and international impact. The efforts not only increase the public awareness on the fatigue-fracture and environmentally-assisted behavior of HEAs and their scientific importance, but also stimulate the interests of the student in pursuing the science, engineering, and technology fields of study.

Table of Contents

List of Tables

List of Figures

Chapter 1. Objective and Motivation

The objective of the work is to provide a fundamental understanding of fatigue-fracture and environmentally-assisted behavior of high-entropy alloys (HEAs). Fatigue, fracture, and environmentally assisted behavior of advanced engineering materials are very common phenomena in industry and important to be investigated. If advanced engineering materials are used in industry, and the greatest concerns are usually fatigue-related and/or corrosion-associated problems. Therefore, the corrosion and fatigue behavior of advanced engineering materials can be an interesting and critical topic to be studied and characterized with an effective life-prediction model. Meanwhile, attempts to model microstructural characteristics and establish relationships between the macroscopic and microscopic behavior require careful experimental data.

The expected outcome of the present research is an in-depth understanding of fatigue fracture mechanisms and long-term stability with environmental effects on advanced engineering materials, HEAs, which are essential to develop lifetime-prediction capabilities and safety models, with an ultimate goal of optimizing the compositions and properties of HEAs for applications-related stress and corrosion environments.

Chapter 2. Background

2.1. High-Entropy Alloys

Nuclear, turbine, and aerospace industries currently place great demands on advanced structural alloys with corrosion-resistant properties [1], and look for materials that could be superior to conventional nickel-based superalloys. In the last decade, a new class of materials, called HEAs, has been proposed and developed [2-17]. These alloys contain 5 or more elements at near equiatomic concentrations and may favor the formation of disordered solid-solution phases with the high mixing entropy, $\Delta S_{\text{mix}} = -R\sum_{1}^{N} x_i \ln x_i$, in place of ordered intermetallic phases that have much smaller entropy of mixing [2, 3, 5, 18, 19]. Here x_{i} is the atomic fraction of element, *i*, and R is the gas constant. The Gibbs free energy, ΔG, of a given phase can be expressed as:

$$\Delta G = \Delta H - T\Delta S \tag{1}$$

Here ΔH and ΔS are, respectively, the enthalpy and entropy of phase formation, and T is the absolute temperature. In disordered solid solutions where the chemical interactions between the different pairs of atom constituents are not much different from the average (i.e., ideal or regular solid solutions), $\Delta S = \Delta S_{\text{mix}} = -R\sum_{1}^{N} x_i \ln x_i$, and in ordered intermetallic phases, $\Delta S \approx 0$.

From Equation (1), increasing ΔS_{mix} will reduce the Gibbs free energy and may stabilize the solid-solution phase. This trend will be more pronounced at elevated temperatures. Controlled by solid-solution-strengthening, the yield strength of HEAs can be very high, and may be comparable to bulk metallic glasses (BMGs) [4, 20]. Although BMGs have high strength only at

relatively low temperatures (below the glass-transition/crystallization temperatures), crystalline HEAs may retain their high strength at higher temperatures [12, 21].

Figure 1 presents an Ashby map showing the range of yield strength (σ_y) versus Young's modulus (E) for materials, such as foams, natural materials, elastomers, ceramics, polymers, composites, and metallic alloys, along with the properties of BMGs and HEAs [4, 5, 19, 21-26]. Contour lines at constant resilience values, σ_y^2/E, are also shown. Materials with higher resilience can store larger elastic energies, and thus make good springs [22]. Figure 1 shows that the σ_y vs E data for HEAs lie outside the benchmarks established by conventional alloys and are comparable to BMGs.

2.2. Microstructures and Fracture Mechanisms

Alloy microstructures must be stable for elevated-temperature applications, because phase transformations occurring during use could deteriorate properties and lead to failure. High ΔS_{mix} stabilizes disordered solid solutions at elevated temperatures. The entropy product, $T\Delta S_{mix}$, decreases linearly with temperature and ordered intermetallic phases with large, negative enthalpies of formation can become thermodynamically preferable. On the other hand, phase-transformation kinetics decrease with decreasing temperature, and the formation of the intermetallic phases may require long annealing times. At the same time, suppressed kinetics may lead to the precipitation of exceptionally fine, nanometer-sized particles and considerably improved properties of these alloys at ambient temperatures. Therefore, studying the phase and microstructure stability in HEAs is important for candidate high-temperature structural materials.

In the as-cast condition through the rapid quenching process, HEAs studied to date tend to have a single-phase body-centered-cubic (BCC), face-centered-cubic (FCC), and/or hexagonal-

close-packed (HCP) crystal structures [27-31]. After processing at elevated temperatures, e.g., by forging, annealing, and aging, additional phases, including intermetallic phases, can form and make HEAs more complex [32-34]. For example, after thermo-mechanical treatments, the intermetallic sigma phase was found in $Al_xCoCrFeNi$ and $Al_xCoCrCuFeNi$ HEA systems [35-37], and unidentified phases also appeared [38, 39]. Unfortunately, thermodynamics and kinetics of phase transformations in HEAs are still unclear, making phase evolution difficult to predict.

One of the earliest quinary HEAs, AlCoCrFeNi, was first reported in 2007 [4]. It belongs to the $Al_xCoCrFeNi$ system, which is one of the most well-developed and refined HEA systems [4, 32, 36, 40-48]. The AlCoCrFeNi alloy shows the high compressive yield strength (σ_Y = 990 MPa) with reasonable compressive ductility (ε = ~ 63 %) at 500 ℃, as shown in Figure 2 [49]. The high strength at elevated temperatures makes it a promising structural material. A single-phase BCC crystal structure has been reported for the as-cast AlCoCrFeNi HEA [32, 43]. Others, however, report the presence of the B2 (ordered BCC) [41, 47] and A1 or L12 structure in the as-cast condition [48]. There are no publications in the open literature on the homogenized phase stability and high-temperature tensile properties of this important HEA system. On the other hand, limited microstructural behavior and fracture mechanism of this alloy at elevated temperatures have been studied previously and shows tremendous potential for elevated-temperature applications by exhibiting high hardness and yield strength at both room and elevated temperatures, even greater than 500 ℃ [4, 32, 36, 40, 43, 46, 48-51].

For thermocalculation modeling, an effective approach is necessary to determine and/or predict multi-component phase diagrams for HEA systems. Traditionally, binary and ternary phase diagrams have relied upon experimental methods. The phenomenological CALculation of PHAse Diagrams (CALPHAD) approach [52] is an effective aid in materials design [53-56], and has

recently been successfully used in the AlCoCrFeNi HEA system [57]. A thermodynamic database for the Al-Co-Cr-Fe-Ni system was developed [57]. Different from traditional alloys, which usually focus at one key element corner, the HEAs have multiple key elements. This trend requires the database to be valid in the entire composition region.

2.3. Mechanical Behavior

Superior structural alloys remain in a high demand for some extreme environmental engineering, particularly in the nuclear, turbine, and aerospace industries. HEAs are reported with high hardness and high compressive strength both at room temperature and elevated temperatures owing to their particular microstructures [3, 19, 26, 39, 45, 49, 58, 59]. HEAs also have shown great integrated tensile properties, including both high ultimate tensile strength and reasonable ductility [35, 39, 60]. Overall, it has been reported that the FCC-structured HEAs exhibit low strength and high plasticity, and BCC-structured HEAs show high strength and low plasticity, and HCP-structured HEAs are seldom to be studied on mechanical properties. Thus, the structure types are the dominant factor for controlling the strength or hardness of HEAs. In this chapter, we will review some of the HEAs papers concern mechanical properties: what has been reported, why so, and hence, design and development to the next level.

2.3.1. Mechanical Behavior at Room Temperature

For room-temperature mechanical properties of HEAs, the yield strength can be varied from 300 MPa for the FCC-structured alloys to about 3,000 MPa for the BCC-structured alloys [4, 61]. The values of Vickers hardness range from 100 to 900. The structure types are one of the dominant factors for controlling the mechanical behavior of HEAs at room temperature. Here, we would like to discuss two other effects on mechanical behavior.

2.3.1.1. Alloying Effect

Like other conventional alloys, small amounts of alloying elements can also be added to HEAs to increase or reduce the strength, plasticity, hardness, etc. The addition of one alloying element to improve one property may have unintended effects on other properties. For example, in order to investigate the differences of effects of various alloying elements on mechanical properties of AlCoCrFeNi alloy, the effects of C, Mo, Nb, Si, Ti elements on AlCoCrFeNi alloy have been investigated systematically [4, 43, 44, 46].

Ma et al. [44] studied the Nb alloying effect, finding that the microstructures and properties of the AlCoCrFeNbxNi HEAs became two phases in the prepared AlCoCrFeNbxNi HEAs: one is body-centered-cubic (BCC) solid solution phase [Figure 3(a)); the other is the Laves phase of (CoCr)Nb type. The microstructures of the alloy series vary from hypoeutectic to hypereutectic, and the compressive yield strength and Vickers hardness have an approximately linear increase with increasing Nb content, as shown in Figure 3(b) [44]. Zhou et al. investigated the Ti alloying effect on AlCoCrFeNiTix, designed by using the strategy of equiatomic ratio and high entropy of mixing. The alloy system is composed mainly of body centered cubic solid solution and possesses excellent room-temperature compressive mechanical properties, as shown in Figure 4. Particularly for AlCoCrFeNiTi0.5 alloy, the yield stress, fracture strength, and plastic strain are as high as 2.26 GPa, 3.14 GPa, and 23.3%, respectively, which are superior to most of the high-strength alloys such as bulk metallic glasses [4, 62].

2.3.1.2. Cooling-Rate Effect

The high cooling rates are effective for reducing the inter-dendrite composition segregation and making the microstructure more uniform, and the ductility can be improved while the yield

strength has no significant change. Wang et al. [45] studied the cooling rates effects on the microstructure and mechanical behavior of a high entropy alloy of AlCoCrFeNi by preparing as-cast rod samples with different diameters. Smaller diameter rod samples have higher cooling rate when using the same equipments. He found that the cast diameter samples has the same phase of BCC solid solution while higher cooling rates lead to more uniform microstructures with reduced inter-dendrite composition segregation, as shown in Figure 5a-d [45]. With decreasing casting diameter, which means increasing cooling rate, both the strength and the plasticity are increased slightly, as shown in Figure 5e.

2.3.2. Mechanical Behavior at Elevated Temperatures

The high-temperature properties of the HEAs were also extensively studied. Like, conventional alloys, the microstructures and mechanical properties can be modified and tuned to reach the optimum. Figure 6 shows that the yield strength decreases with increasing the testing temperature. It is seen that the low Al-content alloy exhibits low yield strength, but it decreases slowly with increasing temperature. Figure 7 shows the change in mechanical properties of the $Al_{0.5}$CoCrCuFeNi HEA of the rolled sample as the temperature increased.

Figure 8 presents that the mechanical properties of the $Al_{0.5}$CoCrCuFeNi HEA of annealed samples as a function of the testing temperature. After annealing, the strength and hardness decrease, while the elongation increases and the strength decreases slowly with increasing the temperature, which means that heat-treatment will highly influence on the mechanical properties, especially at elevated temperatures. We'd like to discuss the heat-treatment effect on high temperature properties of HEAs, including one kind of high performance HEAs at elevated temperatures, called refractory HEAs.

2.3.2.1. Heat-Treatment Effects

Figure 9 shows the microstructure of the AlCrCuNiFeCo HEA in (a) as-cast and (b) hot-forged conditions [35]. Considerable refinement of the cast microstructure was observed after extensive multistep forging at 1,223 K. Figure 10 presents the typical stress-strain curves of the as-cast (a) and hot-forged (b) samples deformed at different temperatures with an initial strain rate of 10^{-3} s^{-1} [35]. We find that, after forging, the alloy is considerably softer and much more deformable than the as-cast alloy. Figure 11 exhibits the photographs of tensile samples after deformation at 1,273 K: (a) a nondeformed sample; (b) an as-cast sample (tensile ductility, d = 77%); and (c) a forged sample (d = 864 %) at a strain rate of 10^{-3} s^{-1}. The forged sample demonstrates highly homogeneous flow, great resistance to neck formation, and extraordinarily high elongation of 864 %. Figure 12 presents the corresponding SEM images of the fracture surfaces of samples after tensile-testing deformation at room temperature: (a and b) as-cast and (c and d) hot-forged conditions [35]. At low magnifications, the as-cast alloy sample has a coarse-faceted appearance (Figure 12a), whereas the forged sample has fine granular appearance (Figure 12c). This observation is consistent with the much smaller grain/particle size of the forged condition than the as-cast condition. High magnification images confirm brittle, quasi-cleavage, fracture of the as-cast alloy, with such characteristic features as flat facets, angular faceted steps, river-pattern markings, cleavage feathers, and tongues (Figure 12b). At the same time, high magnification images of the forged sample confirm a mixed type of brittle and ductile fracture (Figure 12d). The brittle type fracture is reflected by the presence of flat facets with characteristic river-pattern markings inside large dimples, while the ductile type fracture is reflected in numerous dimples of different diameters surrounding the flat facets. It is likely that, during tensile deformation of the forged sample, cracks are formed at the interfaces of the BCC and FCC particles

by brittle fracture, and then the crack opening into voids occurs by plastic deformation of nearest, more ductile regions [35].

2.3.2.2. Refractory HEAs

Currently, Ni-based superalloys already have the great combination of elevated temperature properties, including creep resistance, corrosion resistance, and damage tolerance, but operating temperatures are reaching the theoretical limits of these materials. The high entropy alloying (HEA) approach was used to develop new refractory alloys, which contain several principal alloying elements at near equiatomic concentrations, using new metallic materials with higher melting points, such as refractory molybdenum (Mo) and niobium (Nb) alloys [5, 19, 21, 26, 58].

Senkov et al. [21] reported the yield strengths of NbMoTaW and VNbMoTaW alloys at high temperatures, as shown in Figure 13. From Figure 13, we can see that the V addition is beneficial for increasing the strength, but not suitable for the heat-softening resistance. Figure 14 exhibits the specific yield-strength change with increasing the temperature for the TaNbHfZrTi, TaNbMoW, TaNbVMoW, and $CrCoCuFeNiAl_{0.5}$ cast alloys [26]. It can be seen that the high specific yield strength of the $CrCoCuFeNiAl_{0.5}$ HEAs can be sustained over to 1,100 K, and the TaNbMoW HEA can sustain it high specific strength to 1,800 K. Figure 15 shows the backscatter images of the NbMoTaW and VNbMoTaW HEAs after the deformation of 1,673 K.

Lower density and better room temperature ductility are required if we seek for applications in the aerospace engineering. By replacing V, Ta, and W in the NbMoTaW and VNbMoTaW alloys with lighter Cr, Mo, and Zr, respectively, the density of the new refractory $NbCrMo_{0.5}Ta_{0.5}TiZr$ HEAs alloy was reduced to 8.2 g/cm^3. In addition, the new alloy showed

improved room temperature ductility, relative to the NbMoTaW and VNbMoTaW alloys. Figure 16 exhibits the engineering stress-strain compression curves of the $NbCrMo_{0.5}Ta_{0.5}TiZr$ alloy samples after HIP at 296 K, 1,073 K, 1,273 K, and 1,473 K [58]. During deformation at 296 K, the yield strength was 1,595 MPa and continuous strengthening occurred until the alloy fractured by localized shear at peak strength of 2,046 MPa accumulating about a 5% strain. During testing at T = 1,073 K, yield strength decreased to 983 MPa, the peak strength of 1,100 MPa was achieved at a strain of 4.2%, and the sample fractured by shear at a strain of about 6%, after a decrease in strength to 1,050 MPa. An increase in the testing temperature to 1,273 K resulted in a considerable softening of the alloy after a short stage of strain hardening. At this temperature, yield strength ($\sigma_{0.2}$) = 546 MPa, compressive strength (σ_p) = 630 MPa, and the minimum strength achieved during strain softening was 393 MPa after a plastic strain of about 22%. At this temperature, the sample did not fracture. An increase in the temperature to 1,473 K, led to a further decrease in the flow stress of the alloy, and $\sigma_{0.2}$ was 170 MPa. The peak stress of 190 MPa was reached shortly after yielding, followed by weak softening and a steady state flow at the minimum strength (σ_{min}) = 135 MPa. No sample fracture occurred at this temperature.

Figure 17 presents the SEM secondary-electron images of the fracture surface of a $NbCrMo_{0.5}Ta_{0.5}TiZr$ alloy samples after compression deformation at room temperature [58]. It shows a combination of plastic and brittle deformation mechanism. The formation of dimples is convincing evidence of ductile deformation, while the pieces of teared microstructure are the sign of quasi-cleavage fracture of the FCC (Laves) phase, as well as along the interfaces.

In all, refractory HEAs is a entirely novel concept and relatively new area. Compared to compositions with 3d elements, refractory HEAs (4d elements) show exceptionally-promising

mechanical properties, especially at elevated temperatures. More research, including new compositions and fracture mechanism, need to be explored.

2.3.3. Mechanical Behavior at Cryogenic Temperatures

It is well acknowledged that the low-temperature mechanical properties are particularly beneficial for actual applications of metallic alloys. The mechanical behavior of HEAs at cryogenic temperatures are yet to be investigated in detail. It is also known that FCC metals do not exhibit a ductile-brittle transition temperature (DBTT), so should we expect the same for FCC HEAs? Meanwhile, because DBTT is known for BCC metals, has anybody done work on deformation of BCC HEAs at low temperature? The aim of this chapter is to review the compressive characteristics of both BCC and FCC HEAs at cryogenic temperatures.

Qiao et al. studied the compressive characteristics of a single-phase BCC HEA with the composition of AlCoCrFeNi at 77 K [63]. For the AlCoCrFeNi HEA, there is no obvious ductile to brittle transition even the temperature is lowered to 77 K. Comparing with the compression properties at different temperatures, it is concluded that the yielding strengths and fracture strengths of the AlCoCrFeNi HEA increase by 29.7 % and 19.9 %, respectively, when the temperatures decrease from 298 to 77 K, as shown in Figure 18. However, the fracture strains change gently, while the fracture modes at 298 and 77 K are intergranular and transgranular, respectively, as shown in Figure 19 [63]. That is to say, the DBTT of AlCoCrFeNi BCC HEA is lower than 77 K.

High-entropy alloy $Al_{0.5}CoCrCuFeNi$ has been deformed by compression and the peculiarities of the plastic deformation have been studied by Laktionova et al. [64] in a temperature range from 300 K to 4.2 K. The alloy has been found to provide a high strength and plasticity

greater than 30 % in this temperature range: the yield stress amounts to 450 MPa for 300 K and 750 MPa for 4.2 K, as shown in Figure 20. At temperatures below 15 K, the smooth behavior of the stress-strain curves changes to the serrated one. Thus, FCC HEAs do not exhibit DBTT, like FCC metals.

2.4. Fatigue Failure and Life Prediction

If we seek for the application in the aerospace industry or other field, besides monotonic loading, the fatigue behavior and lifetime prediction are other most influential factors, which are required to be studied and explored, yet rarely reported. The first and only publication so far concerning the fatigue behavior of HEAs, with a composition of $Al_{0.5}CoCrCuFeNi$, came from our group, Hemphill et al. [7]. They found that the fatigue study showed promising fatigue-resistance characteristics due to the prolonged fatigue lives of various samples at relatively high stresses. Compared with conventional alloys, such as steels, Ti-based alloys, and advanced bulk metallic glasses (BMGs), their results suggest that the fatigue behavior of $Al_{0.5}CoCrCuFeNi$ compares favorably. However, one obvious issue is that some unpredictability in the fatigue life of the samples was observed as variations in the stress vs. lifetime plot. They believe that the reason of variations is because of microstructural defects, such as aluminum-oxide inclusions and microcracks, which were introduced during the sample-fabrication process and thermal heat treatment, including casting and rolling. Meanwhile, the fracture mechanisms of four-point-bending (4PB) fatigue is not clearly discussed. Thus, the precise knowledge of fracture mechanism is necessary to model the fatigue behavior of HEAs during cyclic loading.

Hemphill et al. [7] studied fatigue behavior of the $Al_{0.5}CoCrCuFeNi$ HEA and compared the results to many conventional alloys, such as steels, titanium alloys, and advanced BMGs.

Figure 21a shows that a typical stress range versus the number of cycles to failure (S-N) curves comparing fatigue ratios [fatigue ratio = fatigue endurance limit / ultimate tensile strength (UTS)) of the $Al_{0.5}$CoCrCuFeNi HEA to other conventional alloys, and BMGs [7]. The lower bound of the fatigue ratios of HEAs compares favorably to those of steels, titanium, and nickel alloys, and outperforms zirconium alloys as well as some of the Zr-based BMGs. Moreover, for some materials, such as ultra-high strength steels and wrought aluminum alloys, their high tensile strengths result in lower fatigue ratios due to their brittle nature. The strong group (which is defined as samples in the group contain fewer fabrication defects and can reveal the intrinsic fatigue behavior of the HEA) of HEAs tends to outperform these materials by displaying a greater fatigue ratio than materials with comparable tensile strengths due to the reduced number of defects. The upper bound of the fatigue limit of HEAs is significantly higher than that of other conventional alloys and BMGs, showing that HEAs have the potential to outperform these materials in structural applications with improved fabrication and processing. These results are highly encouraging for excellent fatigue resistance in HEAs and with possible long fatigue life, even at stresses approaching the ultimate stress. Because of the lack of the literature on the fatigue behavior of HEAs, the focus of the continuing research should be placed on the data points that show an unexpectedly long fatigue life. If the necessary information on the fatigue resistance can be found and a prediction model for fatigue specimens can be developed, HEAs have a promising future in numerous applications for components in fatigue environments.

Figure 21a illustrates the fatigue-endurance limits for the $Al_{0.5}$CoCrCuFeNi HEA as a function of UTS. One reason for the high fatigue strength of HEAs is the high tensile strength of these materials. It can be clearly seen that as the UTS increases the fatigue endurance limit also increases in a linear fashion, approximately equal to 0.5 for most materials [7]. HEAs follow a

similar pattern and even exceed this ratio, with an upper bound of 0.703. To better compare the fatigue performance of HEAs with other materials with respect to their UTS, the fatigue ratios are used, as shown in Figure 21b.

Meanwhile, the fatigue-endurance limit is usually treated as a constant for a material, and it is a common practice to report the endurance limit of a material to be the stress level below which failure will not occur before an arbitrary large number of cycles, usually 10^7 cycles. In addition, the data from stress verses cycles to failures (S-N) curves are usually analyzed by a simple linear regression approach, which cannot adequately account for the excessive scatter in the data. Nelson [65] first suggested modeling the endurance limit of a material as a random variable instead of a fixed constant; that is, test specimens have different endurance limits according to some "strength distribution." Pascual and Meeker [66] later developed a random endurance-limit fatigue-life model to describe (1) the dependence of fatigue life on the stress level and (2) the scatter in the S-N data. They applied their model to analyze the four-point-bending fatigue data of the carbon eight-harness-satin/epoxy laminate, and their results provided evidences suggesting the random nature of the fatigue-endurance limit. They argued that the randomness in the endurance limit is due in part to the location, orientation, size, and number of defects (e.g., cracks) in the material, which are random themselves. Wallin [67] also examined the statistical aspects of the fatigue-endurance limit, and observed that the variation in the endurance limit has a pronounced effect on the scatter in fatigue life close to the endurance limit. Lognormal, normal, and Weibull distributions have been proposed in the literature to describe the randomness in the endurance limit [67]. Thus, it is significant to perform life-prediction modeling of these alloys, investigating the connection between defects and the fatigue-endurance limits of HEAs by means of statistical fatigue-life modeling.

2.5. Corrosion Behavior and Environmentally-Assisted Failures

Corrosion of metallic materials is an electrochemical interaction between the metals or alloys and their environments, which is generally detrimental to the proper functions of materials and must be prevented. The cost of corrosion in the United States (U.S.) is estimated to be increased from $276 billion in 1998 to $1 trillion in 2013, which is 6.2 % of the U.S. gross domestic product (GDP) [68, 69]. Therefore, the study on the corrosion behavior and mechanism of metals and alloys and the development of corrosion-resistant materials are of enormous economic benefits. Materials to be used in long-term applications as structural or functional materials are expected to possess satisfying corrosion resistance. Noble metals (e.g., Ag, Au, Pt, etc) are stable and exhibit excellent corrosion resistance even in aggressive environments [70]. However, the scalability of noble metal applications is restricted by their high cost and poor mechanical properties [70]. Another category of corrosion-resistant materials, include stainless steels, titanium alloys, cobalt-chromium alloys, and so forth, which are widely used in industry. The underlying corrosion-resistant mechanism for these metals or alloys involves the formation of passive film on the surface, which protects the underneath alloys to be further corroded [70]. In addition to the alloy composition, corrosion behavior of metallic materials is also determined by microstructures [70]. For example, carbides at grain boundaries of stainless steels deteriorates their corrosion resistance due to the formation of susceptible Cr-depleted zones, which can be diminished by heat treatments [71]. Therefore, metallurgical factors, including alloying and processing (e.g., heat treatments) parameters, are very important to the development and investigation of corrosion-resistant metals or alloys.

Due to formation of disordered solid-solution phases, specifically BCC and/or FCC phases, HEAs are expected to exhibit superior corrosion resistance relative to conventional alloys. Most

HEAs contain passivating elements, such as Al, Cr, Mo, etc, which facilitate the formation of passive layers, similar to the case in stainless steels. Meanwhile, HEAs tend to be free from impurities or inclusions, which usually act as corrosion-initiation sites [71]. In particular, HEAs, forming single-phase solid solutions with homogenous chemical compositions and exhibiting a combination of excellent microstructural stability and decent mechanical properties [5, 9, 21], are also expected to yield good corrosion resistance. Such unique properties of HEAs make them good candidates for practical corrosion-resistant applications. A number of investigations were reported, which demonstrated the corrosion behavior of HEAs. Equivalent or superior corrosion resistance of HEAs was found, relative to conventional corrosion-resistant alloys, such as 304 stainless steels (SS), in various aqueous environments [33, 51, 72-85].

2.5.1. Corrosion Behavior of Al-Alloying HEAs

Passivating elements (e.g., Al, Cr, and Ti) tend to encourage the formation and enhance the performance of passive films. A well-known example of passive film enhancement by alloying is the addition of Cr to steels [70]. A variety of mechanisms were proposed to explain the effect of alloying on the properties of passive films, including: (1) an increase in the thermodynamic stability of the passive film, (2) an enhanced tendency to form a continuous barrier between materials and environments, (3) a decrease in the dissolution kinetics, (4) lower critical currents for passivation, (5) higher rates of repassivation, (6) the suppression of electron transfer, and (7) the superior wear resistance to diminish possibilities for erosion corrosion [51, 86-89].

It was previously found that in HEA systems Al alloying can significantly affect phase-structure evolution [14, 51, 78, 90, 91]. With increasing Al contents, lattice types vary from FCC to FCC+BCC, and eventually to BCC+B2 (namely a NiAl-type ordered phase structure) structure in several HEA systems, such as $Al_xCoCrCuFeNi$ [3], $Al_xCoCrFeNi$ [40], and $Al_xCrCuFeNi_2$ [92].

These changes in crystal structures induced by Al alloying can significantly affect the corrosion behavior of the HEAs. Considering their effects on the resulting mechanical and corrosion behavior, Al alloying can be either beneficial or detrimental, which will be discussed in detail below.

Taking the $Al_xCoCrFeNi$ ($x \leq 1$) alloy system as an example, although Al addition enhances the strength of the alloy at the cost of the reduced ductility due to phase changes, from FCC to FCC+BCC, and eventually to BCC+B2 lattice structures (Figure 22), excessive Al addition deteriorates the corrosion resistance of this HEA system in sulfuric acids. Kao and colleagues have reported the corrosion behavior of $Al_xCoCrFeNi$ ($x \leq 1$) alloys with different microstructures in 0.5 M H_2SO_4 solution. As shown in Figure 22, after immersion tests, few indications of corrosion were observed on the surfaces of both Al-free ($x = 0$) and low Al content ($x = 0.25$) $Al_xCoCrFeNi$ alloys, which were composed of single FCC phase. With an increase in Al to $x = 0.5$, the BCC phase emerged, resulting in a mixture of BCC and FCC phases. Signs of corrosion can be observed on $Al_{0.5}CoCrFeNi$ surfaces, which were mainly found on the BCC phase, whereas the FCC phase retained a smooth morphology. The BCC+B2 microstructure of a high-Al content $Al_xCoCrFeNi$ ($x = 1$) alloy was correlated to the lowest corrosion resistance, whereby a rough morphology was observed after immersion tests [51]. The decrease in corrosion resistance of $Al_xCoCrFeNi$ ($x \leq 1$) with increasing the Al concentration was attributed to the formation of pores and the inferior quality of its passive films, which is more distinct at higher temperatures and higher chloride concentrations in chloride-containing solutions [51]. Electrochemical-impedance-spectroscopy (EIS) results have indicated that the passive films become thicker and more dispersive with increasing Al, causing the passivation current (i_{pass}) to increase in the $Al_xCoCrFeNi$ HEA system when exposed to sulfuric solution [51].

In cases of high Al ratio ($x \geq 0.5$), the passive film became unstable and can easily form metastable ion complexes, which eventually dissolve away [51]. Therefore, FCC structures with low Al ratios ($x \leq 0.25$) have better passive performance and corrosion resistance in the $Al_xCoCrFeNi$ HEA system. In fact, the concept that alloys with an FCC structure exhibit higher passivity has been previously employed in the design of 18-8 stainless steels (Fe-18Cr-8Ni in weight percent), the corrosion resistance of which was enhanced by the addition of the austenite (an FCC structure) stabilizer Ni [93].

Similarly, the increase in the corrosion resistance with the decrease in the Al fraction was also found in $Al_xCrFe_{1.5}MnNi_{0.5}$ HEAs tested in H_2SO_4 and NaCl solutions [78]. As shown in Figure 23, scanning-electron-microscopy (SEM) micrographs revealed that the general dissolution and pitting-corrosion susceptibility of the HEAs increased as the amount of Al increased [27].

On the surface of the $CrFe_{1.5}MnNi_{0.5}$ alloy, there was almost no pitting behavior, while the $Al_{0.5}CrFe_{1.5}MnNi_{0.5}$ alloy suffered from localized corrosion, which was more significant than that of the $Al_{0.3}CrFe_{1.5}MnNi_{0.5}$ alloy. This trend may be due to the fact that Al tends to form a porous oxide film on the surface of the substrate in the sulfuric acid, resulting in weaker and more porous oxide regions, which suffer from galvanic corrosion [78, 94]. On the other hand, different microstructures, changing from FCC+α-FeCr ($CrFe_{1.5}MnNi_{0.5}$), to FCC+BCC ($Al_{0.3}CrFe_{1.5}MnNi_{0.5}$), and eventually to BCC ($Al_{0.5}CrFe_{1.5}MnNi_{0.5}$) lattice structures may also influence the corrosion behavior. The increase in the Al content encourages the growth of the BCC phase, whereas the passive films on the surfaces of an FCC structure with low Al ratios (e.g., $x \leq 0.25$) in the $Al_xCrFe_{1.5}MnNi_{0.5}$ HEA system tend to be more stable and thus more corrosion-resistant in certain aqueous corrosion environments (e.g., 0.5 M H_2SO_4 solution in Table 2).

Overall, the passive films formed on the surfaces of an FCC-structured HEA with low Al concentrations ($x \leq 0.25$) tend to be more stable and corrosion-resistant.

2.5.2. Corrosion Behavior of Cu-Alloying HEAs

Theoretically, the microstructures of HEAs are characterized by solid-solution phases (BCC and/or FCC) due to their high entropy, inhibiting the formation of intermetallic compounds and increasing the solubility of other elements [3]. In HEAs with an equimolar fraction for each element, the configuration entropy increases logarithmically with the number of components, based on the following equation:

$$\Delta S_{mix} = R \times \ln(N) \quad (2)$$

where N is the total number of elements in the solution phase, and R is the ideal gas constant. High-entropy solid-solution phases form due to the contribution from the higher entropy, compared with conventional alloys, according to the definition of the Gibbs free energy of mixing (ΔG_m) for a solid-solution phase:

$$\Delta G_m = \Delta H_m - T\Delta S_m \quad (3)$$

where ΔH_m is the enthalpy of mixing, ΔS_m is the entropy of mixing, and T is the absolute temperature. However, in practice only a few compositions form single high-entropy disordered solid solutions, while others either contain more than one phase, or have elemental partitioning among phases. The main reason may be that the configurational entropy with equimolar and near equimolar fractions of constituent elements may be not high enough to compete with the formation of compound phases. Also, the effect of other entropy sources, such as vibrational entropy, cannot be ignored [27].

For some HEAs with single solid-solution phases, galvanic corrosion is suppressed, since no nobler or less noble phases are present. However, as discussed above, the galvanic corrosion between phases was found in some HEAs with more than one phase. In galvanic corrosion, the corrosion of the least noble phase is accelerated by another nobler phase where the corresponding cathodic half reaction happens [86]. A common example of severe galvanic corrosion is graphitic corrosion in gray cast irons, consisting of graphite flakes (nobler phase) in a matrix of ferrites or pearlites (least noble phase) [86]. Similarly, a good example of galvanic corrosion in HEA systems is Cu segregation. Cu tends to segregate as clusters, forming Cu-poor dendrites and Cu-rich interdendrites during solidification due to their weaker bonding energies (chemical mixing enthalpy, ΔH^{chem}) with Fe, Co, Ni, and Cr [7, 14, 39, 95]. For example, a well-studied HEA, $Al_{0.5}CoCrCuFeNi$, consists of Cu-rich interdendrites in a Cu-depleted matrix [7, 39, 95, 96]. When $Al_{0.5}CoCrCuFeNi$ corrodes in an aqueous environment, the matrix becomes relatively noble, while Cu-rich interdendrites corrode readily, with the electrically-connected network of Cu-rich interdendrites acting as the cathodic-charge distribution system. The more active Cu-rich interdendrites can be continually consumed by the anodic half-reaction, which is supported by the cathodic half-reaction occurring in the Cu-depleted matrix. Galvanic corrosion between constituent phases also occurs in other Cu-containing HEA systems. Hsu *et al.* [77] found that $CoCrCu_xFeNi$ alloys suffered from localized corrosion after immersion tests in aerated 3.5 weight percent (wt.%) NaCl solution at room temperature for 30 days. The localized corrosion was found along the Cu-rich interdendrites in both $CoCrCu_{0.5}FeNi$ and $CoCrCu_{1.0}FeNi$, but not in the Cu-free CoCrFeNi HEA. Generally, the corrosion of Cu-containing HEAs is mainly attributed to the galvanic corrosion caused by the Cu segregation. The corrosion resistance generally decreases with the increase of the Cu concentration.

2.5.3. Heat-Treatment Effects on Corrosion Behavior of HEAs

Heat treatments are commonly adopted in processing conventional alloys. Different heat-treatment processes act differently on the microstructures and properties of the materials. For example, heat treatment of conventional alloys aimed at producing peak hardness and enhanced mechanical performance could result in the growth of precipitates, which can be attacked by galvanic corrosion and pitting [86]. The localized corrosion will be more severe, if the precipitates electrically connect to each other forming a network. On the other hand, certain heat treatments can homogenize the chemical distribution of elements, which is beneficial for the corrosion resistance of the material. A good example is that Cr-carbide precipitates in stainless steels can be re-dissolved, leaving the Cr evenly dispersed in the parent alloy, via the heat treatment above 1,035 ℃, followed by rapid quenching [86].

Based on Equation (3), increasing ΔS_{mix} will reduce the Gibbs free energy of HEAs, which stabilizes the solid-solution phase and suppresses the growth of intermetallic precipitates. This effect should be more pronounced at elevated temperatures. As discussed above, a more uniform structure is related to a higher corrosion resistance. Thus, such high-entropy effects at greater temperatures homogenize the microstructures and tend to improve the corrosion resistance of HEAs. If the heat-treatment conditions were properly selected, homogenization at certain high temperatures would dissolve Cr-rich and/or Cu-rich phases. The corrosion resistance of these alloys should be enhanced. For example, in the $CoCrCu_{0.5}FeNi$ HEA, the Cu-rich phase was successfully dissolved into an FCC matrix aging at 1,100 ℃–1,350 ℃, which resulted in better corrosion properties, compared with those aged at 350 ℃–950 ℃ [33]. It is noteworthy that not all heat treatments are suitable to advance the corrosion resistance of HEAs, as the effect can sometimes be contrary to what was desired. Examples are that several heat-treated HEAs, such as $Al_{0.5}CoCrFeNi$ [82]

and $CoCrCu_{0.5}FeNi$ [33], were reported to be susceptible to corrosion in a 3.5wt.% NaCl solution. In these cases, the heat treatments did not homogenize the microstructure, but instead, promoted the formation and growth of Cr-rich and/or Cu-rich phases rather than forming single-phase microstructures.

2.5.4. Comparisons with Conventional Corrosion-Resistant Materials

Among conventional corrosion-resistant materials, there are two major groups: one group that withstand high-temperature and dry or gaseous corrosion (called heat-resistant alloys, HRAs), and the other that withstand low-temperature aqueous corrosion (called corrosion-resistant alloys, CRAs). Most of the materials are competent for only one application as either HRA or CRA; whereas only a few alloys can be used for both applications (e.g., Inconel 625) [97]. As a new advanced engineering material, the chemical composition and microstructure of some HEAs present many similarities with conventional HRAs and/or CRAs, including the high concentrations of Cr, Fe, and Ni elements, and a single FCC lattice structure. Meanwhile, as MPEAs, HEAs can be alloyed more heavily than stainless steels and Ni-based alloys, meaning that larger amounts of specific elements may possibly be dissolved intentionally to tailor the HEAs for particular environments. Certain HEAs (e.g., $Al_xCoCrFeNi$ when $x \leq 0.3$) have hold better chances to serve as HRAs and/or CRAs, owing to their high-temperature strengths, being homogeneous as a single FCC structure at all temperatures, and lower cost, which leads to a wide range of industrial applications [27, 32, 36, 40, 48, 57]. In fact, the corrosion performance of HEAs is comparable or even superior to that of conventional alloys in certain aqueous corrosion environments, as will be discussed below.

The corrosion resistance of metals or alloys can include several parameters, such as the corrosion potential (E_{corr}), pitting potential (E_{pit}), corrosion current density (i_{corr}), and corrosion

rate. The E_{corr} is the reactivity of the alloy, a higher value of which indicates a more stable material. The E_{pit} represents the resistance of the material to pitting corrosion. The i_{corr} is relevant to the corrosion rate, as will be discussed below. According to the American Society for Testing and Materials (ASTM), G31-12a [98], Standard Guide for Laboratory Immersion Corrosion Testing of Metals, the average corrosion rates can be determined by the weight-loss method, which can be calculated from the following equation:

$$Corrosion\ rate\ (mm/year) = \frac{8.76\ \times\ 10^4\ \times\ W}{A\ \times\ T\ \times D} \tag{4}$$

where W is the total weight loss in gram after exposure, A is the exposure area of the specimen in cm^2, T is the exposure time in hour, and D is the density of the alloy in g/cm^3. This method is applicable to uniform corrosion. If the surface examination shows that the major types of corrosion are localized corrosion and/or pitting, the corrosion rate is usually determined using electrochemical-polarization measurements. Based on ASTM G102-89 [99], Standard Practice for Calculation of Corrosion Rates and Related Information from Electrochemical Measurements, Faraday's Law can be used to calculate the corrosion rate in terms of the mass-loss rate:

$$Corrosion\ rate\ (mm/year) = 3.27\ \times\ 10^{-3} \times \frac{i_{corr}}{\rho}\ \times EW \tag{5}$$

where i_{corr} is the corrosion current density in $\mu A/cm^2$, ρ is the density in g/cm^3, and EW is the alloy equivalent weight, which is given by:

$$EW = (\sum \frac{n_i f_i}{W_i})^{-1} \tag{6}$$

where n_i is the valence of the ith element of the alloy, f_i is the mass fraction of the ith element in

the alloy, and W_i is the atomic weight of the ith element in the alloy. The density of HEAs is calculated, using the rule of mixtures of pure elements, as shown below:

$$\rho_{mix} = \frac{\sum c_i A_i}{\sum c_i A_i / \rho_i} \quad (7)$$

where c_i, A_i, and ρ_i are the atomic fraction, the atomic weight, and the density of the element, i, respectively. The ρ_i values of the alloying elements are taken from [100].

A detailed comparison on the corrosion behavior between conventional corrosion-resistant alloys and HEAs is demonstrated in Table 1. Corrosion parameters, including E_{corr}, E_{pit}, and i_{corr} of HEAs and stainless steels in 3.5 wt.% NaCl solution at room temperature are summarized in detail (Figure 24 and Table 1). Generally, the corrosion potential and pitting potential of HEAs are comparable with those of 304 stainless steels. However, the corrosion current density of some HEAs tends to be much lower, which suggests a lower corrosion rate, as indicated in Equation (5). A comparison of the corrosion rate (mm/year) calculated from electrochemical measurements and the weight loss method is also shown in Table 1 and plotted in Figure 24. Data obtained from other materials, such as stainless steels, low alloy steels, low carbon steels, nickel alloys, aluminum alloys, and titanium alloys, and bulk metallic glasses (BMGs) are included for comparison. Corrosion rates of HEAs in the 3.5 wt.% NaCl solution at room temperature are generally lower than those of low carbon steels and low alloy steels, and comparable with stainless steels and aluminum alloys. It is notable that the $CoCrCu_{0.5}FeNi$ HEA heat-treated at 1,250 ℃ for 24 h exhibits comparably low corrosion rate with nickel alloys and titanium alloys. The outstanding corrosion resistance of the heat-treated $CoCrCu_{0.5}FeNi$ HEA can be explained by the fact that the heat treatment at 1,250 ℃ for 24 h is sufficient to dissolve Cu-rich segregation adjacent to grain boundaries in $CoCrCu_{0.5}FeNi$ HEA, as discussed previously. Similarly, corrosion properties of

HEAs in the 0.5 M H_2SO_4 solution are listed in Table 2. Several HEAs, such as CoCrFeNi, have good corrosion properties, including relative high corrosion potentials, low corrosion current densities, large passive regions, and low corrosion rates, compared with conventional alloys (Figure 25). The enhanced corrosion properties of CoCrFeNi are attributed to its single FCC solid-solution microstructure, which is favorable for the formation of a stable passive film. Thus, it is believed that some certain compositions with a proper processing method should make HEAs as good corrosion-resistant alloy candidates.

HEAs with a single-phase microstructure without precipitates and elemental segregation, especially an FCC structure, tend to have better corrosion resistance than multi-phase HEAs. Some single-phase FCC-structure HEA, such as CoCrFeNi and $CrFe_{1.5}MnNi_{0.5}$, are comparably and even more corrosion-resistant than conventional alloys [51, 78, 80], as shown in Table 1 and Table 2. Therefore, it will be very important to further understand the stability of the HEAs system under corrosion environments, with an ultimate goal of optimizing the compositions and properties for applications-related corrosion environments. Meanwhile, corrosion fatigue is an important but complex mode of failure for high-performance structural metals operating in deleterious environments [101]. The corrosion-fatigue behavior of HEAs in aqueous electrolytes is also important to be characterized with an effective life-prediction model.

Chapter 3. Overall Experimental Procedures

The work involves a new kind of advanced engineering materials, called HEAs. Three tasks are as follow: (1) microstructures and fracture mechanism of HEAs, (2) fatigue failure and life prediction of HEAs, and (3) fatigue and environmentally-assisted behavior of HEAs. An overall framework for the research work is shown in Figure 26.

3.1. Microstructures and Fracture Mechanisms of the Homogenized AlCoCrFeNi Alloy

The objective of first task is to study the microstructural stability and fracture mechanism of the AlCoCrFeNi alloys and compare with thermodynamic calculations. In this task, the effect of the homogenization heat treatment on the as-cast microstructure is investigated, and the influence of this substantial change in microstructure on tensile properties is measured. A comparison between predicted phase equilibria and phases observed after the homogenization heat treatment is made.

The as-cast samples of AlCoCrFeNi was prepared by arc-melting the constituent elements in a water-cooled, copper hearth, using a Large Bell Jar (ABJ-900) arcmelter of Materials Research Furnaces, Inc. The elements were be all at least 99.9 weight percent (wt. %) pure, and the melting process was conducted in a vacuum of at least 0.01 torr under a Ti-gettered argon atmosphere. Melting and solidification were repeated several times to improve sample homogeneity. Finally, the re-molten ingot was cast into 6 mm diameter rods (Figure 27). The final composition of the alloy was confirmed through quantitative analysis, by Inductively-coupled plasma optical emission spectrometers (ICP-OES). The carbon percentage was quantitatively analyzed by a

combustion method. Hydrogen, oxygen, and nitrogen were quantitatively analyzed by an inert gas fusion (IGF) method.

Several samples were be heat treated after casting. These samples are referred to as AlCoCrFeNi-HP. The heat treatment consisted of hot isostatic pressing (HIPing) and homogenization. To close porosity in as-cast samples, they were HIPed at 1,100 ℃ / 207 MPa for 1 hour in an ultra-high-purity argon atmosphere. The HIPed samples were placed in a horizontal tube furnace, evacuated with a rough pump, and then the tube was filled with the high-purity argon at a continuous flow rate of ~ 200 ml/min. The samples were heated to 1,150 ℃ at 10 ℃/min, held at 1,150 ℃ for 50 hours, then cooled to T = 50 ℃ at 10 ℃/min. Alloy densities were measured with a helium pycnometer AccuPyc 1330 V1.03. Cylindrical specimens were prepared for tensile tests according to the American Society for Testing and Materials (ASTM) Standard [102]. Uniaxial tensile tests were conducted in air using an 810 Material Test System (MTS) machine equipped with a box furnace. The tensile tests were performed at 700 ℃ with a nominal strain rate of 1×10^{-4} s^{-1}.

The microstructures were investigated by Transmission Electron Microscopy (TEM), Scanning Electron Microscopy (SEM), including energy dispersive spectroscopy (EDS) and electron back-scatted diffraction (EBSD). Combined EDS and EBSD techniques were used to analyze the dendritic structure, since EBSD alone cannot differentiate A2 and B2 phases. An etchant, Kalling's No. 2 (1 g $CuCl_2$, 20 ml HCl, and 30 ml ethanol), was used for selective etching. The samples were swabbed by the cotton ball with the etchant for 10 seconds, followed by running water and ethanol, and then blow-dried.

The sample phases at room temperature were analyzed using high-energy synchrotron X-ray diffraction in the 6-ID-D beamline, Advanced Photon Source (APS), Argonne National Laboratory. X-ray diffraction samples were in the form of powders from a cross-sectional slice of the sample. To investigate the phase transitions due to temperature, in-situ neutron-diffraction measurements were performed at the VULCAN engineering materials diffractometer (Beamline 7) in Spallation Neutron Source (SNS), Oak Ridge National Laboratory (ORNL). Specifically, the lattice and intergranular-strain evolution were studied as a function of phase change and temperature to understand the microscopic-deformation mechanisms in depth. A new database was developed using the available experimental information for the 10 constituent binaries and 10 constituent ternaries, and differential thermal analysis (DTA) of several HEAs in the AlxCoCrFeNi system. All the calculations in the present work were performed by the *PANDAT* software.

In summary, a combination of microstructural characterization and mechanical tests were performed by in-situ synchrotron and neutron diffraction methods with careful microstructural observations using SEM/EDS, EBSD, and TEM. These results allow for the identification of the AlCoCrFeNi HEAs with desirable microstructures, phase stability, and optimized mechanical behavior at elevated temperatures. Above all, the phase identification at different temperatures were compared to thermodynamic predictions and utilized to optimize thermodynamic calculations.

3.2. Fatigue Failures and Life Prediction of Cold-Rolled $Al_{0.5}CoCrCuFeNi$ Alloy

The objective of second task is to explore high-cycle fatigue failure mechanism of a cold-rolled Al0.5CoCrCuFeNi alloy, which is essential to develop lifetime-prediction capabilities and

safety models for future applications. It is widely believed that, oxide inclusions were be exterminated through using highly-purified raw material. Meanwhile, the porosities can be generally exterminated by rolling. Thus, based on those points above, a new set of HEAs was be fabricated using high purified elements and followed by cold-rolling process, compared with an old set of HEAs fabricated by commercial purified elements. The main purpose of this task is to reduce the scattering and explore the fracture mechanism, which is essential to develop lifetime-prediction capabilities and safety models for future applications.

The material investigated in this part was be a cold-rolled $Al_{0.5}CoCrCuFeNi$ alloy. The samples of $Al_{0.5}CoCrCuFeNi$ (mole percent) were prepared by arc-melting the constituent elements with a current of 500 amps in a water-cooled, copper hearth. The elements were from two sources: one was fabricated using commercial-purity (CP) elements while the other was manufactured with high-purity (HP) elements. The melting was done in a vacuum of at least 0.01 torr. The melting and solidification processes was repeated at least five times to improve the homogeneity of the sample, and cast into rectangular copper mold. The rectangular cast ingots were annealed at 1,000 ℃ for six hours and water quenched, which aimed to eliminate the shrinkage pore before cold rolling. The rolling reduction was 84 % with a final thickness of 3 mm. These materials were subsequently machined into fatigue samples with dimensions of 25 mm x 3 mm x 3 mm. To remove surface imperfections during the fabrication process, the samples were polished on a rotating polisher, finished by 1,200 grit emery paper, prior to fatigue tests. Besides the CP samples and HP samples above, a third condition of fatigue data was also used to compare and perform life prediction modeling. Three conditions of fatigue samples prepared by different combinations of purity of raw materials, shape of ingot, processing, and machining, as shown in Figure 28. Four-point-bend (4PB) fatigue tests were conducted in air on the material at different

applied loads. Tests run until failure of the specimen, or 10^7 cycles was reached, using a computer-controlled material test system based on a servohydraulic testing machine. The results of each test was plotted on a typical stress versus the number of cycles to failure (S-N) curve. The stress, σ, on the tensile surface within the span was calculated using the following beam-theory relationship,

$$\sigma = \frac{3P(S_o - S_i)}{2BW^2} \quad (2)$$

where P is the applied load, S_o is the outer span length of 20 mm, S_i is the inner span length of 10 mm, B is the thickness, and W is the height, both 3 mm, respectively. Samples were subjected to 4PB fatigue tests with a load ratio (R) of 0.1 (R = minimum stress/maximum stress, while the maximum stress is 1,200 MPa in the present study) under a load-controlled mode, using a sinusoidal waveform at a frequency of 10 Hz.

To obtain diffraction patterns of the sample, microstructural characterization was be performed in the Advanced Photon Source (APS), located at the Argonne National Laboratory. The fractography of the tensile region fracture surfaces was analyzed using a Gemini Leo 1525 field emission scanning electron microscopy (FE-SEM) at 15 kV and 20 kV, and energy-dispersive x-ray spectroscopy (EDS). Metallographic examinations were also made on cross-sectional planes (where the cut plane is normal to the tensile direction). Quantitative measurements of cavitation volume fraction were made directly on the optical microscopic (OM) micrographs, using a point-count technique. The reported values were the average values from the cavity measurement at least on 10 random cross-sectional planes in each case, so as to cover the entire cross-section of the test specimen.

In summary, this study was adopt the random endurance-limit fatigue life model to analyze the S-N data of the four-point-bending-fatigued $Al_{0.5}CoCrCuFeNi$ HEAs obtained from three conditions of samples with different fabrication processes and/or different purity grades of raw materials, which will understand the connection between defects and the fatigue-endurance limit of HEAs.

3.3. Fatigue and Environmentally-Assisted Behavior of $Al_{0.3}CoCrFeNi$

The objective of third task is to understand the fatigue-environmentally-assisted behavior of HEAs. A single-phase HEA, $Al_{0.3}CoCrFeNi$, was chosen for the study of electrochemical-polarization and environmentally assisted behavior. Moreover, tension-tension fatigue behavior and failure mechanism of single FCC $Al_{0.3}CoCrFeNi$ alloy were investigated in air and in the substitute ocean water, which provide a fundamental understanding of the fatigue behavior and fatigue/environment interaction behavior and life prediction of the single-phase FCC $Al_{0.3}CoCrFeNi$ alloy.

The raw elemental materials at least 99.9 wt.% purity were used. Repeated vacuum induction-melting for at least 5 times was carried out to improve the chemical homogeneity of the alloy. The solidified plate was HIP sintering at 1,200 ℃ and 100 MPa for 4 hours. Argon (Ar) gas was used to supply the high pressure. After the HIP sintering, the chamber temperature decreased from 1,200 ℃ to 340 ℃ in 3 hours, and then decreased to 190 ℃ in one hour (Figure 29). The tensile samples had a gauge length of 30 mm and a cylindrical gauge cross-section of 3 mm in diameter. Uniaxial tensile experiments were conducted in air using an 810 Material Test System (MTS) machine equipped with a box furnace. The slow strain rate tensile tests were performed at room temperature with a strain rate of 2×10^{-6} /s both in air and in ocean water environment.

Moreover, high-cycle tension-tension fatigue behavior and failure mechanism of the single-phase FCC $Al_{0.3}$CoCrFeNi alloy were investigated in air and in the substitute ocean water environment at different applied loads. The sample geometry followed the Standard Practice for Conducting Force Controlled Constant Amplitude Axial Fatigue Tests of Metallic Materials (ASTM Standard E466) [103], as shown in Figure 30. Electric discharge machining (EDM) was used to machine the corrosion-fatigue samples. Moreover, 600 grid emery paper was used to remove the etched surface resulted by the rest residues from EDM wire cutting.

Tests run until failure of the specimen, or 10^7 cycles were reached, using a computer-controlled material test system based on a servohydraulic testing machine. The flat fatigue specimen geometry with continuous radius corrosion-fatigue test configuration is shown in Figure 31. Stainless-steel pins were used to hold the samples. The results of each test were plotted on a typical stress versus the number of cycles to failure (S-N) curve. Samples were subjected to tension-tension fatigue tests with a load ratio (R) of 0.1 (R = minimum stress/maximum stress) under a load-controlled mode, using a sinusoidal waveform at a frequency of 10 Hz.

Before the fatigue tests, the phase structure and chemical composition were investigated using a Gemini Leo 1525 field emission scanning electron microscopy (FE-SEM) at 15 kV, energy-dispersive x-ray spectroscopy (EDS), Electron Backscatter Diffraction (EBSD) imaging, and X-ray diffraction (XRD). After fatigue tests, the fracture morphologies on specimens of fracture surface and tensile lateral plane were examined via SEM with EDS.

In summary, stress-corrosion cracking susceptibility and tension-tension high-cycle fatigue behavior and failure mechanism of single-phase FCC $Al_{0.3}$CoCrFeNi alloy were investigated in air and ocean water environment. The outcomes of this research are an improved understanding of the

single-phase FCC $Al_{0.3}CoCrFeNi$ alloy system under stress and corrosion environment, with an ultimate goal of optimizing the composition and properties for applications related corrosion environments.

Chapter 4. Microstructures and Fracture Mechanisms of An AlCoCrFeNi Alloy in As-Cast and Homogenized Conditions

The microstructure and phase composition of an AlCoCrFeNi high-entropy alloy (HEA) were studied in as-cast (AlCoCrFeNi-AC, AC represents as-cast) and homogenized (AlCoCrFeNi-HP, HP signifies hot isostatic pressed and homogenized) conditions. A combination of electron backscatter diffraction (EBSD), X-ray energy dispersive spectroscopy (EDS), transmission electron microscopy (TEM), scanning transmission electron microscopy (STEM), and high-energy synchrotron X-ray analyses showed the dendritrical structure in the AlCoCrFeNi-AC consisting primarily of a nano-lamellar mixture of A2 [disorder body-centered-cubic (BCC)] and B2 (ordered BCC) phases, in addition to a very small amount of A1 [disorder face-centered-cubic (FCC)] phases. The homogenization heat treatment, consisting of hot isostatic pressed for 1 hour at 1,100 ℃, 207 MPa and annealing at 1,150 ℃ for 50 hours, resulted in an increase in the volume fraction of the A1 phase and formation of a Sigma (σ) phase. Tensile properties in as-cast and homogenized conditions are reported at 700 ℃. The ultimate tensile strength was virtually unaffected by heat treatment, and was 396 ±4 MPa at 700 ℃. However, homogenization produced a noticeable increase in ductility. The AlCoCrFeNi-AC alloy showed a tensile elongation of only 1.0 %, while after the heat-treatment, the elongation of AlCoCrFeNi-HP was 11.7 %. Thermodynamic modeling of non-equilibrium and equilibrium phase diagrams for the AlCoCrFeNi HEA gave good agreement with the experimental observations of the phase contents in the AlCoCrFeNi-AC and AlCoCrFeNi-HP. The reasons for the improvement of ductility after the heat treatment are discussed.

4.1. Introduction

Nuclear, turbine, and aerospace industries currently place high demands on high-temperature structural-alloy properties [1], and look for materials that could be superior to conventional nickel-based superalloys. In the last decade, a new class of materials, called high-entropy alloys (HEAs) or multi-principal-element alloys (MPEAs), has been proposed and developed [2-14, 17, 27, 28, 104, 105]. These alloys contain 5 or more elements at near equiatomic concentrations and may favor the formation of disordered solid-solution phases with high mixing entropy, $S_{mix} = -R\sum_{1}^{N} x_i \ln x_i$, in place of ordered intermetall ic phases that have a much smaller entropy of mixing [2, 3, 5, 17-19]. Here x_i is the atomic fraction of element, i, and R is the gas constant. The Gibbs free energy of mixing, ΔG_{mix}, of a given phase can be expressed as:

$$\Delta G_{mix} = \Delta H_{mix} - T\Delta S_{mix} \quad (1)$$

Here ΔH_{mix} and ΔS_{mix} are, respectively, the enthalpy and entropy of mixing, and T is the absolute temperature. In disordered solid solutions (i.e., ideal or regular solid solutions), $\Delta S_{mix} = -R\sum_{1}^{N} x_i \ln x_i$, and in ordered intermetallic phases, $\Delta S_{mix} \approx 0$. From Equation (1), increasing ΔS_{mix} will reduce the Gibbs free energy and may stabilize the solid-solution phase. This trend will be more pronounced at elevated temperatures. Controlled by solid-solution-strengthening, the yield strength of HEAs can be very high, and may be comparable to bulk metallic glasses (BMGs) [4]. While BMGs have high strength only at relatively low temperatures (below the glass-transition/crystallization temperatures), crystalline HEAs may retain their high strength at higher temperatures [12, 21, 27].

Alloy microstructures must be stable for elevated-temperature applications, because phase transformations occurring during use could deteriorate properties and lead to failure. High ΔS_{mix} stabilizes disordered solid solutions at elevated temperatures. The entropy product, $T\Delta S_{mix}$, decreases with temperature and ordered intermetallic phases with large, negative enthalpies of formation can become thermodynamically preferable. On the other hand, phase transformation kinetics decrease with decreasing temperature, and the formation of the intermetallic phases may require long annealing times. At the same time, suppressed kinetics may lead to the precipitation of exceptionally fine, nanometer-sized particles and considerably improved properties of these alloys at ambient temperatures. Therefore, studying the phase and microstructure stability in HEAs is important for candidate high-temperature structural materials.

In the as-cast condition through the rapid quenching process, HEAs studied to date tend to have a single-phase body-centered-cubic (BCC), face-centered-cubic (FCC), and/or hexagonal-close-packed (HCP) crystal structures [27-31]. Many of them may have precipitations of B2 in BCC and/or $L1_2$ in FCC phases [48, 106]. After processing at elevated temperatures, e.g., by forging, annealing, and aging, additional phases, including intermetallic phases, can form and make HEAs more complex [32-34]. For example, after thermo-mechanical treatments, the intermetallic σ phase was found in $Al_xCoCrFeNi$ and $Al_xCoCrCuFeNi$ HEA systems [35-37], and unidentified phases also appeared [38, 39]. Unfortunately, thermodynamics and kinetics of phase transformations in HEAs are still unclear, making phase evolution difficult to predict.

The present work focuses on one of the earliest quinary HEAs, AlCoCrFeNi, first reported in 2007 [4]. It belongs to the $Al_xCoCrFeNi$ system, which is one of the most well-developed and refined HEA systems [4, 27, 32, 36, 40-48, 104, 107]. The AlCoCrFeNi alloy shows a high compressive yield strength (σ_Y = 990 MPa) with a reasonable compressive ductility (ε = ~ 63 %)

at 500 ℃ [49]. This high strength at elevated temperatures makes it a promising structural material. A single-phase BCC crystal structure has been reported for the as-cast AlCoCrFeNi [32, 43]. Others, however, report the presence of B2 [41, 47] and A1 or $L1_2$ structures in the as-cast condition [48]. There are no publications in the open literature on the homogenized phase stability and high-temperature tensile properties of this important HEA system. In this paper, the effect of the homogenization heat treatment on the as-cast microstructure is studied, and the influence of this substantial change in microstructures on tensile properties is investigated. Comparison between the predicted phase equilibria and phases observed after homogenization heat treatment is made.

4.2. Thermodynamic Modeling

The as-cast HEAs may have different phases than the homogenized HEAs, since rapid cooling can suppress equilibrium phases, which often require a significant elemental redistribution. An effective approach is necessary to determine and/or predict multi-component phase diagrams for HEA systems. Traditionally, binary and ternary phase diagrams have relied upon experimental methods. The first-principles alloy theory was applied to predict the structures of the Al_xCoCrFeNi HEA system, and it was concluded that alloys around the equimolar AlCoCrFeNi composition have superior mechanical performance, as compared to the single-phase regions [104]. Meanwhile, Widom et al. applied a hybrid Monte Carlo and molecular-dynamics (MD) method to study the temperature-dependent chemical order for the refractory MoNbTaW HEA [108]. They found that the Monte Carlo species swaps allow for the equilibration of the structure, which cannot be achieved by conventional MD simulations [108]. In addition, the phenomenological CALculation of PHAse Diagrams (CALPHAD) approach [52] is proved to be an effective aid in materials design [53-56], and has recently been successfully used in the AlCoCrFeNi HEA system [57].

The essence of the CALPHAD approach is to obtain self-consistent thermodynamic descriptions (Gibbs energy functions) of lower-order (binary and ternary) systems by fitting to known thermodynamic and phase-equilibrium data. A thermodynamic description represents a set of Gibbs-energy functions with optimized thermodynamic-model parameters for all the phases in a system. The thermodynamic description for higher-order systems can be obtained via an extrapolation method [109]. This description enables estimates of phase diagrams and thermodynamic properties of multi-component systems that are experimentally unavailable.

A thermodynamic database for the Al-Co-Cr-Fe-Ni system was developed [57]. Different from traditional alloys, which usually focus at one key element corner, the HEAs have multiple key elements. This trend requires the database to be valid in the entire composition region. The current database was developed, using the available experimental information for the 10 constituent binaries and 10 constituent ternaries. In this database, the disordered solution phases, such as A1 and A2, are described by the substitutional solution model; the ordered intermetallic phases, such as sigma and B2, are described by the compound-energy formalism, and the line compounds are described by the stoichiometric model. Details of these thermodynamic models can be found in References [110, 111], and will not be repeated here. It should also be pointed out that the Gibbs energy of all the phases in the 5-component system were obtained from those of binaries and ternaries [57], and no thermodynamic model parameters were optimized using the experimental data of the present work for the 5-component system. All the calculations in this work were performed by the *PANDAT* software.

4.3. Results

4.3.1. Microstructures of the Alloy in the As-cast Condition

The microstructure of the AlCoCrFeNi-AC alloy is shown in Figure 32. The microstructure consists of equiaxed grains (Figure 32a). Flowery, branched dendrites are seen inside the grains at higher magnification (Figure 32b). The dendrites span is ~ 40 μm, and the arm thickness is ~ 20 μm. Figure 33 presents the image quality, inverse pole-figure and phase-identification maps of grains and dendrites, as well as the elemental maps. The data were collected simultaneously with the EBSD and EDS techniques. Randomly-oriented equiaxed matrix grains are clearly recognized on the image quality and inverse pole figure maps (Figure 33a-b). The phase map (Figure 33c) and EDS element mapping (Figure 33d-h) reveal two distinct compositions. The dendrites with the volume fraction of 45 % are enriched with Al and Ni (called NiAl-rich dendrites), and the interdendritic regions with the volume fraction of 55 % are enriched with Cr and Fe (called NiAl-poor interdendrites), while Co is uniformly distributed inside these phases. The chemical compositions of both NiAl-rich dendrites and NiAl-poor interdendrites are shown in Table 4.

To further investigate phase structures of NiAl-rich dendrites and NiAl-poor interdendrites, bright-field and dark-field TEM images of the interior of the matrix grains are exhibited in Figure 34. Note that the origin of the TEM sample came from either NiAl-rich or NiAl-poor region due to the sample preparation limitation. The dark-field TEM images were produced using a fundamental spot of the A2 and B2 phases [Figure 34(b)] and a superlattice spot of the B2 phase [Figure 34(c)]. They reveal a lamellar structure of the matrix grains consisting of fine, nanometer-sized lamellae of A2 and B2 phases. Figure 34(d) is a false-color scanning transmission electron microscopy (STEM) EDS map showing the distribution of Al (red), Co (green), and Cr (blue) in

the phases. It can be clearly identified that the A2 phase is enriched with Cr, and the B2 phase is enriched with Al. A bright-field and high-angle-annular-dark-field (BF-HAADF) pair of aberration-corrected STEM (AC-STEM) images also confirms its A2+B2 structures (Figure 35). The semiquantitative analyses by STEM-EDS spectra of A2 and B2 phases are shown in Table 5. In addition, a very small amount (volume fraction is less than 1-2 %) of fine precipitates of an additional phase, which has an A1 (disordered FCC) structure and is enriched with Co, is also identified inside grains (Figure 34d). This phase is anticipated from the solidification simulation conducted in the following section by the Scheil model [112], while the chemical compositions by the STEM-EDS spectra quantification of this A1 phase are not reliable due to its thickness less than a full foil. The reason is when we place a beam on the particle, we are measuring X-rays (chemistry) from both the particle and the matrix. In reality, we don't know how thick the particle is, relative to the matrix. Thus, we don't know how much contribution is coming from each. Therefore, STEM-EDS spectra quantification of the A1 phase is not reliable and not presented in Table 5. The nano-lamellar A2+B2 structure seems to co-exist in both NiAl-rich dendrites and NiAl-poor interdendrites, while the A1 phase might only exist in the interdendritic region, and the reasons are discussed in the following sections.

To sum up, based on the electron-microscopy study, the AlCoCrFeNi-AC primarily consists of a nano-lamellar mixture of the A2 and B2 phases, as well as a very small amount of A1 nanoprecipitates. The NiAl-rich dendrite regions are enriched with the B2 phase, in addition to the A2 phase. The NiAl-poor interdendrite regions are enriched with the A2 phase, beside a large amount of B2 phases and a small amount of A1 nanoprecipitates. The volume fraction of each phase presented in the as-cast condition is shown in Table 6.

4.3.2. Microstructures of the Alloy after the Homogenization Treatment

The homogenization treatment led to dramatic changes in the alloy microstructure (Figure 36). The homogenized alloy is called AlCoCrFeNi-HP. Instead of dark dendrites (NiAl-rich) in a bright matrix (NiAl-poor) (Figure 32), light-color precipitates are now recognized inside of the grey-color matrix and along grain boundaries. The different grey levels of the constituents in the backscattered-electron (BSE) images result from different compositions, e.g., brighter contrasts correspond to higher concentrations of heavier elements. The combined EBSD/EDS analysis reveals the presence of four phases in the homogenized alloy (Figure 37). The matrix grains have a B2 crystal structure. Two other phases, one with an A2 crystal structure and another with a tetragonal crystal structure (σ phase), precipitate inside the large B2 grains. The fourth phase, with the A1 crystal structure, mainly precipitates along grain boundaries, although some particles are also present inside the grains. The elemental analysis of these phases reveals that the B2 phase is rich in Ni and Al, the A2 and σ phases are rich in Cr and Fe, and the A1 phase is slightly enriched with Al, Co, and Cr. The chemical compositions of four phases (A2, B2, A1, and σ) determined by SEM-EDS are shown in Table 5, and the volume fractions of these four phases determined through the EBSD analysis, and calculations are shown in Table 6. Bright-field TEM images of the AlCoCrFeNi-HP alloy are shown in Figure 38. Nanoprecipitates with an A2 structure (indicated by red arrows) inside the B2 matrix are easily recognized. As shown in Figure 38(c-g), STEM-EDS X-ray maps of the microstructures of the AlCoCrFeNi-HP alloy (in a homogenized condition) confirm that the A2 nanoprecipitates is enriched with Co, Cr, and Fe, while the B2 matrix are enriched with Ni and Al. The chemical compositions of these phases are consistent with those in the homogenized condition (Table 5), showing that A2 has 19 at. % Co, 43 at. % Cr, and

30 at. % Fe. In all, based on the electron microscopic investigation, the AlCoCrFeNi-HP is confirmed to be composed of four major phases: A2, B2, A1, and σ.

4.3.3. Characterizations Using Synchrotron X-ray Diffraction

High-energy synchrotron X-ray diffraction shows that the as-cast alloy contains two phases: the A2 phase with a lattice parameter of a = 2.875(1) Å, and the B2 phase having a very similar lattice constant and crystal structure with respect to the A2 (Figure 39). The presence of the B2 phase was confirmed by a (100) superlattice peak. The A2+B2 structures were consistent with previous publications [4, 41]. This trend is also very common in other HEA systems, where Tsai et al. found that the lattice constants among the three phases in $Al_{0.3}CoCrCu_{0.5}FeNi$, measured using the TEM images, were very similar [113]. The Co-rich A1 phase found on TEM pictures (Figure 34d) was not identified by synchrotron diffraction, which may be due to its very small amount (volume fraction is less than 1-2 %) presented in the as-cast condition.

Four phases were identified in the AlCoCrFeNi-HP: A2 and B2 having the same lattice parameter a = 2.869(1) Å, A1 with a = 3.596(9) Å, and σ with a = 8.800 Å and c = 4.544 Å. The heat treatment slightly alters the lattice parameter of the A2 and B2 phases from 2.875(1) Å to 2.869(1) Å. This trend may be caused by the diffusion of solute atoms and then creation of vacancies among A2+B2 phases in order to form another two new phases (A1 and σ). Such diffusion will also lead to chemical-composition changes, possibly contributing to the slight change of lattice parameters. The σ phase is an ordered intermetallic compound with $P4_2/mnm$ (#136) [114]. The three strongest peaks belonging to this phase, (410), (411), and (331), as well as (002), are found in the synchrotron pattern. Three other σ peaks, (330), (202), and (212), are shielded by peaks from other phases. In sum, phase identification for both the as-cast (A2+B2) and

homogenized (A2+B2+A1+σ) conditions using synchrotron X-ray diffraction well agrees with the electron microscopic results.

4.3.4. Mechanical Behavior

Figure 40 shows the engineering stress-strain curves of the AlCoCrFeNi alloy in both the as-cast (AlCoCrFeNi-AC) and homogenized (AlCoCrFeNi-HP) conditions for tensile testing at 700 ℃. The values of the elongation to fracture (ε), yield strength (σ_y), ultimate tensile strength (σ_{UTS}), and specific strength (σ_{UTS}/ρ) of the samples are given in Table 7. The value of σ_y for the as-cast and heat-treated alloy are 395 MPa and 295 MPa, respectively. A noticeable increase in tensile elongation occurs after the heat treatment: the elongation increases from 1.0 % for as-cast samples to 11.7 % for heat-treated samples. The values of σ_{UTS} for as-cast (400 MPa) and homogenized (393 MPa) conditions are comparable and may remain within the experimental error. For comparison, the tensile properties of the reported HEAs and conventional structural materials at 700 ℃ are also listed in Table 7. Compared to others, the present alloy exhibits the relatively high σ_y, σ_{UTS}, and plastic deformation.

4.3.5. Thermodynamic Properties and Phase Equilibrium

Figure 41a presents the calculated solidification path for the AlCoCrFeNi alloy by the Scheil model [112], which indicates that the primary solidified phase is B2. Then the A2+B2 phase will form with decreasing temperature. According to the simulation shown in Figure 41a, only 7 % volume fraction of the liquid is consumed to form the primary B2, and the next 20 % volume fraction of the liquid forms A2+B2 mixture phases. Then, the rest of the liquid solidifies into A2+B2+A1 structures. Furthermore, the temperature drops less than 15 ℃ (1,189 ℃ to 1,175 ℃) for the A2+B2+A1 mixture to finish solidification. The calculated results (Figure 41a) are very

consistent with the experimental ones: primary-solidified dendrites consist of A2+B2 phases, while secondary-solidified interdendrites are composed of A2+B2+A1 phases.

An equilibrium line calculation is also performed for the AlCoCrFeNi alloy, as shown in Figure 41b. All four phases, A2+B2+A1+σ, are all presented in the equilibrium phase diagram. As exhibited in the calculation, the A1 phase is in equilibrium with the A2 phase after the heat treatment, which is consistent with the experimental data in the present work and those in the literature [32, 36]. The calculated volume fractions of A2 and B2 are similar to the experimental results, while those of A1 and σ are different from the experimental results (Figure 41b and Table 6). Note that the σ phase does form in the temperature range of 460 - 800 ℃ (Figure 41b), and it is also observed in the AlCoCrFeNi-HP microstructure (Figure 37). However, AlCoCrFeNi-HP was annealed beyond the thermodynamically-predicted temperature range (460 - 800 ℃). Several possible reasons are proposed in Section 5.2.

Overall, the thermodynamics prediction, presented in Figure 41, agree qualitatively with the experimental observation in this investigation. The validity of thermodynamic modeling and differences between modeling and experimental results are discussed in Section 5.2.

4.4. Discussion

4.4.1. Reasons for the Improvement of Ductility

The present work shows a significant effect of homogenization heat treatment on the microstructure and tensile properties of the AlCoCrFeNi HEA. Most importantly, the number and amount of phases increase and the tensile elongation at 700 ℃ increases from 1.0 % to 11.7 %. How the high-temperature properties of HEAs relate to those of other structural materials and how they depend on heat-treatment conditions and compositions are shown in Table 7 and Figure 42.

For example, the tensile behavior of AlCoCrCuFeNi HEA in as-cast and forged conditions are very different: from high strength with limited elongation to low strength with decent elongation. The tensile behavior of $Al_{0.5}$CoCrCuFeNi HEA in rolled and annealed condition have similar phenomenon. This trend indicates that proper heat treatments can be applied to HEA system by changing microstructures and tailoring properties. This is also exactly the same situation in the present study. Compared to the AlCoCrFeNi-AC alloy, the AlCoCrFeNi-HP alloy exhibits higher combined properties, such as elongation and plastic deformation.

The size scales of the microstructures are very different in two conditions (as-cast and homogenized). The AlCoCrFeNi-AC alloy shows 50 - 100 nm lamella of A2+B2 phases. Dislocation motion through these finely-spaced interfaces is very difficult. Similarly, TiAl-based alloys also have very limited tensile ductility at room temperature because of their fully-lamellar structures ($\alpha_2+\gamma$) generally observed in cast conditions [115]. However, the brittleness even up to 700 ^{o}C in the AlCoCrFeNi-AC material is probably due to the difficulty of forcing dislocation motion through the alternating thin lamella of different crystal structures.

The lamellar structure explains the poor ductility. Our TEM results indicate that the boundary planes between the A2 and B2 lamellas are often of 100 plane with <010> in the long directions of the lamella. The slip systems active in these highly alloyed phases are unknown, but based upon extrapolations from the knowledge of B2-NiAl and A2-Fe, the dominant slip planes are likely 110-type. Burger's vectors are similarly unknown, but a<110> in B2 and a/2<111> in A2 are likely and assumed here. Atom probe tomography (Figure 43a) indicates that the lamellas contain high densities of fine precipitates of the opposite phase. A HAADF image from STEM with a sketch of AlCoCrFeNi-AC specimen shows an A2+B2 lamellar structure at the atomic level (Figure 43b). Both the lamella boundaries and the fine precipitates likely act as strengthening

obstacles to reduce the ductility of the material. For example, if a lamella is 50 nm wide and oriented with <100> in its long direction, then 110-plane dislocation will have only ~ 50 or ~ 70 nm of the distance from one edge of the lamella to the other (Figure 43c). This distance will be further interrupted by the fine particles, which will require dislocation climb, cross slip, cutting, or bowing, to bypass. The assumed a<110> B2 dislocations will not easily transfer into the assumed a/2<111> burger's vector in A2, and vice-versa. Thus, dislocations will probably have to climb, cross-slip, or bow around the nanoparticles, rather than cut the particles. Those dislocations that do pass through the particle forest will then probably pileup at the lamellar interface, again due to the difficulty of the shear transfer from the $a<110>_{B2}$ to $a/2<111>_{A2}$ burger's vectors. All of these factors together will result in the increased shear stress required to drive dislocations through the structure, and, therefore, reduced ductility.

In the homogenized condition instead, due to breaking up the A2+B2 lamella into larger domains (Figure 38), giving the dislocations longer glide-lengths before hitting an obstacle may be the main reason for the improvement of ductility but lower yield strength (Figure 40 and Table 7). Furthermore, the other important reason may be the occurrence of the relatively-ductile A1 phase free of precipitates. Our nanoindentation results revealed that the A1 phase has a hardness of only 4.3 ± 0.2 GPa, which is less than half of the B2 phase with a hardness of 8.9 ± 0.4 GPa at room temperature. Liu et al. also confirmed that the A1 phase has a lower yield strength than the B2 matrix in the $Al_{0.8}$CoCrCuFeNi HEA at room temperature [116]. Generally, a phase with a lower hardness and a lower yield strength will possess a higher ductility, even more at elevated temperatures. This trend may also happen in our case, which means that the appearance of a large amount of a relatively ductile A1 phase along grain boundaries in the homogenized condition contributes to the improvement of the ductility, compared with the as-cast condition with a very

few amount of A1 nanoprecipitates. In addition, the thermal treatment (HIP+homogenization) after casting may reduce defects produced by casting and relieve residual stresses during fast-cooling drop-casting.

4.4.2. Validity of Thermodynamic Modeling

Based on the thermodynamic modeling for the as-cast condition, the A1 phase only forms over less than a 15 ℃ interval (1,189 ℃ to 1,175 ℃ in Figure 41a). Thus, the A1 phase may not be able to form or only a very small amount of A1 forms due to the high cooling rate (non-equilibrium) of the alloy preparation using the drop-casting method. There is a very small amount (less than 1-2 %) of fine precipitates of an additional phase, which has an A1 structure and is enriched with Co (Figure 34d), which is consistent with our Scheil modeling. Also, the simulation shows that the structure is a mixture of the A2+B2 owing to this special solidification (note that NiAl-rich dendrites solidified first, and then NiAl-poor interdendritic regions formed), which is consistent with the experimental observation for the microstructures of AlCoCrFeNi-AC alloy in the present work. Note that the volume fraction of the A1 phase is ~ 50 % (Figure 41b), and we may not be able to obtain this amount, since the AlCoCrFeNi-HP alloy may not yet reach equilibrium due to the sluggish diffusion of elements in HEAs and the short annealing period (only 50 hours in the present study).

There is one main difference between thermodynamic-modeling predictions and microstructural characterizations. It is the presence of σ phases in the homogenized condition. As mentioned previously, the σ phase is observed in the microstructure of the AlCoCrFeNi-HP alloy, which was annealed at 1,150 ºC for 50 hours, beyond the thermodynamically-predicted existing temperature range (460 - 800 ℃). There are two possible reasons for this discrepancy. One reason

may be due to unreasonable thermodynamic parameters for the σ phase in the present thermodynamic model. The other reason may result from the localization of certain alloying elements within this alloy forming the σ phase. For example, a certain amount of Co can improve the stability of the σ phase at higher temperatures, up to 1,283 ℃ (such as the binary Co-Cr σ phase [117, 118]), which is higher than the annealing temperature of 1,150 ℃. Indeed, some amounts (24 at. %) of Co are observed in the σ phase, as presented in Figure 37(d) and shown in Table 5. Of course, it is also likely that the σ phase precipitated during slow furnace cooling (10 ^{o}C/min). Chou et al. [36] did not observe the σ phase at 500 ℃ and 550 ℃, which is not surprising, since the precipitation is a diffusion-controlled process, and a certain amount of phases are necessary for the phase identification by the regular lab X-ray diffraction.

Further experimental and thermodynamical investigations on these issues will be carried out in future studies. Specifically, systematic phase-transformation studies for the AlCoCrFeNi alloy will be necessary, especially in the solid state, for the quantitative comparison. As mentioned previously, the current Al-Co-Cr-Fe-Ni database was developed using the available experimental data of the 10 constituent binaries and 10 constituent ternaries. This database needs further validation by the 5-component alloys.

4.4.3. A2+B2 Nano-lamellar Structure in HEA Systems

If we define BCC HEA as a single-phase A2 (a disordered BCC solid solution) structure with no elemental segregation, many reported single-BCC HEAs with one lattice parameter may fail to meet this criterion. They are usually elemental-segregation dendritical structures (dendrites and interdendrites) [4, 5, 26, 119], and people tend to call them as element-rich, such as NiAl-rich in 3d-transition-metal-based HEAs, and TaW-rich in refractory HEAs. Actually, those alloys may

be composed of A2 and B2 phases. NiAl-type B2 structure in HEA systems are usually very stable due to its very negative enthalpy [14]. Once B2 phases formed during cast processing, solidified microstructures were difficult to be homogenized through regular heat treatments (compare Figure 33 with Figure 37). If a single-phase A2 HEA is going to be identified, only an X-ray diffraction pattern with no (100) superlattice peak is not enough. Formed by the eutectic reaction during solicitation (Figure 41a), A2 and B2 could have very small lattice parameter mismatch [14]. This trend may be the reason why only one lattice parameter can be found via X-ray diffraction pattern [4, 5, 26, 119]. This feature is also very common in the Ni-based superalloy (γ and γ') and FCC HEA systems [2, 106, 113]. To the current authors' knowledge, single-phase FCC or BCC HEAs can only be found in a few publications [120-123].

In the present study, the A2+B2 nano-lamellar structures also coexist in both NiAl-rich dendrites and NiAl-poor interdendritic regions in the as-cast condition, even though only one lattice parameter can be found via synchrotron X-ray diffraction pattern (as-cast in Figure 39). Furthermore, the NiAl-rich dendrite regions are enriched with the B2 phase, and the NiAl-poor interdendrite regions are enriched with the A2 phase. This trend has been confirmed by SEM with EDS/EBSD and TEM studies, as shown in Section 4.1. To further investigate this trend, the selective etching technique [124-126] was applied. As shown in Figure 44, nanoprecipitates with 50-100 nm were etched away both in NiAl-rich dendritical and NiAl-poor interdendritical regions, and yet another kind of line-shape nanoprecipitates might be only found in NiAl-poor regions. The selectively-etched morphology (Figure 44) quite agrees with the previous TEM results (Figure 34): etched-away nanoprecipitates are the Cr-rich phase with an A2 structure; etched-away line-shape nanoprecipitates are the Co-rich phase with an A1 structure; and remaining are the NiAl-rich matrix with a B2 structure. This trend also agrees the original function of the selective etchant

(Kalling's No.2) in steel which does attack ferrite (A2 structure) and slightly attack the austenite (A1 structure) [127]. Furthermore, based on our thermodynamic calculation (Figure 41a), A2+B2 tend to be firstly solidified together to form dendrites (NiAl-rich regions in this study), and then A2+B2+A1 are solidified to form interdendritically (NiAl-poor regions in this study) during fast cooling. This feature may be the reason why line-shape nanoprecipitates with an A1 structure can only be found in NiAl-poor interdendritic regions (Figure 44). Thus, we have many indications that both dendrites and interdendritic regions are fine A2+B2 nano-lamellar structure (NiAl-rich dendrites enriched in B2, and NiAl-poor interdendrites enriched in A2), while another kind of line-shape nanoprecipitates with A1 structure only exist in NiAl-poor interdendritic regions.

Similar phenomena are also found in AlCoCrFeNi-HP. As presented in Figure 45, Cr-rich nanoprecipitates with an A2 structure are embedded in the NiAl-rich B2 matrix, while CoCrFe-rich A1 phases are free of precipitates. Note that the structure type of a pure Cr element is A2, which further confirm our hypothesis.

Above all, the microstructures and mechanical behavior of one alloy, AlCoCrFeNi, have been carefully studied in two conditions (as-cast and homogenized), as summarized in Figure 46. As confirmed by both experiments (SEM/EDS, EBSD, TEM/STEM, APT, and Synchrotron) and simulations (CALPHAD), the homogenization treatment results in phase evolution: from two major phases (A2+B2) in the as-cast condition to four major phases (A2+B2+A1+σ) in the homogenized condition. Moreover, both NiAl-rich dendrites and NiAl-poor interdendrites have a fine A2+B2 nano-lamellar structure, but different volume fractions of A2 and B2. The very different microstructures in the two conditions exhibits similar σ_{UTS} but a noticeable increase in the tensile ductility after the heat treatment (HIP and homogenized).

4.5. Conclusions

In summary, we discuss how as-cast and homogenized phases can be identified, what phases are usually found in the as-cast and homogenized conditions, and what the thermodynamics and kinetics of phase transformations are in the AlCoCrFeNi HEA, as shown in a summary cartoon of Figure 46.

(1) Using SEM/EDS, EBSD, STEM and high-energy synchrotron X-ray diffraction, the microstructure of the AlCoCrFeNi-AC alloy are identified to have clear intra-granular dendritic structures containing two regions, NiAl-rich dendrites and NiAl-poor interdendritic regions. The TEM/STEM and the selective etching technique further confirm that both NiAl-rich and NiAl-poor regions have a fine A2+B2 nano-lamellar structure. The difference between two regions is that the NiAl-rich dendrite regions are enriched with the B2 phase, while the NiAl-poor interdendrite regions are enriched with the A2 phase as well as a small amount of A1 nanoprecipitates (less than 1-2 %).

(2) Four phases, A2, B2, A1, and σ phases, are found in the AlCoCrFeNi-HP. A2 nanoprecipitates embedded in the B2 matrix are also found in the homogenized condition, while blocky wall-like A1 phases along boundaries are identified and free of precipitates.

(3) A noticeable increase in the tensile ductility occurs after the HIP and homogenized treatment. During tensile testing at 700 ℃, the elongation of the homogenized alloy is 11.7 %, while the as-cast alloy show the elongation of only 1.0 %. The ultimate tensile strength at 700 ℃ is almost unaffected by the heat treatment, 400 MPa and 393 MPa, respectively.

(4) The reason for the limited elongation of the AlCoCrFeNi-AC alloy may be that dislocation motion through these finely-spaced interfaces (50-100 nm) is very difficult, resulting higher yield strength. The improvement of ductility for the AlCoCrFeNi-HP alloy may be due to breaking up the A2+B2 lamella into larger domains, the occurrence of relatively ductile FCC phase, reduced casting defects, and relieved residual stress.

(5) The CALPHAD thermodynamic modeling, including the solidification path and the phase map, are well consistent with the experimental data.

The authors believe that this study will pave the way for the characterization and optimization of the AlCoCrFeNi alloy and the microstructures of the similar HEAs system. Meanwhile, it is the authors' hope that this study will draw more attention of scientists to research homogenized HEAs with balanced mechanical properties, perhaps with multiple phases, rather than the only pursuit of single-phase solid-solution HEAs, which is also emphasized by Miracle et al. [28]. It even provides support toward the composition design of HEAs based on the composition-structure-property relationship. The fundamental understanding of microstructures will lay down the foundation for the discovery of new HEAs with improved materials properties in extreme environments. HEAs as a new class of advanced materials with competitive high strengths at elevated temperatures and with reasonable ductility may become the next-generation structural materials. The development of such novel materials will bring significant impacts on some extreme environmental engineering for wide applications.

Chapter 5. Fatigue Behavior of a Wrought Al0.5CoCrCuFeNi Two-Phase High-Entropy Alloy

Fatigue behavior of a cold-rolled two-phase $Al_{0.5}$CoCrCuFeNi high-entropy alloy (HEA) was studied. Some specimens were fabricated using commercial-purity raw materials, while others were manufactured with high-purity components. Scatter in the fatigue life of the commercial-purity samples was found in the stress vs. lifetime plot (S-N curve). However, the high-purity samples showed less scatter, and fatigue life is predictable using traditional fatigue statistics. The fatigue property of the alloy is comparable with and may even outperform many commercial alloys. Fatigue cracking is promoted by shrinkage pores with a size of ~ 5 μm, while mechanical nanotwinning were found to be the main deformation mechanism before crack initiation and during crack propagation by transmission electron microscopy (TEM). Two orientations of dense nanotwins were found at the crack initiation site, while less-dense nanotwins were found away from the crack initiation site. The nanotwinning behavior resulted in strengthening of the alloy and consequently high fatigue strength (810 MPa). Moreover, statistical models were applied to predict fatigue life, suggesting that using improved fabrication processes and/or high-purity raw materials may enhance the fatigue behavior by reducing the number of fabrication microcracks and pores in the test samples.

5.1. Introduction

Metallic structural alloys with excellent mechanical properties at elevated temperatures always remain in high demand for the aerospace and nuclear industries. Modern and advanced technologies not only strongly depend on the existing properties of metals, but urgently call for

even better metals with unique properties [1]. Recently, a new strategy for the development of high-strength and high-temperature alloys, called high-entropy alloys (HEAs) and/or multi-principal-element alloys (MPAs), has been proposed and developed [2, 4, 7, 14, 27, 95, 96, 105, 128]. Researchers generally assume that such alloys will lead to complex and brittle intermetallics. However, single face-centered-cubic (FCC) and/or body-centered-cubic (BCC) phases have been found in many HEAs systems, such as $Al_xCoCrCuFeNi$ [14, 34, 39, 95, 106] and $Al_xCoCrFeNi$ [4, 14, 40, 122]. When the number of elements, *N*, is equal or larger than 5 and the concentrations of each of the alloying elements are between 5 and 35 atomic percent (at. %), the high mixing entropy can significantly reduce the Gibbs free energy and stabilize solid-solution-like phases with relatively simple crystal structures, compared to intermetallic phases, especially at high temperatures [2, 5, 18].

If we seek for the applications in the aerospace industry or other fields, besides monotonic loading, the fatigue behavior and lifetime prediction are one of the most influential factors, which are required to be studied and explored, yet rarely reported in HEA systems. The first and only publication so far concerning the fatigue behavior of $Al_{0.5}CoCrCuFeNi$ HEAs came from our group, Hemphill et al [7]. Their study showed promising fatigue resistance characteristics due to the prolonged fatigue lives of various samples at relatively high stresses. Compared with conventional alloys, such as steels, Ti-based alloys, and advanced bulk metallic glasses (BMGs), their results suggested that the fatigue behavior of HEAs compared favorably.

However, three main issues remain to be explored further. The first issue is that the fracture mechanism in four-point-bending fatigue has not been clearly defined [7]. The precise knowledge of the fracture mechanism is essential for understanding their promising fatigue resistance and developing life prediction capabilities. Thus, microstructure evolution and crack initiation during

fatigue test was investigated. The second issue is that a large amount scattering was observed in the stress vs. lifetime plot (also called S-N curve) [7]. These authors believe that the reason of the scatter is due to microstructural defects, such as aluminum oxide inclusions and microcracks which were introduced during sample fabrication and thermal heat treatments, including initial casting and cold rolling. Thus, based on what has been found [7], two new sets of HEAs were successfully fabricated: (1) shrinkage pores and macrosegregation in the as-cast ingot were mechanically removed by machining and cold-rolling; (2) besides removing pores and segregation, high purity elements were used as raw materials in order to reduce the extent of oxide inclusions and microcracks.

The third issue that was investigated is the connection between defects and fatigue endurance limits of HEAs by means of statistic fatigue-life modeling [7]. The fatigue-endurance limit is usually treated as a constant for a material, and it is a common practice to report the endurance limit of a material to be the stress level below which failure will not occur before an arbitrary large number of cycles, usually 10^7 cycles is reached. In addition, the S-N data are usually analyzed by a simple linear regression approach, which cannot adequately take into account for the significant scatter in the data. Nelson [129] first suggested modeling the endurance limit of a material as a random variable instead of a fixed constant; that is, test specimens have different endurance limits according to some "strength distribution." Pascual and Meeker [66] later developed a random endurance-limit fatigue-life model to describe (1) the dependence of fatigue life on the stress level and (2) the scatter in the S-N data. They applied their model to analyze the four-point-bending fatigue data of the carbon eight-harness-satin/epoxy laminate, and their results provided evidence suggesting a random nature of the fatigue-endurance limit. They argued that the randomness in the endurance limit is due in part to the location, orientation, size, and number

of defects (e.g., cracks) in the material, which are random themselves. Wallin [67] also examined the statistical aspects of the fatigue-endurance limit, and observed that the variation in endurance limit has a pronounced effect on the scatter in fatigue life close to the endurance limit. Lognormal, normal, and Weibull distributions have been proposed in the literature to describe the randomness in the endurance limit [67]. In order to partially understand the scatter in the fatigue life and the connection between defects and the fatigue-endurance limit of HEAs, this study adopts the random endurance-limit fatigue life model to analyze the S-N data of $Al_{0.5}$CoCrCuFeNi HEAs obtained from three conditions of samples (two from this study and one from [7]) using different fabrication processes and/or different purity grades of the raw materials.

5.2. Results

5.2.1. Microstructural Characterization before Fatigue Testing

Microstructural characterization before the fatigue tests was performed using SEM with EDS element mapping, TEM, and Synchrotron XRD. Figure 48 shows Condition-3 $Al_{0.5}$CoCrCuFeNi microstructures on three sides [cold-rolled surface, electric-discharge-machining (EDM) cut surface, and cross section] with SEM-EDS elemental mapping of six principal elements, including Al (red), Co (green), Cr (blue), Cu (yellow), Fe (cyan), and Ni (magenta),. Cu segregation is clearly seen from the elemental mapping. Suffering the same fabrication process (cast + annealed + cold-rolled), the microstructures of three conditions are very similar, consisting of two phases: (1) continuous matrix, formed from the primary dendrite phase (dark color), and (2) Cu-rich second phase (light color), developed from the Cu-rich interdendritic phase, which is consistent with previous studies [7, 34, 39, 59, 95]. For further investigation of Cu-rich interdendritic phase, the TEM was performed, as shown in Figure 49. TEM-EDS results

are shown in **Table 9** for the compositions of matrix phase and Cu-rich phase. In addition, image and diffraction analyses reveal that Cu-rich phase seen in SEM image in fact has a high density of nanoprecipitates which have FCC structure and a particle size of 5-10 nm. The nanoprecipitates are very probably Ni-,Al-rich clusters since Ni and Al has strong bonding with each other and tend to segregate to form final NiAl-rich B2 (ordered BCC) structure.

Figure 50 shows synchrotron X-ray line profiles of three conditions of $Al_{0.5}$CoCrCuFeNi HEA: black for Condition-1, blue for Condition-2, and red for Condition-3. Synchrotron X-ray profiles of three conditions are similar, only showing a single FCC structure with lattice parameter of 0.362 ± 0.002 nm. As two phases can be distinguished in SEM images (Figure 48), it demonstrates that the two phases are FCC and enjoy close match in lattice parameter (0-1%). The matrix and minor are hereafter denoted by FCC-1 and FCC-2.

An ordered structure indicated by the (100) super-lattice peak is not present in the Synchrotron XRD patterns, which reveals that no ordered FCC (called $L1_2$) phase are found in this alloy. The inserted Synchrotron 2-D diffraction pattern (it only shows the Condition-3 here, and the Conditions 1 and 2 show the same phenomenon) shows a texture, which is due to cold-rolling.

5.2.2. S-N curves of Four-point-bending Fatigue

High-cycle four-point-bending fatigue test results are plotted as the maximum stress [the maximum stress calculated from Equation (2)] vs. the number of cycles to failure or run-out (10^7 cycles) to give the S-N curve, as shown in Figure 51. In general, the shape of the S-N curve of $Al_{0.5}$CoCrCuFeNi HEA is similar to those for other crystalline metals and amorphous metals [130-136]. The S-N curve shows a distinct endurance limit of about 800 MPa, which is below the yield strength of this alloy (1,284 MPa), and the ratio of the fatigue limit to tensile strength (1,344 MPa)

is about 0.59 [7]. These indicate that HEAs have favorable and/or greater endurance limits, and fatigue ratios comparable with steels and other conventional alloys. Above the endurance limit, the maximum stress exhibits a clear relationship with the number of fatigue cycles.

As seen from Figure 51, there is a noticeable extent of scatter at each stress level for regular-purity samples (black dots for Condition-1 and blue triangles for Condition-2, respectively). However, the Condition-3 (red squares) samples showed less scatter. For example, at a stress of 1,100 MPa, two failures of the Condition-2 samples are within an order of magnitude between 2.7×10^4 and 1.3×10^5 cycles while two failures of Condition-3 samples only between 6.0×10^4 and 9.8×10^4 cycles. At a maximum stress of 1,200 MPa, near the yield stress, 1,284 MPa, of the alloy [7], most failures are within an order of magnitude of each other, between 3.0×10^4 and 1.0×10^5 cycles. As the stress level decreases, especially near the range of the endurance limit, the spread in the maximum stress range between 800 and 850 MPa becomes more pronounced than at the greater maximum stress, which is characteristic of fatigue behavior [137]. Estimations of the endurance limits based on the stress ranges are within a lower bound of 800 MPa and an upper bound of 850 MPa. These values were chosen because the specimens reached 10^7 cycles without failure. The results reveal the general trend of the S-N data: the fatigue life increased with decreasing maximum stress level, as is normally observed for crystalline materials.

5.2.3. Fractography

The fracture surfaces were examined using SEM. Figure 52 presents the fracture surface of a Condition-3 specimen tested at a relatively high maximum stress of 1,100 MPa, with an R ratio of 0.1, in air and at room temperature. The topography of the fracture surface possesses very crystallographic features: (i) crack-initiation region, (ii) slow and stable crack-propagation region

with a crystallographic appearance and striations, and (iii) fast-fracture region with dimpled-overload [Figure 52(a)]. Under four-point-bending cyclic loading, the crack-initiation site could usually be identified at a corner of the tensile stress surface, by tracing the radial marks on the fracture surface, which pointed toward the origin of the fracture. Voids and/or inclusions were found in the higher magnification of the fatigue-crack-initiation region [Figure 52(b)]. It was confirmed that the cracks initiated from pores but the direction of striations were random, because the microcracks may form from several pores. Following crack initiation, the fatigue crack propagates randomly through and around pores, which indicates that the direction of fatigue striation has a variable path which has been changed owing to existing pores. The characteristic feature of the crack-propagation region exhibits a stair-step appearance with fatigue striations that formed due to the four-point-bending cyclic loading, as revealed by the SEM examination in Figure 52(c). Some areas in Figure 52(c) also exhibit a cleavage-like fracture surface, which means that the crack propagates in both ductile and brittle modes. The random directions of the fatigue striation in Figure 52(c) are consistent with those in the crack initiation region. These trends indicate that the crack propagation is crystallographic. The fast fracture region [Figure 52(d)] contains typical ductile fracture features, such as dimples, which indicates that some ductility in the alloy is present.

The local plastic deformation can be seen as the development of slip lines and slip bands after a significant number of loading cycles, which eventually reach a size such that they can act as the initiator of the fatigue crack, followed by crack propagation, as shown in Figure 53. Some oxides were found at high magnification in the crack initiation region. As shown in Figure 54(b-c), the area adjacent to the crack initiation site experiences significant plastic deformation due to stress concentration, followed by crack propagation with slip bands. Found in Figure 53(e) and

Figure 54(b), peaks (extrusions) and troughs (intrusions) of the surface of the component were formed due to the movement of material along slip planes, which serve as stress risers to create microcracks and facilitate crack propagation. Microcracks nucleated along planes of high shear stress can be found, as shown in Figure 55 and Figure 56.

5.2.4. Deformation Substructures

To examine the nature of cyclic strain localization and damage accumulation mechanisms under cyclic loading, TEM-FIB specimen were removed from a failed specimen with a lifetime of 2,069,447 cycles at 1,200 MPa in Condition-1. Three different locations, including crack initiation site, adjacent to crack initiation site, and away from the crack initiation site, were the major focus and the TEM analyses are shown in Figure 57. Figure 57(c) indicates that low nanotwin density associated with tangled dislocations already exists in the cold-rolled specimens before fatigue testing since the location away from crack initiation site and free from plastic deformation shows such a structure. From Figure 57(a) and (b) taken from the locations with severe cyclic deformation (at the crack initiation site) and moderate deformation (adjacent to the crack initiation site), respectively, it can be found that more nanotwins were induced during cyclic loading before crack initiation. In particular, two sets of nanotwins were formed at the crack initiation site as compared to one set of twinning seen in Figure 57(b) and (c). Figure 58 shows further investigation on FIB specimens at the crack initiation site. Two different-orientation sets of dense nanotwins and a high density of tangled dislocation [Figure 58(a)] were clearly identified. Diffraction patterns [Figure 58(b)] with zone axis [011] and three chosen spots [Figure 58(c)] for dark images indicate that the orientations or twinning direction of two-set twins are $[2\bar{1}1]$ (green color) [Figure 58(e)] and $[21\bar{1}]$ (blue color) [Figure 58(f)], respectively. The result of TEM-EDS in this area (Table 9) confirms that it is the matrix (FCC-1), rather than the Cu-rich phase (FCC-2).

Overall, TEM observations suggest that the main crack initiation mechanism: the severe cyclic stress action on the maximum-tensile-stress sites of specimens will induce more nanotwins and more sets of nanotwins before crack initiation. The increased density of nanotwins brings larger work hardening at the sites and gives higher resistance to crack initiation due to smaller stress concentration by providing more twin boundaries. As a result, the fatigue strength level is expected to be higher. This basically explains the reasons why the present alloys have favorable and/or greater endurance limits, and fatigue ratios comparable with steels and other conventional alloys. Further discussion on this will be presented in the following section.

5.3. Statistical Modeling

5.3.1. Fatigue-life Modeling

This section outlines the fatigue-life model with a random endurance limit. A commonly-used analytical representation of the S-N curves, considering the fatigue-endurance limit, is given by [138]

$$n = \begin{cases} c(s-\gamma)^{-d}, & s > \gamma, \\ \infty, & s \le \gamma, \end{cases} \tag{3}$$

where n, s, and γ, are, respectively, the cycles to failure, the applied stress, and the fatigue-endurance limit, and c and d are positive material parameters. Taking the natural logarithm on Equation (3) results in

$$\log(n) = \begin{cases} \beta_0 + \beta_1 \log(s-\gamma), & s > \gamma, \\ \infty, & s \le \gamma, \end{cases} \tag{4}$$

where $\beta_0 = \log(c)$ and $\beta_1 = -d$. To account for the statistical scatter in the observed fatigue-life data, a random error term, ε, is introduced to Equation (4) such that the fatigue life, n, is modeled by

$$\log(n) = \beta_0 + \beta_1 \log(s - \gamma) + \varepsilon, \quad s > \gamma. \tag{5}$$

It is assumed that the fatigue-endurance limit, γ, is a random variable following certain probability distribution. Let $V = \log(\gamma)$, and suppose that V has a probability density function (pdf) given by

$$f_V(v; \mu_\gamma, \sigma_\gamma) = \frac{1}{\sigma_\gamma} \varphi_V\left(\frac{v - \mu_\gamma}{\sigma_\gamma}\right), \tag{6}$$

where μ_γ and σ_γ are the location and scale parameters, respectively. If $\varphi_V(\cdot)$ is the standardized normal pdf, i.e., $\varphi_V(z) = \exp(-z^2/2)/\sqrt{2\pi}$, the endurance limit, γ, follows the lognormal distribution. If $\varphi_V(\cdot)$ is the standardized smallest extreme value pdf, the endurance limit is then a Weibull random variable.

Let $x = \log(s)$ and $W = \log(n)$. Then conditioned on a fixed value of $V < x$, the conditional pdf of W is assumed to be given by

$$f_{W|V}(w; \beta_0, \beta_1, \sigma, x, v) = \frac{1}{\sigma} \phi_{W|V}\left(-\frac{w - [\beta_0 + \beta_1 \log(\exp(x) - \exp(v))]}{\sigma}\right), \tag{7}$$

with location parameter $\beta_0 + \beta_1 \log(\exp(x) - \exp(v))$ and scale parameter σ. Again $\varphi_{W|V}(\cdot)$ may be assumed to be the standardized normal or smallest extreme value pdf. The marginal pdf of W is, then, given by

$$f_W(w;x,\boldsymbol{\theta}) = \int_{-\infty}^{x} \frac{1}{\sigma\sigma_\gamma} \varphi_{W|V}\left(\frac{w-[\beta_0+\beta_1\log(\exp(x)-\exp(v))]}{\sigma}\right)\cdot\varphi_V\left(\frac{v-\mu_\gamma}{\sigma_\gamma}\right)dv, \quad (8)$$

where $\boldsymbol{\theta} = (\beta_0,\beta_1,\sigma,\mu_\gamma,\sigma_\gamma)$. The marginal cumulative distribution function (cdf) of W is given by

$$F_W(w;x,\boldsymbol{\theta}) = \int_{-\infty}^{x} \frac{1}{\sigma_\gamma} \Phi_{W|V}\left(\frac{w-[\beta_0+\beta_1\log(\exp(x)-\exp(v))]}{\sigma}\right)\cdot\phi_V\left(\frac{v-\mu_\gamma}{\sigma_\gamma}\right)dv, \quad (9)$$

where $\Phi_{W|V}(\cdot)$ denote the conditional cdf of W given V. The distribution functions given by Equations (8) and (9) do not have closed forms. Numerical methods will be used to evaluate them.

Pascual and Meeker [66] showed that this random endurance limit model possesses characteristic that are usually observed in fatigue-life data. Their results demonstrated that this model can adequately describe curvature in the S-N relationship and the increase in scatter in the fatigue life as the stress level decreases.

5.3.2. Computations and Results

This section presents the computational results of applying the random endurance limit model to analyze the S-N data of three conditions of $Al_{0.5}CoCrCuFeNi$ samples. The fatigue life data of different conditions of $Al_{0.5}CoCrCuFeNi$ samples were analyzed separately using the random endurance-limit model, as shown in Section 4.1. For each condition, we denote the fatigue-life data by (n_i, s_i, δ_i), i = 1,2,…,m, where m is the total number of observations in that condition, s_i is the applied maximum stress for the ith sample, and the binary indicator, δ_i, specifies whether n_i is a failure or a censored (runout) observation. Herein δ_i = 1 when n_i is the observed cycles to fatigue failure, and δ_i = 0 when n_i is a censored observation, i.e., the fatigue test is terminated after

n_i cycles but the sample has not failed. The unknown model parameters, $\boldsymbol{\theta}$, are estimated by the maximum likelihood method [139], which maximizes the likelihood function of the data given by

$$L(\boldsymbol{\theta}) = \prod_{i=1}^{m} \left[f_W(w_i; x_i, \boldsymbol{\theta}) \right]^{\delta_i} \left[1 - F_W(w_i; x_i, \boldsymbol{\theta}) \right]^{1-\delta_i}, \tag{10}$$

where $w_i = \log(n_i)$ and $x_i = \log(s_i)$, for $i = 1,2,\ldots,m$, and $f_W(w_i; x_i, \boldsymbol{\theta})$ and $F_W(w_i; x_i, \boldsymbol{\theta})$ are defined by Equations (6) and (7), respectively. Note that in the computation, n_i and s_i are scaled to have units of million cycles and 10^3 MPa, respectively, to improve numerical stability.

We assumed that $\varphi_V(\cdot)$ and $\varphi_{W|V}(\cdot)$ are both standardized normal pdf. Table 10 lists the maximum likelihood estimates of the model parameters for the three conditions of samples. Using the maximum likelihood estimates of the model parameters, we can predict the S-N behavior by estimating the *p*-quantile fatigue life as a function of the stress. The *p*-quantile fatigue life at the stress level, *s*, denoted by $n_p(s)$, is defined as

$$\Pr(n \le n_p(s); s, \boldsymbol{\theta}) = p = F_W(\log(n_p(s)); \log(s), \boldsymbol{\theta}). \tag{11}$$

When $p = 0.5$, $n_{0.5}(s)$ is the median fatigue life at the stress level, *s*, which can be used to describe the average stress-life behavior. Figure 51 shows the predicted $n_{0.5}(s)$ for the three conditions of HEA samples. As shown in

Figure 51, the random endurance limit model can reasonably capture the stress-life relationship for all three conditions.

The endurance limit is of particular interest in this study. The endurance limit, γ, is assumed to follow the lognormal distribution with the location parameter μ_γ and scale parameter σ_γ. Once the two parameters are estimated, we can compute some characteristics of the random endurance

limit. The median endurance limit computed by $\exp(\mu_\gamma)$ and the standard deviation of the endurance limit computed by $\sqrt{\exp(\mu_r)\exp(\sigma_\gamma^2)(\exp(\sigma_\gamma^2)-1)}$ can be used to measure the average endurance limit and the variability in the endurance limit, respectively [140].

Table 11 shows the median endurance limits and the standard deviations of the endurance limits for the three conditions of the samples. Because *V*, the logarithm of the endurance limit, is assumed to follow the pdf given by Equation (6), we can derive the pdf of the endurance limit itself, which is given by

$$f(\gamma;\mu_\gamma,\sigma_\gamma)=\frac{1}{\gamma\sigma_\gamma}\varphi_V\left(\frac{\log(\gamma)-\mu_\gamma}{\sigma_\gamma}\right). \tag{11}$$

Figure 59 depicts the $f(\gamma;\mu_\gamma,\sigma_\gamma)$ functions for the three conditions of HEA samples.

5.4. Discussion

5.4.1. Fatigue-Strengthening Mechanism in Relationship to Twinning Behavior

Low density of existing nanotwins with tangled dislocations in the $Al_{0.5}$CoCrCuFeNi alloy were believed to be introduced during the cold rolling process as mentioned in Section 3.4. Therefore, elastic and/or plastic strains were accommodated in structure with existing nanotwins and tangled dislocations prior to fatigue crack initiation. This also occurs in the case of supersaturated carbon in martensite, which increases the twinning to accommodate the strains in the Fe lattice due to carbon [141]. Then, fatigue cracks were initiated at heterogeneous nucleation sites, either preexistent defects (inclusions, gas pores, or local soft spots) [137], or twin boundaries,

or both. Since more nanotwins were found at and adjacent to the crack initiation site where severe deformation and moderate deformation occurred, respectively, as shown in Figure 57 (a-b), nanotwinning is expected to be the preferred mode for deformation before crack initiation and during propagation, and thus be the principle mechanism for cyclic plastic deformation in the present alloy.

Nanotwins in the alloy were formed during the cold-rolling and cyclic loading. In particular, those nanotwins during cyclic loading brought strengthening for the alloy and consequently high fatigue strength (810 MPa). The reasons for this are further considered. First, the formation of nanotwins results in continuous grain fragmentation because of the formation of new interfaces. The new twin boundaries act like high-angle grain boundaries, effectively reducing the dislocation mean free path, causing twinning-induced strengthening [34, 121]. The larger work-hardening due to dynamic microstructure refinement is also referred to as the dynamic Hall–Petch effect [142].

Conventional deformation twins are usually in the same order of grain size and also found to be microtwins and nanotwins in some special alloys with low stacking fault energy such as Hadfield manganese steels and 316L steels [143], so nanotwins in this HEA is also unique. Nanotwins were also seen at cryogenic temperatures in another HEA, CoCrFeMnNi [121]. The formation of nanotwins is believed mainly due to two principle reasons: low stacking fault energy (SFE) and high strength, which has been discussed for the present alloys [34]. Low SFE could reduce the critical stress needed to nucleate twin and thus preferably promotes nucleation of nanotwins. The low SFE is attributable to the fact that FCC matrix in HEAs contains an extremely large amount of solutes which can effectively lowering the overall energy of stacking fault by Suzuki interaction [144, 145].

5.4.2. Reasons for Data Scatter

The variability in fatigue behavior is well known. This is true for cycles to failures in our case, but if the materials are stable, S-N should not have extensive scatter, as shown in the Condition-3 of $Al_{0.5}$CoCrCuFeNi HEA (Figure 51). The reason for the extensive scatter is that, in addition to three basic factors (stress variation, peak values, and cycles), there are other variables, such as stress concentration, corrosion, temperature, overload, metallurgical structure, and residual stresses which can affect the propensity for fatigue.

Bending fatigue produces stress gradient, which are tensile at the bottom surface, decrease with increasing distance into the component, and then become compressive. Fatigue cracks generally initiate at a tensile surface, and a certain size of shrinkage pores acting as stress risers, decrease the time to nucleation and thus degrade fatigue life. Dislocations usually play a major role in the fatigue crack initiation phase [137]. In the present study, since there might have stress risers such as shrinkage pores and preexisting cracks due to fabrication at or near surface. As shown in Figure 47, stress concentration at these defects will cause the local microscopic stress to exceed the yield strength (1,284 MPa), while the maximum stresses of the rest area were still below the yield strength of the material (Figure 51). In this case, upon repeated fatigue loading, plastic deformation occurred locally in the alloy [146, 147]. Then, extensive scatter occurred depending if the specimens had shrinkage pores and preexisting cracks. After carefully examining cross-sections of as-received specimens, microcracks are much less content in Condition-3, while porosity is barely seen in all three conditions (Figure 47). This is the principle reason for reduced scatter in Condition-3.

Besides, some oxides were found, as shown in Figure 54c. They were formed during melting and heat treatment. If many oxides were located near the bottom surface in the specimen, the tensile stress were more easily triggering cracks than the specimens without or having less oxides. The cycles to failure of the former would be much lesser than the latter, resulting in extensive scatter.

5.4.3. Fatigue-life Modeling

As shown in Table 10, the maximum likelihood estimates of the model parameters differ substantially among the three conditions of samples, indicating that the fabrication process and the purity level of the raw materials may have significant and complex effects on the fatigue behavior of the $Al_{0.5}CoCrCuFeNi$ HEAs. All the β_1 estimates are negative, implying that as the stress level increases the fatigue life, on average, decreases. No obvious trend was discovered concerning how improving the fabrication process and/or the raw materials affects the parameters β_0, β_1, or σ. However, as shown in Table 10 and Table 11 and Figure 59, improving the fabrication process and/or the raw materials clearly has positive effects on the fatigue-endurance limits. Conditions 2 and 3 have comparable median endurance limits, and they are higher than the median endurance limit of Condition-1. Moreover, the standard deviations show a clear decreasing trend from Condition-1 to Condition-3, indicating a reduction of variability in the fatigue-endurance limit from Condition-1 to Condition-3. Figure 59 also conveys the same information. In Figure 59, the endurance limits corresponding to the peaks of the $f(\gamma;\mu_\gamma,\sigma_\gamma)$ functions for Conditions 2 and 3 are almost identical and higher than that of Condition-1. The $f(\gamma;\mu_\gamma,\sigma_\gamma)$ function of Condition-3 has the least variability; while the $f(\gamma;\mu_\gamma,\sigma_\gamma)$ function of Condition-1 has the most variability.

The defects in the HEA samples, therefore, may have a significant effect on the fatigue-endurance limits (Figure 47 and Figure 53). A reduction of the defects may result in improved fatigue-endurance limits of HEAs. Because the median endurance limit measures the average endurance limit of the sample, it may be correlated with the average number of defects in the test samples. On the other hand, the standard deviation measures the dispersion in the endurance limits among different samples within the same condition, and it may be correlated to the homogeneity of defects in the cast material. Using an improved fabrication process and high-purity raw materials may reduce the average number of defects as well as enhance the uniformity of defect distribution in the material. Because the variation in endurance limit has a pronounced effect on the scatter in fatigue life, especially at low stress levels, the effect of defects on the fatigue-endurance limits may partially explain the scatter in the fatigue-life data shown in Figure 50. S-N Plots and Ashby maps for three conditions of HEAs and other materials are shown in Figure 62 [22, 148]. The black-dashed ellipse indicates the family of HEAs. Note that yield strengths and ultimate tensile strength of three conditions are used the published result [7]. Three conditions of HEAs lie outside the benchmarks established by conventional alloys and bulk-metallic glasses (BMGs). The fatigue and yield strengths of some BMGs may have greater than HEAs because BMGs do not have crystal defects, such as grain boundaries and dislocations. As expected, HEAs usually have much greater ductility than BMGs. Overall, HEAs have better combination of mechanical properties of both fatigue and yield strengths, compared to conventional structural counterparts.

5.5. Conclusions

The two-phase FCC $Al_{0.5}CoCrCuFeNi$ HEA shows a very promising mechanical property with a high yield strength (1,284 MPa), high fatigue strength (810 MPa), and significant ductility (7.6 %) (Table 12). Based on the observation in this study, the following conclusions can be drawn.

(1) The fatigue life decreases as the applied maximum stress levels increases, as is normally observed. The high-cycle fatigue tests of the Condition-3 samples (fabricated by high-purity elements) gives higher fatigue strength than Condition-1, and less scatter than Conditions 1 and 2 (fabricated by commercial-purity elements). The attributed reasons are due to preexisting microcracks, pores, and oxides.

(2) TEM observations suggest that nanotwinning is the main deformation mechanism before crack initiation and often during fatigue crack propagation. The main crack initiation mechanism is: the severe cyclic stress action on the maximum-tensile-stress sites of specimens will induce more nanotwins and more sets of nanotwins before crack initiation. The increased density of nanotwins brings larger work hardening at the sites and gives higher resistance to crack initiation due to smaller stress concentration by providing more twin boundaries.

(3) Nanotwins formation during fatigue test results in strengthening for this alloy, which gives greater endurance limits, and fatigue ratios comparable with steels and other conventional alloys.

(4) By employing a random endurance-limit fatigue-life model to explore the effects of defects on the fatigue-endurance limits of HEAs, results suggest that using improved fabrication processes and/or high-purity raw materials enhance the fatigue behavior by reducing the preexisting microcracks in the test samples.

Chapter 6. Corrosion-Fatigue Behavior of a Single-Phase Face-Centered-Cubic $Al_{0.3}CoCrFeNi$ High-Entropy Alloy

The high-cycle tension-tension fatigue behavior and failure mechanism of a single-phase face-centered-cubic (FCC) $Al_{0.3}CoCrFeNi$ multi-principal-element high-entropy alloy (HEA) were investigated in air and ocean water environment. The single-phase microstructure was confirmed using scanning electron microscopy with energy-dispersive x-ray spectroscopy (EDS) and electron backscatter diffraction (EBSD) imaging, and in-situ neutron diffraction. Subsequent to fatigue testing, a longitudinal section was prepared to examine the region just beneath the fracture plane in order to reveal the environmental-degradation mechanism. The intragranular fracture with no phase transformation and segregation was confirmed. Slow strain rate testing was performed, finding that the alloy was not susceptible to stress corrosion cracking in ocean water environment at a strain rate of 2×10^{-6} / s. Electrochemical properties, such as anodic and cyclic polarizations of this new advanced structural material were compared with conventional alloys, indicating that this alloy has lower corrosion potential and current, lower corrosion rate, and larger passivation range, compare to 316L stainless steel, and comparable to C-2000 nickel alloy. The present studies provide a fundamental understanding of the fatigue behavior and fatigue/environment interaction behavior and life prediction of the single-phase FCC $Al_{0.3}CoCrFeNi$ HEA.

6.1. Introduction

Corrosion of metallic materials is an electrochemical interaction between the metals or alloys and their environment, which is generally detrimental to the proper functions of materials

and must be prevented. The cost of corrosion in the United States (U.S.) is estimated to have increased from $276 billion in 1998 to $1 trillion in 2013, which is 6.2% of the U.S. gross domestic product (GDP) [68, 69]. Therefore, the study on the corrosion behavior and degradation mechanism of metals and alloys and the development of corrosion-resistant materials are of enormous economic benefits. Materials to be used in long-term applications as structural or functional materials are expected to possess satisfying corrosion resistance. Noble metals (e.g., Ag, Au, Pt, *etc.*) are stable and exhibit excellent corrosion resistance even in aggressive environments [70], but the scalability of noble metal applications is restricted by their high cost and poor mechanical properties [70]. Another category of corrosion-resistant materials includes stainless steels, titanium alloys, cobalt-chromium alloys, and so forth, which are widely used in industry. The underlying corrosion-resistant mechanism for these metals or alloys involves the formation of passive films on the surface, which protects the underneath metals or alloys from further corrosion. In addition to the alloy composition, the corrosion behavior of metallic materials is also determined by their microstructures [70]. For example, carbides at grain boundaries of stainless steels deteriorate their corrosion resistance due to the formation of susceptible Cr-depleted zones, which can be diminished by heat treatments [71]. Therefore, metallurgical factors, including alloying and processing (e.g., heat treatments) parameters, are also very important in the development and investigation of corrosion-resistant metals or alloys.

Recently, a novel class of advanced structural materials, called High-Entropy Alloys (HEAs) or Multi-Principal-Element Alloys (MPEAs), has been proposed and developed [2, 3, 5-7, 11, 13, 14, 27, 91, 149-151]. Compared with conventional alloys containing one or two principal elements, HEAs are usually composed of five or more elements with equimolar or near equimolar elemental fractions, which form disordered solid-solution phases, specifically body-

centered-cubic (BCC) and/or face-centered-cubic (FCC) phases. Both single-phase and multi-phase HEAs are expected to exhibit superior corrosion resistance relative to conventional alloys. Most HEAs contain passivating elements, such as Al, Cr, Mo, *etc.*, which facilitate the formation of passive layers, similar to the case of stainless steels. Meanwhile, HEAs tend to be free of impurities or inclusions, which usually act as corrosion-initiation sites [71]. In particular, some HEAs, forming single-phase solid solutions with homogenous chemical compositions [120, 152], are also expected to yield good corrosion resistance, along with their combination of excellent microstructural stability and decent mechanical properties. Such unique properties of HEAs make them good candidates for practical corrosion-resistant applications. A number of investigations on the corrosion behavior of HEAs have been reported, which revealed equivalent or superior corrosion resistance of HEAs in various aqueous environments, as compared with conventional corrosion-resistant alloys, such as 304 stainless steel (SS) [33, 51, 72-85].

6.2. Development of a Single-phase FCC HEA

HEAs with a single-phase microstructure without precipitates and elemental segregation, especially an FCC structure, tend to have better corrosion resistance than multi-phase HEAs. Therefore, a computational alloy design technique was used to development of a single-phase FCC HEA. As shown in Figure 63, An $Al_{0.3}CoCrFeNi$ is a good start material since it has a single-phase FCC structure over temperature ranges. The reason to choose FCC structure is due to its excellent corrosion resistance. For example, the microstructure of 304 and 316 stainless steels are all austenite, which is an FCC structure. For another example, the corrosion-resistant Ni alloys, such as Hastelloy C-22 and C-2000, are all FCC structures.

A set of EBSD maps (Figure 64), including phase map and inverse pole figure map, show that the $Al_{0.3}CoCrFeNi$ has 100 % (in red color) FCC structure, also called A1. The grain size is

around 300 μm. The slow cooling rate during the casting process might bring the alloy large grain size. The EDS results (Table 13) from several different locations in the alloys shows that the experimental results are close to the nominal composition. Also, a back-scattered SEM image and EDS X-ray maps (Figure 65) confirm that the alloy has homogenized chemical composition and no elemental segregation. From room temperature to 1,500 ^{o}C, this alloy only shows one set of FCC peaks by the in-situ neutron diffraction (Figure 66). This is consistent with the microscopic results and computational alloy design. Therefore, the Al0.3CoCrFeNi is confirmed to be a single-phase material, and its FCC crystal structure has over all temperature ranges. Overall, the single-phase FCC microstructure was confirmed using SEM with EDS and EBSD imaging, and in-situ neutron diffraction.

6.3. Corrosion-Fatigue and Electrochemical Behavior of a Single-phase FCC HEA

The Stress - Number of Cycles to Failure curve (also called S-N curve) for Al0.3CoCrFeNi in air established the existence of a fatigue limit of ~ 180 MPa, as shown in Figure 67. When testing the alloy in the ocean water solution, only limited decrease in the air fatigue limit is observed (Figure 67). In this aqueous solution, the 10^7 fatigue strength of the Al0.3CoCrFeNi alloy is ~ 170 MPa. Concerning the experimental deviation, ocean water have nearly no detectable effect on the air fatigue limit of the Al0.3CoCrFeNi alloy at a frequency of 10 Hz. Additionally, to reveal the environmental-degradation mechanism, a longitudinal section (Figure 68) just beneath the fracture plane shows the intragranular fracture rather than inter-granular. Therefore, it is believed that this material is suffering more brittleness than it is suffering grain boundary attack or decohesion. The grains themselves seem more likely to crack than the grain boundaries. Also, the

EBSD phase map (Figure 68c) and EDS X-ray maps (Figure 69) shows that this alloy has no phase transformation and no segregation after the cyclic loading in the ocean water environment.

Results of the slow strain rate testing performed in air and in ocean water are given in Figure 70. Slow strain rate testing is a standard method of testing metals for evaluating the environmental effect on the stress-corrosion cracking susceptibility. Critical strain rates are different in alloys, and a strain rate of 2×10^{-6} / s is a median value according to Table 14, and was chosen to test the alloy. If suffering stress-corrosion cracking, the ductility of alloy should be largely reduced in the corrosive environment compared to the inert environment. As we can see in Figure 70, in the corrosive environment (ocean water), the ductility of this alloy is not reduced compared to the inert environment (air). The result proves that the Al0.3CoCrFeNi alloy is not susceptible to stress-corrosion cracking in ocean water environment.

Figure 71 shows the anodic polarization curves of the Al0.3CoCrFeNi alloy, 316L stainless steel, and C2000 nickel alloy in the ocean water solution at room temperature (25 ^{o}C). The corrosion potential (E_{corr}) of the Al0.3CoCrFeNi alloy (-177 mV) is more noble than that of C2000 nickel alloy (-189 mV) but less than that of 316L stainless steel (-117 mV). The corrosion current density (i_{corr}) of the Al0.3CoCrFeNi alloy (1.37×10^{-2} μA/cm^2) is also lower than that of C2000 nickel alloy (3.45×10^{-2} μA/cm^2), but higher than 316L stainless steel (4.50×10^{-3} μA/cm^2). In general, the i_{corr} values can be used to calculate the general corrosion rates (mmpy) of alloys. However, a lower corrosion current density does not necessarily correspond to a lower corrosion rate, because the corrosion rate is not only related to the corrosion current density but also to a function of atomic-fraction-weighted values of atomic weight, ion valence, and density of the alloy. Therefore, a more reasonable value of the corrosion rate can be estimated according to Faraday's law. Consequently, the general corrosion rate of the Al0.3CoCrFeNi alloy in ocean

water is 3.40 x 10^{-4} mmpy, whereas that of the C2000 nickel alloy is 1.17 x 10^{-4} mmpy, and that of the 316L stainless steel is 1.60 x 10^{-4} mmpy. The HEA had a comparable corrosion resistance in ocean water environment, compared to the other two corrosion-resistant alloys. This corrosion resistance of the Al0.3CoCrFeNi alloy may be attributed to the high-alloyed disordered solid solution, which made this alloy more stable in the corrosive environment.

Both the Al0.3CoCrFeNi alloy and C2000 nickel alloy showed the repassivation behavior, while this did not happen in the 316L stainless steel (Figure 72). For cyclic polarization behavior, particular attention is to be focused on two features. The first feature is the breakdown potential, E_{pit}. The second feature is the protect potential (E_{prot}) at which the hysteresis loop is completed on the reverse polarization scan. The more noble E_{pit}, the less susceptible the alloy is to the initiation of localized pitting attack. The more E_{prot}, the less likely that propagation of pits will occur over a range of potential below E_{pit}. The Al0.3CoCrFeNi alloy has lower E_{pit} and E_{prot} than the C2000 nickel alloy but higher than 316L stainless steel, which means that the alloy is not as good as the C2000 but better than 316L.

Note that Al0.3CoCrFeNi and C2000 nickel alloys have very similar electrochemical behavior. This trend might be attributed to their Cr ratios. All three alloys have a single-phase FCC microstructure but different Cr ratios (Table 15). For example, Al0.3CoCrFeNi and C2000 nickel alloys are all having 23 weight percent of Cr element, while 316L stainless steel only has 18 weight percent of Cr element. This trend might be the reason that the Al0.3CoCrFeNi and C-2000 nickel alloys with the same higher Cr ratio have very similar electrochemical behavior, having better corrosion resistant in ocean water environment than 316L stainless steel with lower Cr ratio.

6.4. Conclusions

The microstructure of the Al0.3CoCrFeNi is a single-phase material and FCC crystal structure over all the temperature range, which was confirmed using scanning electron microscopy with EDS and EBSD imaging, and in-situ neutron diffraction. Ocean water has nearly no detectable effect on the air fatigue limit of the Al0.3CoCrFeNi alloy at a frequency of 10 Hz. A longitudinal section just beneath the fracture plane shows the intragranular fracture rather than intergranular fracture. This alloy was also not susceptible stress corrosion cracking to the ocean water environment at a strain rate of 2×10^{-6}/s. Electrochemical properties, including anodic and cyclic polarizations of this new advanced structural material, were compared with conventional alloys, indicating that this alloy has a lower corrosion potential and current, lower corrosion rate, and larger passivation range, compared to 316L stainless steel, and comparable to C2000 nickel alloy.

Chapter 7. Summary

The work is to provide a fundamental understanding of fatigue, fracture, and environmentally-assisted behavior of HEAs. The research involves fatigue, fracture, and environmentally-assisted behavior. Three tasks are studied: (1) microstructures and fracture mechanisms of HEAs, (2) fatigue failure and life prediction of HEAs, and (3) fatigue and environmentally-assisted behavior of HEAs.

In the first task, the microstructural stability and fracture mechanisms of the AlCoCrFeNi alloys are studied and compared with thermodynamic calculations. We discuss how as-cast and homogenized phases can be identified, what phases are usually found in the as-cast and homogenized conditions, and what the thermodynamics and kinetics of phase transformations are in the AlCoCrFeNi HEA. Using SEM/EDS, EBSD, STEM and high-energy synchrotron X-ray diffraction, the microstructures of the AlCoCrFeNi-AC alloy are identified to have clear intra-granular dendritic structures containing two regions, NiAl-rich dendrites and NiAl-poor interdendritic regions. The TEM/STEM and the selective etching technique further confirm that both NiAl-rich and NiAl-poor regions have a fine A2+B2 nano-lamellar structure. Four phases, A2, B2, A1, and σ phases, are found in the AlCoCrFeNi-HP. The A2 nanoprecipitates embedded in the B2 matrix are also found in the homogenized condition, while blocky wall-like A1 phases along boundaries are identified and free of precipitates. A noticeable increase in the tensile ductility occurs after the HIP and homogenized treatment. During tensile testing at 700 ℃, the elongation of the homogenized alloy is 11.7 %, while the as-cast alloy show the elongation of only 1.0 %. The ultimate tensile strength at 700 ℃ is almost unaffected by the heat treatment, 400 MPa and 393 MPa, respectively. The reason for the limited elongation of the AlCoCrFeNi-AC alloy

may be that dislocation motion through these finely-spaced interfaces (50-100 nm) is very difficult, resulting in higher yield strength. The improvement of ductility for the AlCoCrFeNi-HP alloy may be due to breaking up the A2+B2 lamella into larger domains, the occurrence of the relatively ductile FCC phase, reduced casting defects, and relieved residual stress. The CALPHAD thermodynamic modeling, including the solidification path and the phase map, are well consistent with the experimental data.

In the second task, high-cycle fatigue-failure mechanisms of the cold-rolled Al0.5CoCrCuFeNi alloy are explored, and the experimental results are used to develop lifetime-prediction capabilities and safety models for future applications. The two-phase FCC Al0.5CoCrCuFeNi HEA shows a very promising mechanical property with a high yield strength (1,284 MPa), high fatigue strength (810 MPa), and significant ductility (7.6 %) (Table 12). The fatigue life decreases, as the applied maximum stress levels increases, as is normally observed. The high-cycle fatigue tests of the Condition-3 samples (fabricated by high-purity elements) gives higher fatigue strength than Condition-1, and less scatter than Conditions 1 and 2 (fabricated by commercial-purity elements). The attributed reasons are due to preexisting microcracks, pores, and oxides. The TEM observations suggest that nanotwinning is the main deformation mechanism before crack initiation and often during fatigue crack propagation. The main crack-initiation mechanism is: the severe cyclic stress action on the maximum-tensile-stress sites of specimens will induce more nanotwins and more sets of nanotwins before crack initiation. The increased density of nanotwins brings larger work hardening at the sites and gives higher resistance to crack initiation due to the smaller stress concentration by providing more twin boundaries. Nanotwins formation during fatigue test results in strengthening for this alloy, which gives greater endurance limits, and fatigue ratios comparable with steels and other conventional alloys. By employing a

random endurance-limit fatigue-life model to explore the effects of defects on the fatigue-endurance limits of HEAs, results suggest that using improved fabrication processes and/or high-purity raw materials enhance the fatigue behavior by reducing the preexisting microcracks in the test samples.

In the third task, the electrochemical-polarization behavior and fatigue-environmentally assisted behavior of Al0.3CoCrFeNi are investigated. The microstructure of the Al0.3CoCrFeNi is a single-phase material and FCC crystal structure over all the temperature range studied, which was confirmed using scanning electron microscopy with EDS and EBSD imaging, and in-situ neutron diffraction. Ocean water has nearly no detectable effect on the air fatigue limit of the Al0.3CoCrFeNi alloy at a frequency of 10 Hz. A longitudinal section just beneath the fracture plane shows the intragranular rather than intergranular fracture. This alloy was also not susceptible the stress-corrosion cracking in the ocean water environment at a strain rate of 2×10^{-6} / s. Electrochemical properties, including anodic and cyclic polarizations of this new advanced structural material, were compared with conventional alloys, indicating that this alloy has a lower corrosion potential and current, lower corrosion rate, and larger passivation range, compared to the 316L stainless steel, and comparable to C2000 nickel alloy.

Chapter 8. Suggested Future Work

Based on the current research and a number of publications focusing on the fracture, fatigue, and corrosion of the advanced engineering materials, HEAs, the several following uncertainties and future directions from the experimental perspective in this cutting-edge research area are suggested for researchers' consideration:

(1) On one hand, Al is the BCC phase stabilizer, and increasing the Al content will lead to the increased strength. On the other hand, a high Al molar ratio (e.g., 1.0 in the $Al_xCoCrFeNi$ HEA system) will cause the formation of the brittle B2 phase. Thus, an optimal Al ratio should be carefully studied for each HEA system to achieve optimized mechanical properties. Meanwhile, like conventional alloys, heat-treated HEAs certainly have different microstructures and mechanical properties than as-cast ones. An optimal heat-treatment process is one of the most influential factors to improve mechanical behavior.

(2) While the compression, hardness, and even corrosion behavior in an aqueous solution have been reported for these Al-containing HEAs, other mechanical properties, such as creep and fatigue [7], are needed in order to study whether these HEAs meet the requirements for gas turbines that require the structure stability and mechanical sustainability for substantially long hours at high temperatures. The formation of protective surface oxide scales is extremely important for high-temperature applications and for any structural materials. In this regard, the critical amounts of Al and Cr required to form a continuous and coherent Cr_2O_3 or Al_2O_3 surface scale need to be studied.

(3) Residual stresses from cold working, hot forging, and other sources can lead to higher corrosion rates, causing stress corrosion cracking (SCC) [153]. However, cold working and hot forging, such as upset forging, tend to effectively remove casting defects, refine microstructures, improve the strengths, and accelerate the homogenization process of as-cast alloys [28]. The effects of residual stresses on corrosion behavior of HEAs can be further investigated.

(4) Welding has a number of effects on the metallurgy and corrosion resistance of alloys, because the uncontrolled melting and re-solidification will lead to grain size and chemical composition changes. The corrosion behavior of this region, known as the heat-affected zone (HAZ), can be an interesting topic to be studied.

Chapter 9. Intellectual Merit and Broader Impacts

The objective of the work is to provide fundamental understanding of fatigue fracture and environmentally assisted behavior of HEAs. The present research involves fatigue, fracture, and environmentally assisted behavior of a new kind of advanced engineering materials, called HEAs. Three tasks have been studied. In the first task, microstructural stability and fracture mechanisms of the ac-cast and homogenized AlCoCrFeNi alloys were studied and compared with thermodynamic calculations. In the second task, the high-cycle four-point-bending fatigue behavior and failure mechanisms of the cold-rolled $Al_{0.5}$CoCrCuFeNi alloy were explored, and the experimental results were used to develop lifetime-prediction capabilities and safety models for future applications. In the third task, the electrochemical-polarization and fatigue-environmentally assisted behavior and long-term heat-treatment effects of the HIPed $Al_{0.3}$CoCrFeNi HEA system were investigated and predicted with lifetime modeling.

The author hopes that the study of fatigue fracture on HEAs advances the fundamental understanding of the mechanisms of the fatigue-fracture and environmentally-assisted behavior of HEAs. The experimental approaches also provide the critical information for the mechanistic study of the heat-treatment effects on microstructures and mechanical properties, especially corrosion fatigue of HEA systems. The current research on the fatigue-fracture and environmentally-assisted behavior of HEAs enriches the research and teaching efforts in advanced structural materials at UT. The presentations at professional conferences and the publications in academic journals achieve the wide national and international impact. The author develops a comprehensive knowledge of advanced materials processes and characterizations.

References

[1] Lu K. Science 2010;328:319.

[2] Cantor B, Chang ITH, Knight P, Vincent AJB. Mater. Sci. Eng. A 2004;375:213.

[3] Yeh JW, Chen SK, Lin SJ, Gan JY, Chin TS, Shun TT, Tsau CH, Chang SY. Adv. Eng. Mater. 2004;6:299.

[4] Zhou YJ, Zhang Y, Wang YL, Chen GL. Appl. Phys. Lett. 2007;90:181904.

[5] Senkov ON, Wilks GB, Miracle DB, Chuang CP, Liaw PK. Intermetallics 2010;18:1758.

[6] Zhang Y, Yang X, Liaw PK. Jom 2012;64:830.

[7] Hemphill MA, Yuan T, Wang GY, Yeh JW, Tsai CW, Chuang A, Liaw PK. Acta Mater. 2012;60:5723.

[8] Otto F, Yang Y, Bei H, George EP. Acta Mater. 2013;61:2628.

[9] Senkov ON, Senkova SV, Woodward C, Miracle DB. Acta Mater. 2013;61:1545.

[10] Zhu C, Lu ZP, Nieh TG. Acta Mater. 2013;61:2993.

[11] Zhang Y, Zuo T, Cheng Y, Liaw PK. Sci. Rep. 2013;3:1455.

[12] Senkov ON, Senkova SV, Miracle DB, Woodward C. Mater. Sci. Eng. A 2013;565:51.

[13] Guo W, Dmowski W, Noh J-Y, Rack P, Liaw P, Egami T. Metall. Mater. Trans. A 2013;44:1994.

[14] Tang Z, Gao MC, Diao HY, Yang TF, Liu JP, Zuo TT, Zhang Y, Lu ZP, Cheng YQ, Zhang YW, Dahmen KA, Liaw PK, Egami T. Jom 2013;65:1848.

[15] Komarasamy M, Kumar N, Tang Z, Mishra RS, Liaw PK. Mater. Res. Lett. 2014:DOI: 10.1080/21663831.2014.958586.

[16] Antonaglia J, Xie X, Tang Z, Tsai CW, Qiao JW, Zhang Y, Laktionova MO, Tabachnikova ED, Yeh JW, Senkov ON, Gao MC, Uhl JT, Liaw PK, Dahmen KA. Jom 2014;66:2002.

[17] Zhang Y, Lu ZP, Ma SG, Liaw PK, Tang Z, Cheng YQ, Gao MC. MRS Communications 2014;4:57.

[18] Huang PK, Yeh JW, Shun TT, Chen SK. Adv. Eng. Mater. 2004;6:74.

[19] Senkov ON, Scott JM, Senkova SV, Miracle DB, Woodward CF. J. Alloys Compd. 2011;509:6043.

[20] Zhao W, Sun Z, Tang Z, Liaw PK, Li J, Liu RP, Li G. Metall. Mater. Trans. A 2013;45:2371.

[21] Senkov ON, Wilks GB, Scott JM, Miracle DB. Intermetallics 2011;19:698.

[22] Ashby MF. Materials selection in mechanical design. Burlington, MA: Butterworth-Heinemann, 2011.

[23] Hofmann DC, Suh J-Y, Wiest A, Duan G, Lind M-L, Demetriou MD, Johnson WL. Nature 2008;451:1085.

[24] Wang WH. Prog. Mater. Sci. 2012;57:487.

[25] Wang FJ, Zhang Y, Chen GL. J. Alloys Compd. 2009;478:321.

[26] Senkov ON, Scott JN, Senkova SV, Meisenkothen F, Miracle DB, Woodward CF. J. Mater. Sci. 2012;47:4062.

[27] Zhang Y, Zuo TT, Tang Z, Gao MC, Dahmen KA, Liaw PK, Lu ZP. Prog. Mater Sci. 2014;61:1.

[28] Miracle DB, Miller JD, Senkov ON, Woodward C, Uchic MD, Tiley J. Entropy 2014;16:494.

[29] Gao MC, Alman DE. Entropy 2013;15:4504.

[30] Takeuchi A, Amiya K, Wada T, Yubuta K, Zhang W. Jom 2014:1.

[31] Feuerbacher M, Heidelmann M, Thomas C. Materials Research Letters 2014:1. DOI:10.1080/21663831.2014.951493.

[32] Kao Y-F, Chen T-J, Chen S-K, Yeh J-W. J. Alloys Compd. 2009;488:57.

[33] Lin C-M, Tsai H-L, Bor H-Y. Intermetallics 2010;18:1244.

[34] Tsai CW, Chen YL, Tsai MH, Yeh JW, Shun TT, Chen SK. J. Alloys Compd. 2009;486:427.

[35] Kuznetsov AV, Shaysultanov DG, Stepanov ND, Salishchev GA, Senkov ON. Mater. Sci. Eng. A 2012;533:107.

[36] Chou HP, Chang YS, Chen SK, Yeh JW. Mater. Sci. Eng., B 2009;163:184.

[37] Ng C, Guo S, Luan J, Shi S, Liu CT. Intermetallics 2012;31:165.

[38] Hsieh K-C, Yu C-F, Hsieh W-T, Chiang W-R, Ku JS, Lai J-H, Tu C-P, Yang CC. J. Alloys Compd. 2009;483:209.

[39] Tsai CW, Tsai MH, Yeh JW, Yang CC. J. Alloys Compd. 2010;490:160.

[40] Wang W-R, Wang W-L, Wang S-C, Tsai Y-C, Lai C-H, Yeh J-W. Intermetallics 2012;26:44.

[41] Wang YP, Li BS, Ren MX, Yang C, Fu HZ. Mater. Sci. Eng. A 2008;491:154.

[42] Cui HB, Wang Y, Wang JY, Guo XF, Fu HZ. China Foundry 2011;8:259.

[43] Zhu JM, Fu HM, Zhang HF, Wang AM, Li H, Hu ZQ. J. Alloys Compd. 2011;509:3476.

[44] Ma SG, Zhang Y. Mater. Sci. Eng. A 2012;532:480.

[45] Wang FJ, Zhang Y, Chen GL, Davies HA. J. Eng. Mater. Technol. 2009;131.

[46] Zhu JM, Fu HM, Zhang HF, Wang AM, Li H, Hu ZQ. Mater. Sci. Eng., A 2010;527:6975.

[47] Li C, Zhao M, Li JC, Jiang Q. J. Appl. Phys. 2008;104:113504.

[48] Li C, Li JC, Zhao M, Jiang Q. J. Alloys Compd. 2010;504, Supplement 1:S515.

[49] Zhang Y. Mater. Sci. Forum 2010;654-656:1058.

[50] Kao Y-F, Chen S-K, Chen T-J, Chu P-C, Yeh J-W, Lin S-J. J. Alloys Compd. 2011;509:1607.

[51] Kao Y-F, Lee T-D, Chen S-K, Chang Y-S. Corros. Sci. 2010;52:1026.

[52] Kaufman L, Bernstein H. Computer calculation of phase diagrams with special reference to refractory metals. New York: Academic Press, 1970.

[53] Joubert JM. Prog. Mater. Sci. 2008;53:528.

[54] Cao HB, Pan Y, Ding L, Zhang C, Zhu J, Hsieh KC, Chang YA. Acta Mater. 2008;56:2032.

[55] Bei H, Yang Y, Viswanathan GB, Rawn CJ, George EP, Tiley J, Chang YA. Acta Mater. 2010;58:6027.

[56] Yang Y, Zhang C, Chen S, Morgan D, Chang YA. Intermetallics 2010;18:574.

[57] Zhang C, Zhang F, Chen S, Cao W. Jom 2012;64:839.

[58] Senkov ON, Woodward CF. Mater. Sci. Eng. A 2011;529:311.

[59] Tong C-J, Chen M-R, Yeh J-W, Lin S-J, Chen S-K, Shun T-T, Chang S-Y. Metall. Mater. Trans. A 2005;36:1263.

[60] Shun TT, Du YC. J. Alloys Compd. 2009;479:157.

[61] Wang XF, Zhang Y, Qiao Y, Chen GL. Intermetallics 2007;15:357.

[62] Zhou YJ, Zhang Y, Kim TN, Chen GL. Mater. Lett. 2008;62:2673.

[63] Qiao JW, Ma SG, Huang EW, Chuang CP, Liaw PK, Zhang Y. Mater. Sci. Forum 2011;688:419.

[64] Laktionova MO, Tabachnikova ED, Tang Z, Liaw PK. Low Temperature Mechanical Behavior of the Al0.5CoCrCuFeNi High-Entropy Alloy. Materials Science and Technology. Pittsburgh, Pennsylvania, USA, 2012.

[65] Nelson WB. Accelerated testing: statistical models, test plans, and data analysis: Wiley, 1990.

[66] Pascual FG, Meeker WQ. Technometrics 1999;41:277.

[67] Wallin K. Fatigue Fract. Eng. Mater. Struct. 2010;33:333.

[68] Koch GH, Brongers MP, Thompson NG, Virmani YP, Payer JH. Corrosion cost and preventive strategies in the United States. No. FHWA-RD-01-156, 2002.

[69] G2MT Labs, LLC. G2MT Labs, LLC. http://www.g2mtlabs.com/cost-of-corrosion/.

[70] Corrosion 13A, ASM Handb., ASM Int. 2003.

[71] Frankel GS. Corrosion 13A, ASM Handb., ASM Int. 2003:257.

[72] Chen YY, Duval T, Hung UD, Yeh JW, Shih HC. Corros. Sci. 2005;47:2257.

[73] Chen YY, Hong UT, Shih HC, Yeh JW, Duval T. Corros. Sci. 2005;47:2679.

[74] Chen YY, Hong UT, Yeh JW, Shih HC. Scripta Mater. 2006;54:1997.

[75] Chou YL, Yeh JW, Shih HC. Corros. Sci. 2010;52:2571.

[76] Doğan Ö, Nielsen B, Hawk J. Oxid. Met. 2013;80:177.

[77] Hsu Y-J, Chiang W-C, Wu J-K. Mater. Chem. Phys. 2005;92:112.

[78] Lee CP, Chang CC, Chen YY, Yeh JW, Shih HC. Corros. Sci. 2008;50:2053.

[79] Lee CP, Chen YY, Hsu CY, Yeh JW, Shih HC. J. Electrochem. Soc. 2007;154:C424.

[80] Lee CP, Chen YY, Hsu CY, Yeh JW, Shih HC. Thin Solid Films 2008;517:1301.

[81] Li QH, Yue TM, Guo ZN, Lin X. Metall. Mater. Trans. A 2012;44:1767.

[82] Lin C-M, Tsai H-L. Intermetallics 2011;19:288.

[83] Lin C-M, Tsai H-L. Mater. Chem. Phys. 2011;128:50.

[84] Qiu X-W, Liu C-G. J. Alloys Compd. 2013;553:216.

[85] Qiu X-W, Zhang Y-P, He L, Liu C-g. J. Alloys Compd. 2013;549:195.

[86] Noel JJ. Corrosion 13A, ASM Handb., ASM Int. 2003;13A:258.

[87] Chuang M-H, Tsai M-H, Wang W-R, Lin S-J, Yeh J-W. Acta Mater. 2011;59:6308.

[88] Hsu CY, Sheu TS, Yeh JW, Chen SK. Wear 2010;268:653.

[89] Wu JM, Lin SJ, Yeh JW, Chen SK, Huang YS. Wear 2006;261:513.

[90] Tian F, Delczeg L, Chen N, Varga LK, Shen J, Vitos L. Physical Review B 2013;88:085128.

[91] Welk BA, Williams REA, Viswanathan GB, Gibson MA, Liaw PK, Fraser HL. Ultramicroscopy 2013;134:193.

[92] Guo S, Ng C, Liu CT. J. Alloys Compd. 2013;557:77.

[93] Smith WF. Structure and properties of engineering alloys. New York: McGraw-Hill, 1993.

[94] Chiang W-C, Luu W-C, Wu J-K. J. Mater. Sci. 2006;41:3041.

[95] Tong C-J, Chen Y-L, Yeh J-W, Lin S-J, Chen S-K, Shun T-T, Tsau C-H, Chang S-Y. Metall. Mater. Trans. A 2005;36:881.

[96] Laktionova MA, Tabchnikova ED, Tang Z, Liaw PK. Low Temp. Phys. 2013;39:630.

[97] Rebak RB. Corrosion 13A, ASM Handb., ASM Int. 2003:279.

[98] ASTM G31 REV A. West Conshohocken, PA: ASTM International, 2012.

[99] ASTM G102-89. West Conshohocken, PA: ASTM International, 2010.

[100] Haynes WM, Lide DR. CRC handbook of chemistry and physics. Boca Raton, Fla.: CRC Press, 2010.

[101] Gangloff RP. Metall. Trans. A 1985;16:953.

[102] ASTM E8. Standard Test Methods for Tension Testing of Metallic Materials. West Conshohocken, PA: ASTM International, 2012.

[103] ASTM. Conducting Constant Amplitude Axial Fatigue Tests of Metallic Materials. ASTM E466 - 07. Philadelphia, PA, 2007.

[104] Tian F, Delczeg L, Chen N, Varga LK, Shen J, Vitos L. Phys. Rev. B 2013;88:085128.

[105] Tang Z, Huang L, He W, Liaw P. Entropy 2014;16:895.

[106] Singh S, Wanderka N, Murty BS, Glatzel U, Banhart J. Acta Mater. 2011;59:182.

[107] Wang W-R, Wang W-L, Yeh J-W. J. Alloys Compd. 2014;589:143.

[108] Widom M, Huhn WP, Maiti S, Steurer W. Metall. Mat. Trans. A 2014;45:196.

[109] Chou K-C, Austin Chang Y. Berichte der Bunsengesellschaft für physikalische Chemie 1989;93:735.

[110] Zhang C, Zhang F, Chen S-L, Cao W-S, Chang Y. Acta Mater. 2011;59:6246.

[111] Zhang C, Gao M, Yang Y, Zhang F. Calphad 2014;45:178.

[112] Scheil E. Z. Metallkd 1942;34:70.

[113] Tsai M-H, Yuan H, Cheng G, Xu W, Tsai K-Y, Tsai C-W, Jian WW, Juan C-C, Shen W-J, Chuang M-H, Yeh J-W, Zhu YT. Intermetallics 2013;32:329.

[114] Bergman G, Shoemaker DP. Acta Crystallogr. 1954;7:857.

[115] Liu CT, Schneibel JH, Maziasz PJ, Wright JL, Easton DS. Intermetallics 1996;4:429.

[116] Liu Z, Guo S, Liu X, Ye J, Yang Y, Wang X-L, Yang L, An K, Liu CT. Scripta Materialia 2011;64:868.

[117] Ishida K, Nishizawa T. J. Phase Equilib. 1990;11:357.

[118] ASM International. Alloy Phase Diagram Committee., ASM International. Handbook Committee. ASM handbook. Materials Park, Ohio: ASM International, 1992.

[119] He JY, Liu WH, Wang H, Wu Y, Liu XJ, Nieh TG, Lu ZP. 10.1016/j.actamat.2013.09.037. Acta Mater 2013.

[120] Lucas MS, Wilks GB, Mauger L, Munoz JA, Senkov ON, Michel E, Horwath J, Semiatin SL, Stone MB, Abernathy DL, Karapetrova E. Appl. Phys. Lett. 2012;100:251907.

[121] Otto F, Dlouhý A, Somsen C, Bei H, Eggeler G, George EP. Acta Mater. 2013;61:5743.

[122] Wu Z, Bei H, Otto F, Pharr GM, George EP. Intermetallics 2014;46:131.

[123] Senkov ON, Senkova SV, Woodward C. Acta Mater. 2014;68:214.

[124] Bei H, Shim S, George E, Miller M, Herbert E, Pharr G. Scripta Mater. 2007;57:397.

[125] Bei H, Shim S, Pharr GM, George EP. Acta Mater. 2008;56:4762.

[126] Hou JS, Zhou LZ, Yuan C, Tang Z, Guo JT, Qin XZ, Liaw PK. Mater. Sci. Eng. A 2013;560:25.

[127] Vander Voort GF. Metallography, principles and practice. New York: New York : McGraw-Hill, 1984.

[128] Tang Z. Master Thesis. The University of Tennessee, TN, USA 2012.

[129] Nelson WB. Accelerated testing: statistical models, test plans, and data analysis: John Wiley & Sons, 2009.

[130] Huang L, Wang G, Qiao D, Liaw PK, Pang S, Wang J, Zhang T. J. Alloys Compd. 2010;504, Supplement 1:S159.

[131] Jiang L, Brooks CR, Liaw PK, Wang H, Rawn CJ, Klarstrom DL. MSEA 2001;314:162.

[132] Jiang L, Wang H, Liaw PK, Brooks CR, Klarstrom DL. Metall. Mater. Trans. A 2001;32:2279.

[133] Sun P-L, Wang G, Liaw PK. Scripta Mater. 2012;66:443.

[134] Tian H, Liaw PK, Fielden DE, Brooks CR, Brotherton MD, Jiang L, Yang B, Wang H, Strizak JP, Mansur LK. Metall. Mater. Trans. A 2006;37:163.

[135] Wang GY, Liaw PK, Yokoyama Y, Inoue A. J. Appl. Phys. 2011;110:113507.

[136] Wang GY, Liaw PK, Yokoyama Y, Inoue A. Intermetallics 2012;23:96.

[137] Hertzberg RW. Deformation and fracture mechanics of engineering materials. New York: J. Wiley & Sons, 1996.

[138] Kvam PH, Kvam EP. Technometrics 1999;41:292.

[139] Meeker WQ, Escobar LA. Statistical methods for reliability data: John Wiley & Sons, 1998.

[140] Ebeling CE. An introduction to reliability and maintainability engineering 2005.

[141] Ravichandran KS, Vasudevan AK. Fatigue And Fracture, Vol. 19, ASM Handb., ASM Int. 1996:381.

[142] Bouaziz O, Allain S, Scott C. Scripta Mater. 2008;58:484.

[143] Karaman I, Sehitoglu H, Chumlyakov YI, Maier HJ. Jom 2002;54:31.

[144] Zaddach AJ, Niu C, Koch CC, Irving DL. Jom 2013;65:1780.

[145] Zhang H, He Y-Z, Pan Y, Guo S. J. Alloys Compd. 2014;600:210.

[146] Brooks CR, Choudhury A. Metallurgical failure analysis. New York: McGraw-Hill, 1993.

[147] Brooks CR, Choudhury A. Failure analysis of engineering materials. New York: McGraw-Hill, 2002.

[148] Morrison ML, Buchanan RA, Liaw PK, Green BA, Wang GY, Liu CT, Horton JA. MSEA 2007;467:190.

[149] Zhang Y, Zhou YJ, Lin JP, Chen GL, Liaw PK. Adv. Eng. Mater. 2008;10:534.

[150] Ma SG, Zhang SF, Gao MC, Liaw PK, Zhang Y. Jom 2013;65:1751.

[151] He JY, Liu WH, Wang H, Wu Y, Liu XJ, Nieh TG, Lu ZP. Acta Mater. 2014;62:105.

[152] Yao MJ, Pradeep KG, Tasan CC, Raabe D. Scripta Mater. 2014;72–73:5.

[153] Natishan P. Corrosion 13A, ASM Handb., ASM Int. 2003:687.

[154] Al-Fozan SA, Malik AU. Desalination 2008;228:61.

[155] Ezuber H, El-Houd A, El-Shawesh F. Mater. Des. 2008;29:801.

[156] Miller MK, Liaw PK. Bulk metallic glasses: an overview. New York: Springer, 2008.

[157] Corrosion 13B, ASM Handb., ASM Int. 2003.

[158] Quartarone G, Bellomi T, Zingales A. Corros. Sci. 2003;45:715.

[159] Chen J, Young B. Eng. Struc. 2006;28:229.

[160] Venkatesh V, Rack HJ. Mech. Mater. 1998;30:69.

[161] Schaeublin R, Leguey T, Spatig P, Baluc N, Victoria M. J. Nucl. Mater. 2002;307:778.

[162] Sundar RS, Deevi SC. Mater. Sci. Eng. A 2003;357:124.

[163] Li JC, Wu TY, Riquier Y. Mater. Sci. Eng. A 1994;174:149.

[164] Liu CT. Mater. Chem. Phys. 1995;42:77.

[165] Sikka VK, Deevi SC, Viswanathan S, Swindeman RW, Santella ML. Intermetallics 2000;8:1329.

[166] Noh S, Kasada R, Kimura A. Acta Mater. 2011;59:3196.

[167] Hirata A, Fujita T, Wen YR, Schneibel JH, Liu CT, Chen MW. Nat. Mater. 2011;10:922.

Appendix

Table 1. Corrosion potential, E_{corr}, corrosion current density ($\mu A/cm^2$), i_{corr}, pitting potential, E_{pit}, and average corrosion rates (mm/year) of HEAs and other materials in the 3.5 wt.% NaCl solution at room temperature [33, 77, 82, 154-157].

Composition	**Heat Treatment Condition**	E_{corr} (V_{SHE})	i_{corr} ($\mu A/cm^2$)	E_{pit} (V_{SHE})	**Corrosion Rates* (mm/year)**
CoCrFeNi	As-cast	-0.01	0.03	0.55	3.3×10^{-4}
$CoCrCu_{0.5}FeNi$	As-cast	-0.04	0.72	0.34	7.5×10^{-4}
$CoCrCu_{0.5}FeNi$	1,100ºC/24h	-0.15	0.14	0.30	1.1×10^{-3}
$CoCrCu_{0.5}FeNi$	1,250ºC/24h	-0.02	0.01	0.29	4.0×10^{-5}
$CoCrCu_{0.5}FeNi$	1,350ºC/24h	-0.16	0.05	0.30	3.6×10^{-4}
$Al_{0.5}CoCrFeNi$	As-cast	-0.32	0.17	0.38	1.3×10^{-3}
$Al_{0.5}CoCrFeNi$	800ºC/24h	-0.39	0.30	0.39	2.4×10^{-3}
$Al_{0.5}CoCrFeNi$	950ºC/24h	-0.29	2.22	0.43	1.8×10^{-2}
Stainless steels	-	0.02*	0.06*	0.72*	$5.3 \times 10^{-4} – 3.4 \times 10^{-3}$
Low alloy steels	-	-	-	-	$6.9 \times 10^{-2} – 1.5 \times 10^{-1}$
Low carbon steels	-	-	-	-	$9.7 \times 10^{-2} – 8.1 \times 10^{-1}$
Nickel alloys	-	-	-	-	$3.1 \times 10^{-5} – 1.4 \times 10^{-4}$
Aluminum alloys	-	-	-	-	$8.9 \times 10^{-4} – 2.9 \times 10^{-3}$
Titanium alloys	-	-	-	-	$8.0 \times 10^{-6} – 2.5 \times 10^{-4}$
Bulk metallic glasses	-	-	-	-	$1.0 \times 10^{-3} – 2.9 \times 10^{-1}$

* Average corrosion rates are obtained, including the electrochemical measurements and weight-loss method. Specifically, the corrosion data refer to the 304L stainless steel.

Table 2. Corrosion potential, E_{corr}, corrosion current density (μA/cm^2), i_{corr}, pitting potential, E_{pit}, passive region, ΔE, and average corrosion rates (mm/year) of HEAs and conventional alloys in the 0.5 M H_2SO_4 solution at room temperature [51, 78, 157, 158].

Composition	E_{corr} **(mV$_{SHE}$)**	i_{corr} **(μA/cm^2)**	ΔE **(mV$_{SHE}$)**	**Corrosion Rates * (mm/year)**
CoCrFeNi	-81	15.8	1,098	0.12
$Al_{0.25}$CoCrFeNi	-95	16.7	1,092	0.13
$Al_{0.5}$CoCrFeNi	-84	13.4	1,083	0.11
$CrFe_{1.5}MnNi_{0.5}$	-229	686	1,227	6.9
$Al_{0.3}CrFe_{1.5}MnNi_{0.5}$	-194	2,390	1,176	24
Stainless steels	-186	74.5	1,178	0.47 – 9.3
Copper alloys	-	-	-	0.06 – 0.30
Nickel alloys	-	-	-	0.03 – 0.10

* Average corrosion rates are obtained, including electrochemical measurements and weight loss method.

Table 3. Chemical compositions (at. %) of AlCoCrFeNi in the as-cast condition by inductively-coupled plasma-optical emission spectrometers (ICP-OES). The experimental (exp.) results are compared with calculated (cal.) ones.

Element	**Al**	**Co**	**Cr**	**Fe**	**Ni**	**C**	**H**	**O**	**N**
Exp. (at. %)	20.25	20.39	19.31	19.68	20.37	0.002	1 ppm	0.004	0.002
Cal. (at. %)	20.00	20.00	20.0	20.00	20.00	-	-	-	-

Table 4. Chemical compositions (at. %) of NiAl-rich dendrites (DR) and NiAl-poor interdendrites (ID) in the as-cast condition, by SEM-EDS (more than 3 different locations and less than 2 at. % standard deviation).

AlCoCrFeNi-AC					
Element / Region	**Al**	**Co**	**Cr**	**Fe**	**Ni**
NiAl-rich DR	26	21	14	16	22
NiAl-poor ID	18	19	22	21	19

Table 5. Chemical compositions (at. %) of each phase in AlCoCrFeNi-AC (A2+B2+A1) by STEM-EDS (semi-quantitative analyses) and AlCoCrFeNi-HP (A2+B2+A1+σ) by SEM-EDS (more than 3 different locations and less than 2 at. % standard deviation).

AlCoCrFeNi-AC					
Element / Phase	**Al**	**Co**	**Cr**	**Fe**	**Ni**
A2 *	trace	20	~ 50	25	5
B2 *	~ 40	15	trace	10	30
A1 **	-	-	-	-	-
AlCoCrFeNi-HP					
Element / Phase	**Al**	**Co**	**Cr**	**Fe**	**Ni**
A2	3	19	43	30	6
B2	30	19	9	14	27
A1	8	23	27	27	15
σ	5	24	28	31	11

* Semiquantitative analyses from STEM-EDS spectra

** The A1 phase is not of a full-foil-thickness, so that STEM-EDS spectra quantification is not reliable.

Table 6. Volume fraction of each phase in as-cast (A2+B2+A1) and homogenized (A2+B2+A1+σ) conditions by the EBSD analysis.

AlCoCrFeNi-AC		
Phase		**Volume fraction**
NiAl-rich DR	**A2**	29 %
	B2	71 %
	Total	100 %
NiAl-poor ID	**A2**	58 %
	B2	40 %
	A1	2 %
	Total	100 %
Overall	**A2**	46 %
	B2	53 %
	A1	1 %
	Total	100 %

AlCoCrFeNi-HP		
Phase	**Experiment**	**Modeling**
A2	24 %	13 %
B2	46 %	38 %
A1	16 %	49 %
σ	14 %	-
Total	100 %	100 %

Table 7. Tensile properties at 700 ℃ for AlCoCrFeNi-AC, AlCoCrFeNi-HP, and some other high-temperature structural materials (all of these data were tested in tension at 700 °C): elongation to fracture (ε), yield strength (σ_y), ultimate tensile strength (σ_{UTS}), and specific strength (σ_{UTS}/ρ). Densities of all materials are also listed. Note that density (**ρ**) values of the present work (AlCoCrFeNi-AC and AlCoCrFeNi-HP) were measured with a helium pycnometer, while density values of other HEAs are calculated by the theoretical density of a disordered solid solution [5].

Materials	**ε (%)**	**σ_y (MPa)**	**σ_{UTS} (*MPa*)**	**σ_{UTS}/ρ [*MPa/(g/cm^3)*]**	**ρ *(g/cm^3)***
AlCoCrFeNi-AC (This Work)	**1.0**	**395**	**400**	**57.1**	**7.0**
AlCoCrFeNi-HP (This Work)	**11.7**	**295**	**393**	**56.1**	**7.0**
AlCoCrCuFeNi As-Cast [35]	4.7	350	360	50.7	7.1
AlCoCrCuFeNi Forged [35]	63	63	91	12.8	7.1
$Al_{0.5}$CoCrCuFeNi As-Rolled [39]	5.0	180	185	24.3	7.6
$Al_{0.5}$CoCrCuFeNi As-Annealed [39]	12	160	180	23.7	7.6
Duplex Stainless Steel [159]	2.4	329	366	46.9	7.8
304 Stainless Steel [159]	9.1	179	248	31.8	7.8
Ni-Based Inconel 690 [160]	26	150	478	53.7	8.9
ODS Steel 0.3 % Yttria [161]	11	210	272	34.9	7.8
Intermetallics FeAl 787 [162]	18	345	350	64.8	5.4

Table 8. Summary of three conditions of cold-rolled $Al_{0.5}CoCrCuFeNi$.

Condition	**Raw materials**	**Processing**	**Machining**
1*	Commercial purity: > 99 %	Homogenized at 1,000 ^{o}C for 6 h, water quenched and then cold rolled.	Shrinkage pores and macrosegregation were **remained** in some portions.
2	Commercial purity: > 99 %	Homogenized at 1,000 ^{o}C for 6 h, water quenched and then cold rolled.	Shrinkage pores and macrosegregation were **removed** before cold rolling.
3	High purity: > 99.9 %	Homogenized at 1,000 ^{o}C for 6 h, water quenched and then cold rolled.	Shrinkage pores and macrosegregation were **removed** before cold rolling.

* used in the literature [7]

Table 9. TEM-EDS results of matrix (FCC-1) and Cu-rich second phase (FCC-2) are shown below. The EDS result of FCC-1 is an average of four different locations, while the one of FCC-2 is an average of ten different locations of nanostructure.

Elements / Phases	Al	Co	Cr	Cu	Fe	Ni
Matrix (FCC-1)	6.4 ±0.5	17.2 ±1.1	16.9 ±1.2	27.1 ±2.2	17.0 ±0.3	15.6 ±0.3
Second (FCC-2)	11.6 ±1.7	4.2 ±1.1	1.7 ±1.0	65.0 ±3.6	3.7 ±1.2	13.8 ±1.9

Table 10. Maximum likelihood estimates of model parameters.

Parameter	**Maximum likelihood estimate**		
	Condition-1	**Condition-2**	**Condition-3**
$\boldsymbol{\beta_0}$	- 2.996	- 4.712	- 3.212
$\boldsymbol{\beta_1}$	- 1.111	- 1.590	- 0.643
$\boldsymbol{\sigma}$	1.034	0.006	0.216
$\boldsymbol{\mu_\gamma}$	- 0.377	- 0.211	- 0.235
$\boldsymbol{\sigma_\gamma}$	0.373	0.170	0.053

Table 11. Characteristics of the endurance-limit distribution (Unit: MPa).

	Median	**Standard deviation**
Condition-1	685.9	342.9
Condition-2	810.1	156.4
Condition-3	790.7	46.8

Table 12. Microstructures and mechanical properties of the wrought $Al_{0.5}CoCrCuFeNi$ two-phase HEA.

Material	**Microstructure**	**Yield Strength**	**Ultimate Tensile Strength**	**Tensile Elongation**	**Fatigue Strength**	**Fatigue ratio**
$Al_{0.5}CoCrCuFeNi$	FCC-1 and FCC-2	1,284 MPa	1,344 MPa	7.6 %	810 MPa	0.60

Table 13. Experimental (Exp.) results by EDS and nominal (Nom.) results of Al0.3CoCrFeNi

Element	Exp. (at. %)	Nom. (at. %)
Al	7.00 ± 0.27	6.97
Co	23.46 ± 0.29	23.26
Cr	23.51 ± 0.80	23.26
Fe	22.74 ± 0.77	23.26
Ni	23.29 ± 0.76	23.26

Table 14. Critical strain rates of different alloys

Metal-environment system	**Critical strain rate, s^{-1}**
Aluminum alloys - aqueous chloride solutions	10^{-4} to 10^{-7}
Copper alloys - ammonia/nitrite solutions	10^{-6}
Titanium alloys - chloride solutions	10^{-5}
Steels - solutions of carbonates, hydroxides	10^{-6}
Magnesium alloys - chromate/chloride solutions	10^{-5}
Stainless steel - chloride solutions	10^{-6}
Stainless steel - high temperature water solutions	10^{-7}

Table 15. The chemical compositions and microstructures of the Al0.3CoCrFeNi alloy, 316L stainless steel, and C2000 nickel alloy

Material	**Composition (wt.%)**	**Microstructure**
$Al_{0.3}$CoCrFeNi	Ni-26Co-24Fe-**23Cr**-1Al	Single-Phase FCC
SS316L	Fe-**18Cr**-10Ni-3Mo	Single-Phase FCC
C-2000	Ni-**23Cr**-16Mo-2Cu	Single-Phase FCC

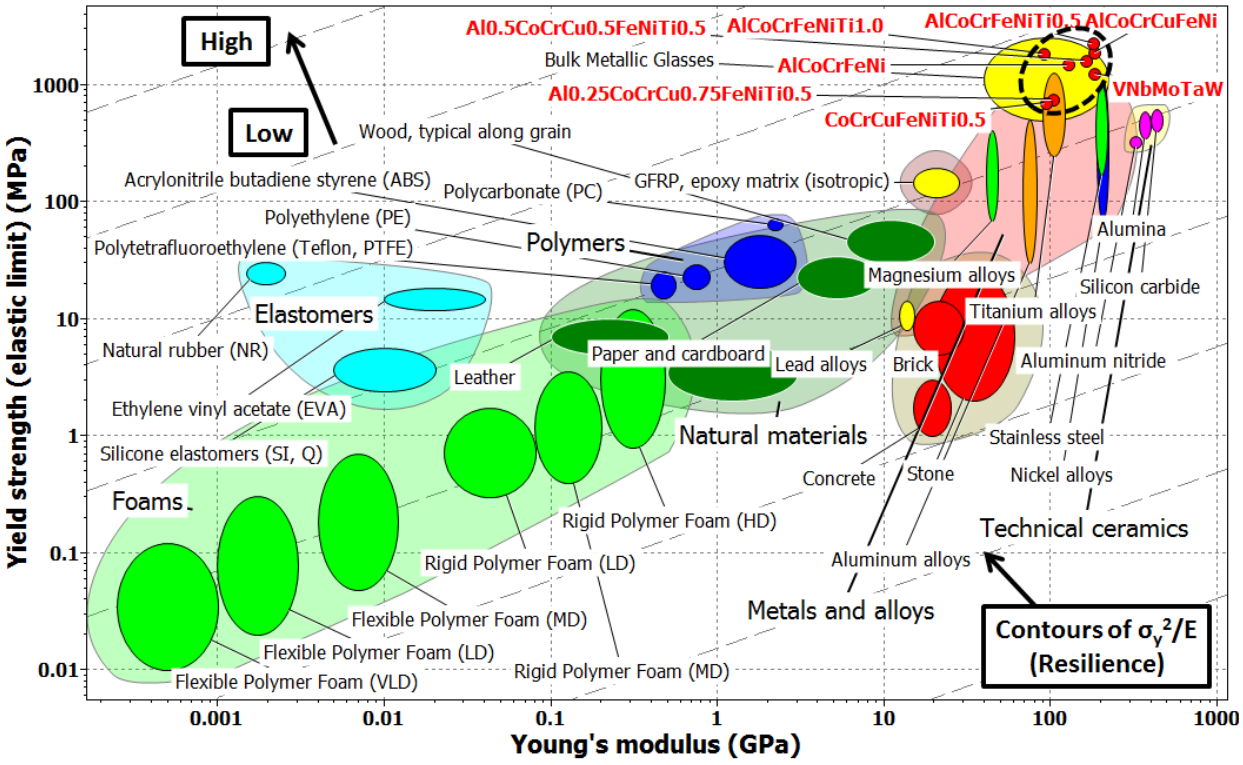

Figure 1. An Ashby map showing yield strength (σ_y) versus Young's modulus (E) ranges at room temperature for foams, natural materials, elastomers, ceramics, polymers, composites, and metals, along with data for BMGs and some HEAs. The contours show the material indices or guide lines for the resilience, σ_y^2/E.

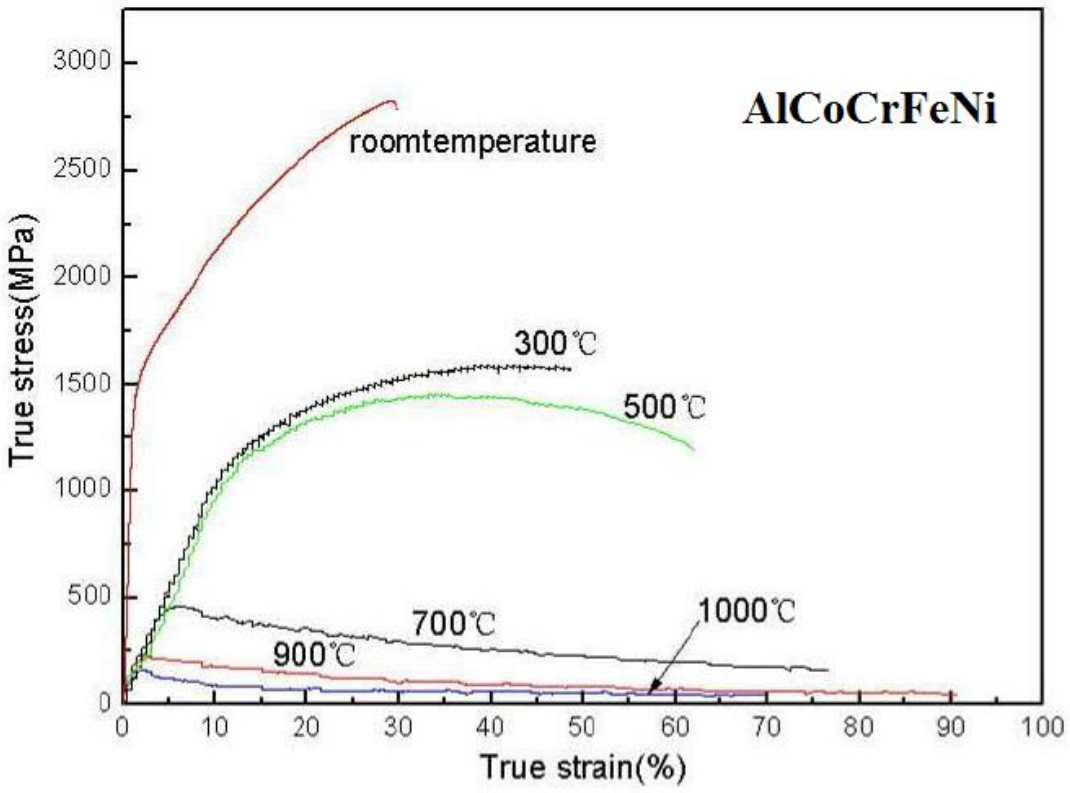

Figure 2. Compressive engineering stress-engineering strain curves of the AlCoCrFeNi at room and elevated temperatures. (Literature results from [49])

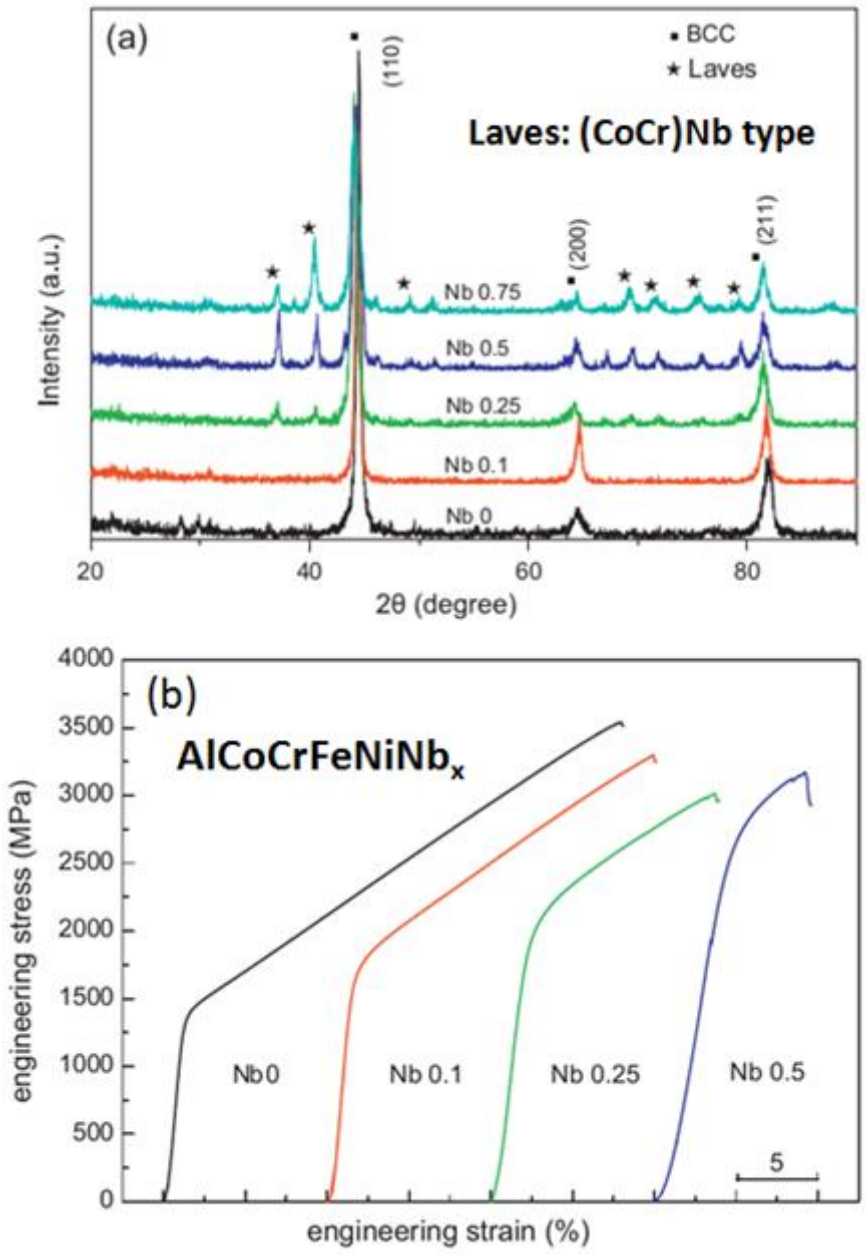

Figure 3. (a) The addition of Nb elements (x = 0, 0.1, 0.25, 0.5, and 0.75) into this HEA changes the original phase constitution, which yields the formation of ordered Laves phase besides solid solution phase. (b) The compressive stress-strain curves of the AlCoCrFeNiNbx cylindrical samples with a diameter of 5 mm (x = 0, 0.1, 0.25, and 0.5). Literature results from [44]

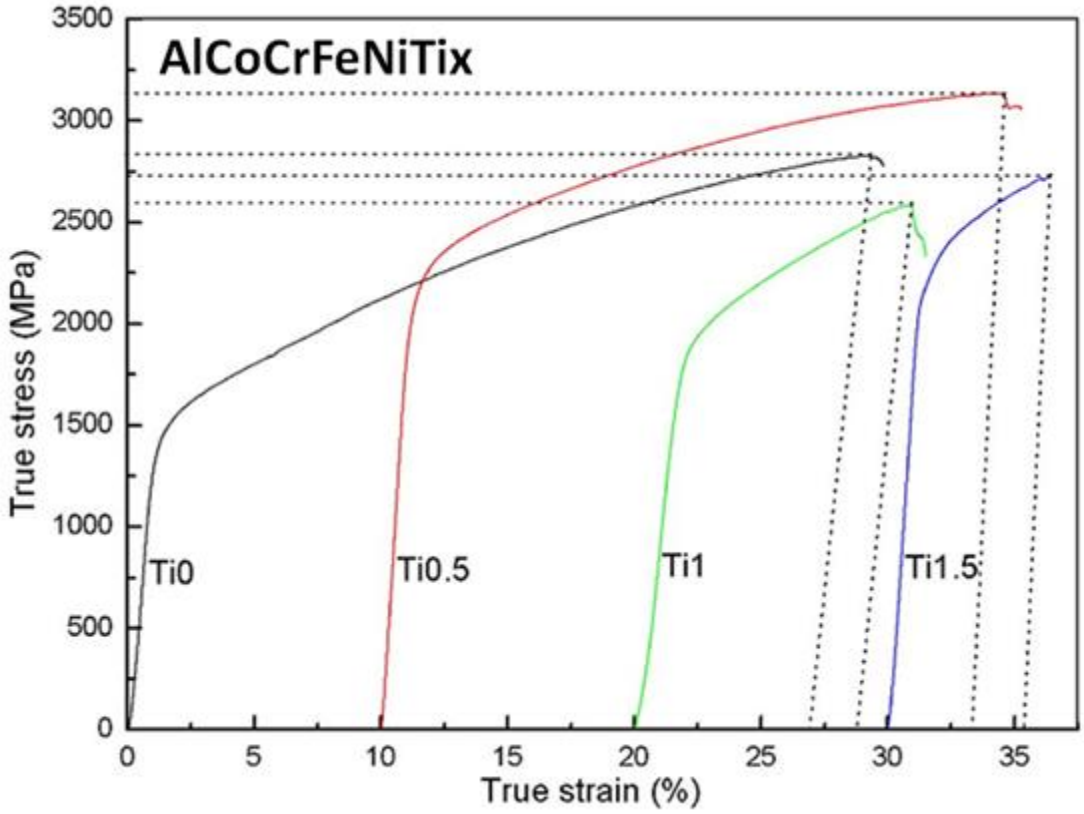

Figure 4. Compressive true stress-strain curves of AlCoCrFeNiTix alloy cylindrical samples with a diameter of 5 mm. Literature results from [4]

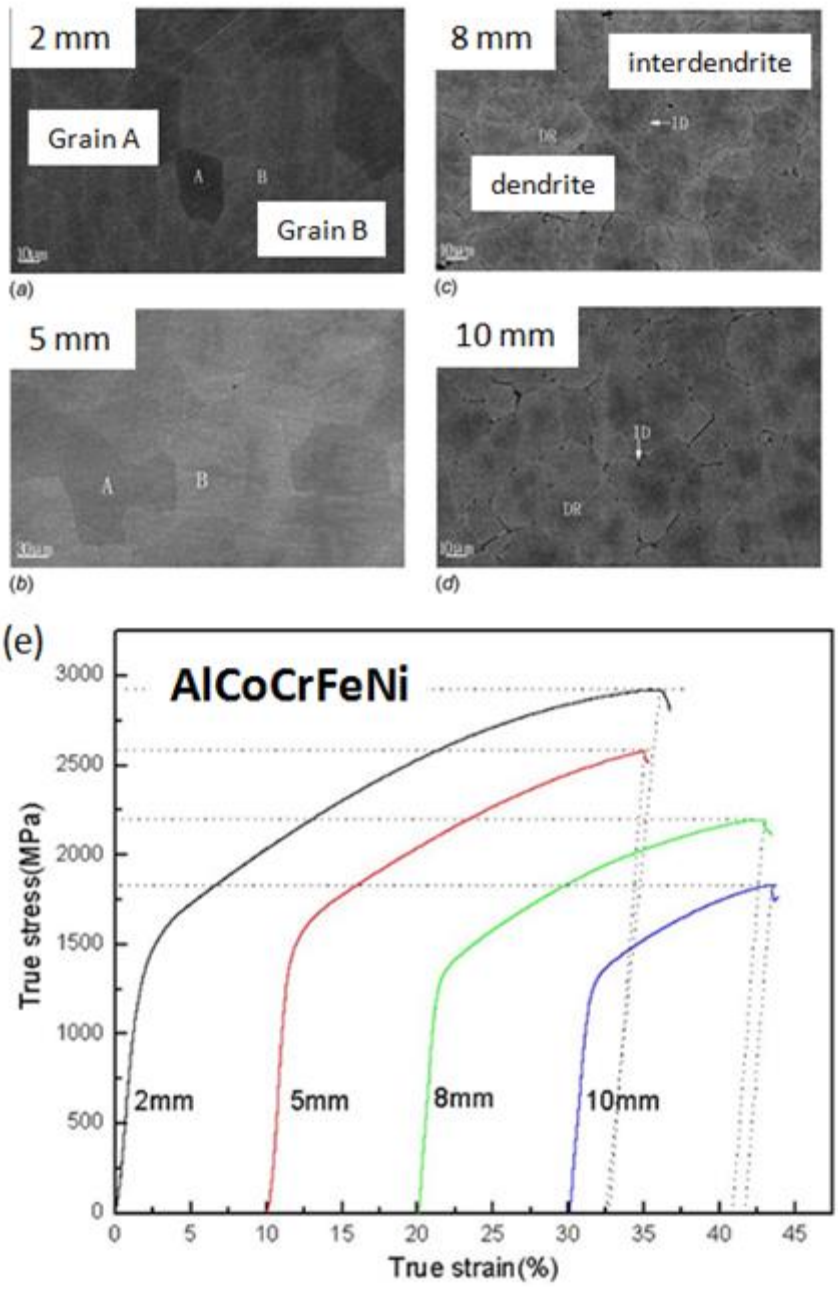

Figure 5. As the cooling rate increasing, the percentage of interdendritic phase is reduced (a-d), but both the strength and the plasticity are enhanced significantly (e). Compressive true stress-true strain curves for the AlCoCrFeNi alloy cylindrical samples with different diameters. Literature results from [45]

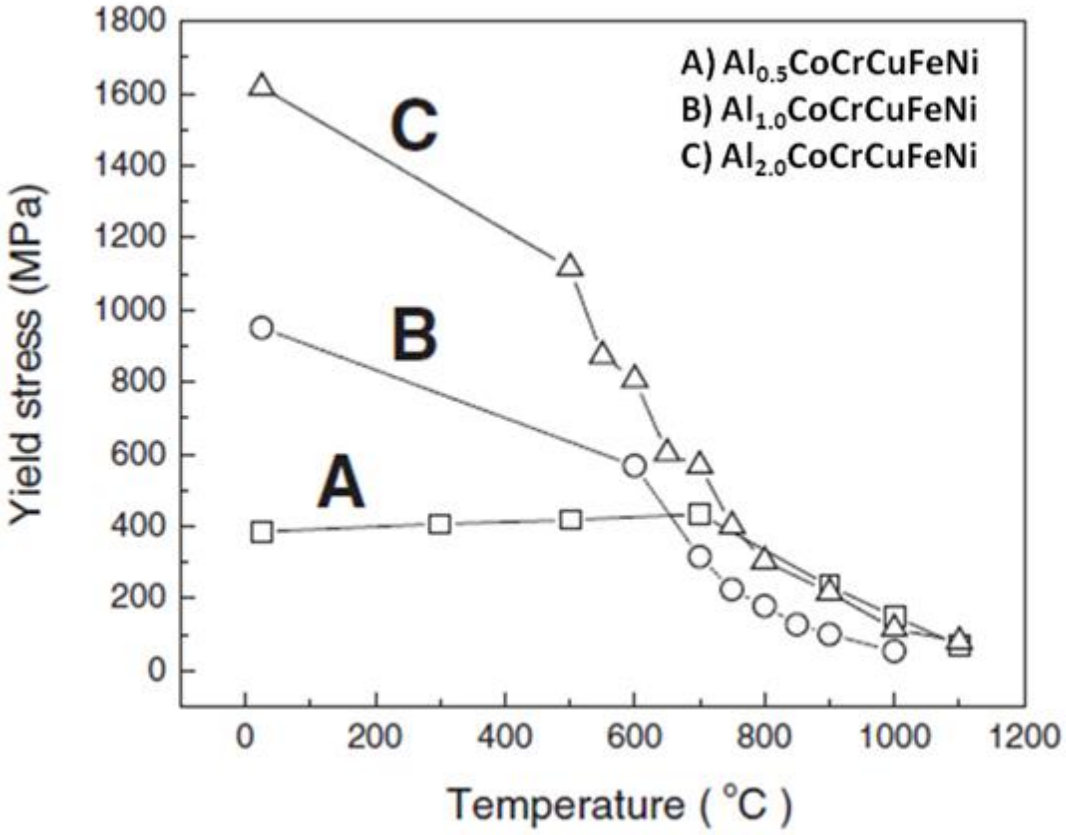

Figure 6. Compressive yield strength of AlxCoCrCuFeNi alloy system tested at different temperatures: A) Al0.5CoCrCuFeNi, B) Al1.0CoCrCuFeNi, and C) Al2.0CoCrCuFeNi alloys. Literature results from [3]

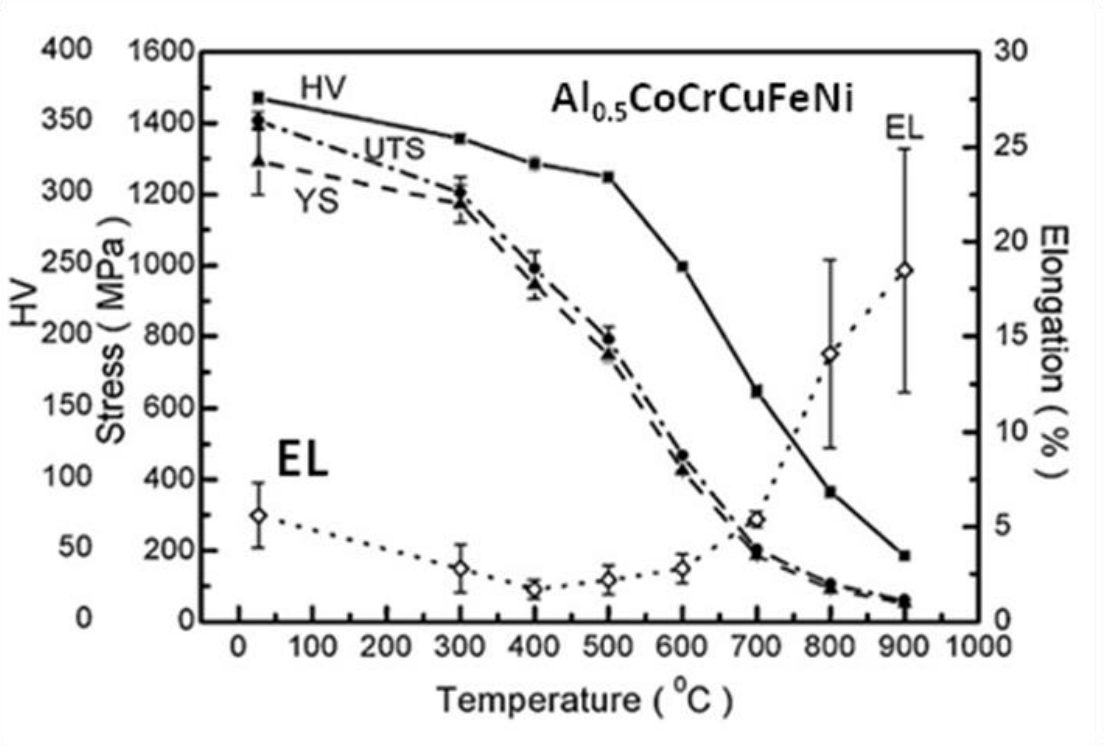

Figure 7. Hardness, strength, and elongation as a function of temperature for as-rolled samples.

Literature results from [39]

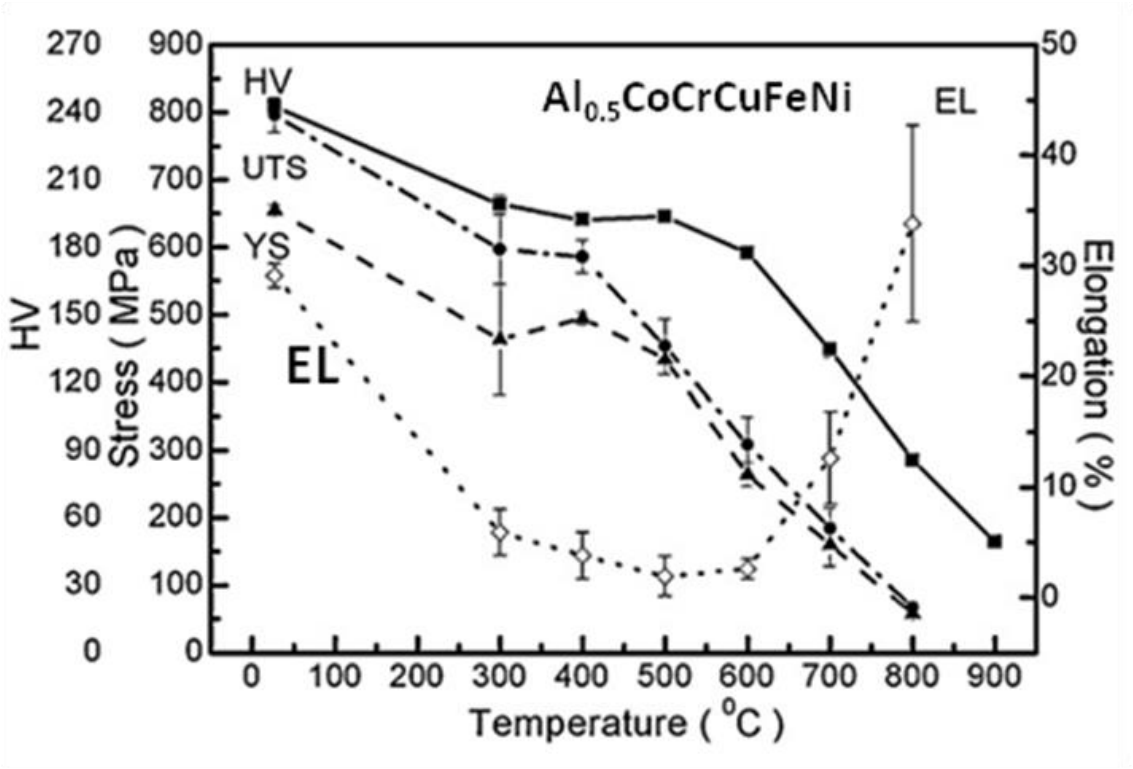

Figure 8. Hardness, strength and elongation as a function of temperature for as-annealed samples. Literature results from [39]

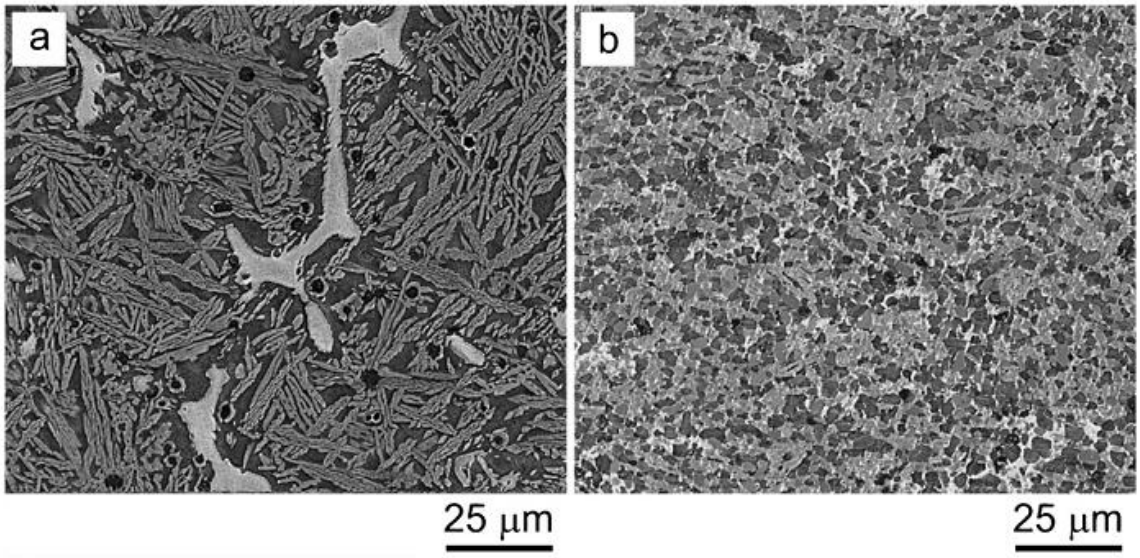

Figure 9. Microstructures of the AlCrCuNiFeCo HEA in (a) as-cast and (b) hot-forged conditions. Literature results from [35]

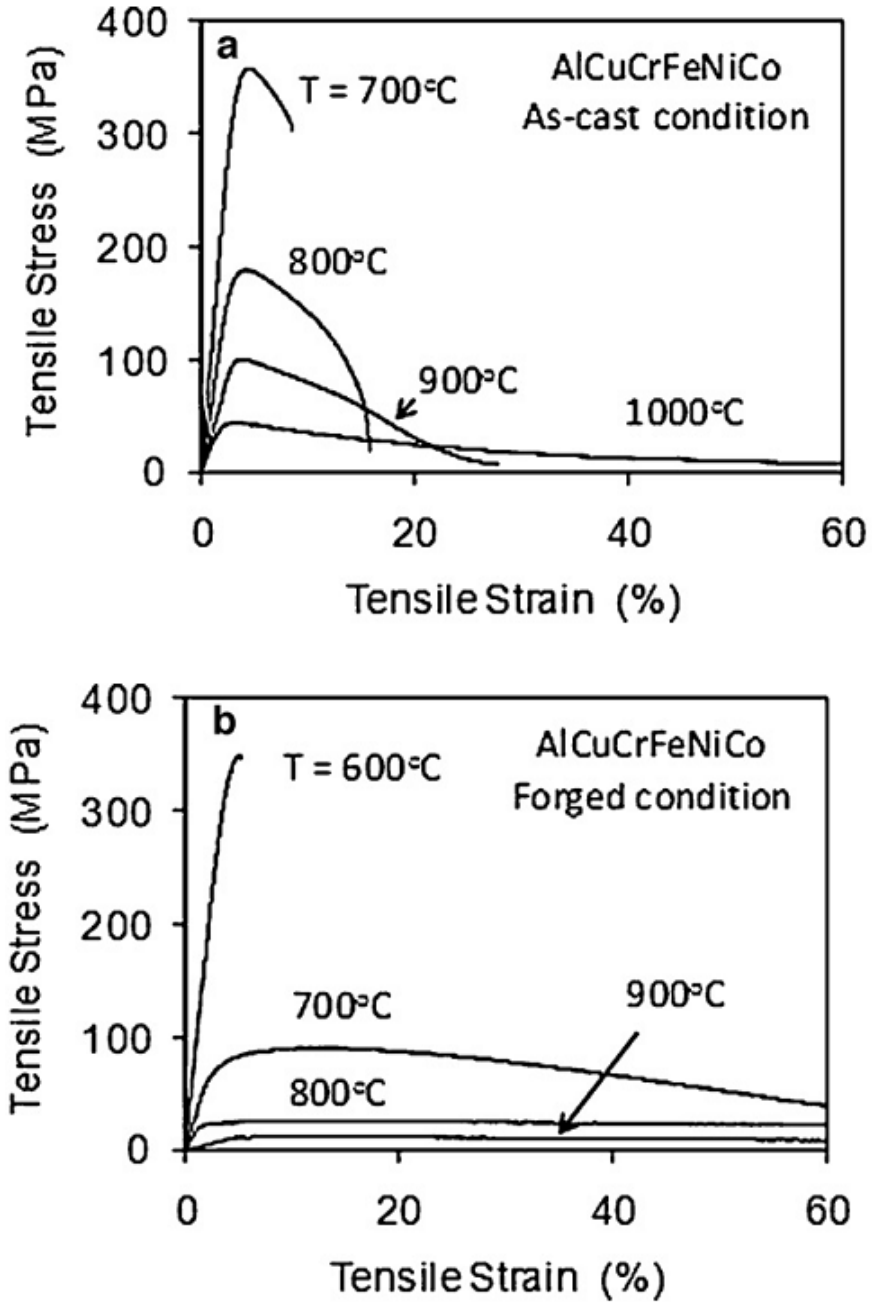

Figure 10. Typical stress-strain curves of AlCoCrCuFeNi (a) the as-cast and (b) hot-forged samples deformed at different temperatures and the initial strain rate of 10^{-3} s^{-1}. Literature results from [35]

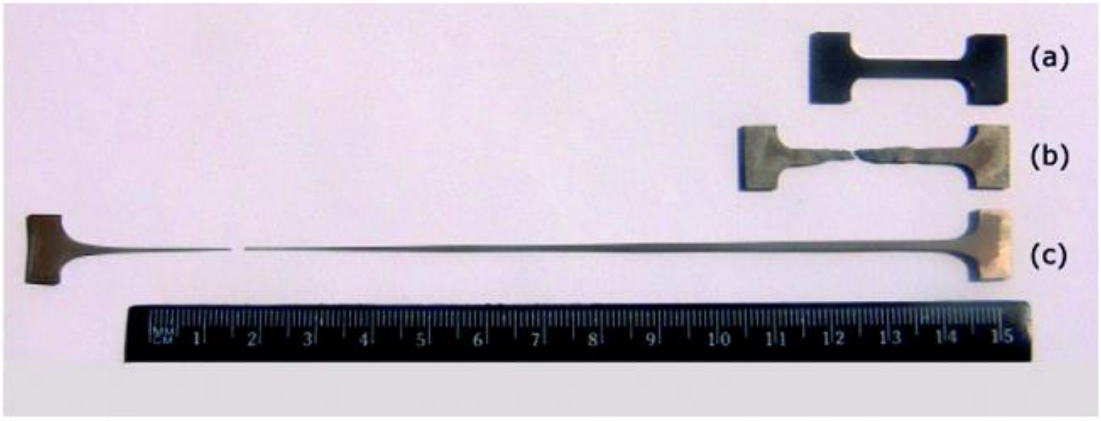

Figure 11. Photographs of AlCoCrCuFeNi tensile samples after deformation at 1,273 K: (a) a non-deformed sample; (b) as-cast sample (ε = 77%); and (c) forged sample (ε = 864%). Strain rate =10^{-3} s^{-1}. Literature results from [35]

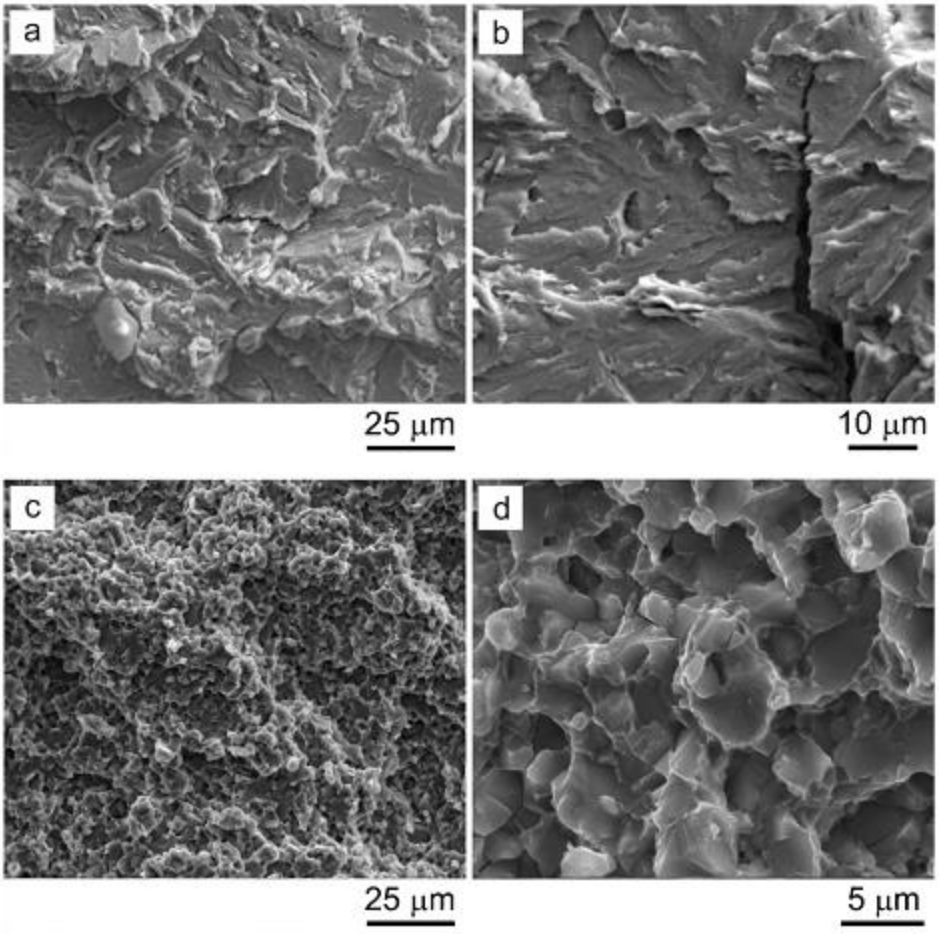

Figure 12. SEM images of the AlCoCrCuFeNi fracture surfaces of tensile samples after tensile-testing deformation at room temperature. a and b: as-cast; c and d: hot-forged conditions. Literature results from [35]

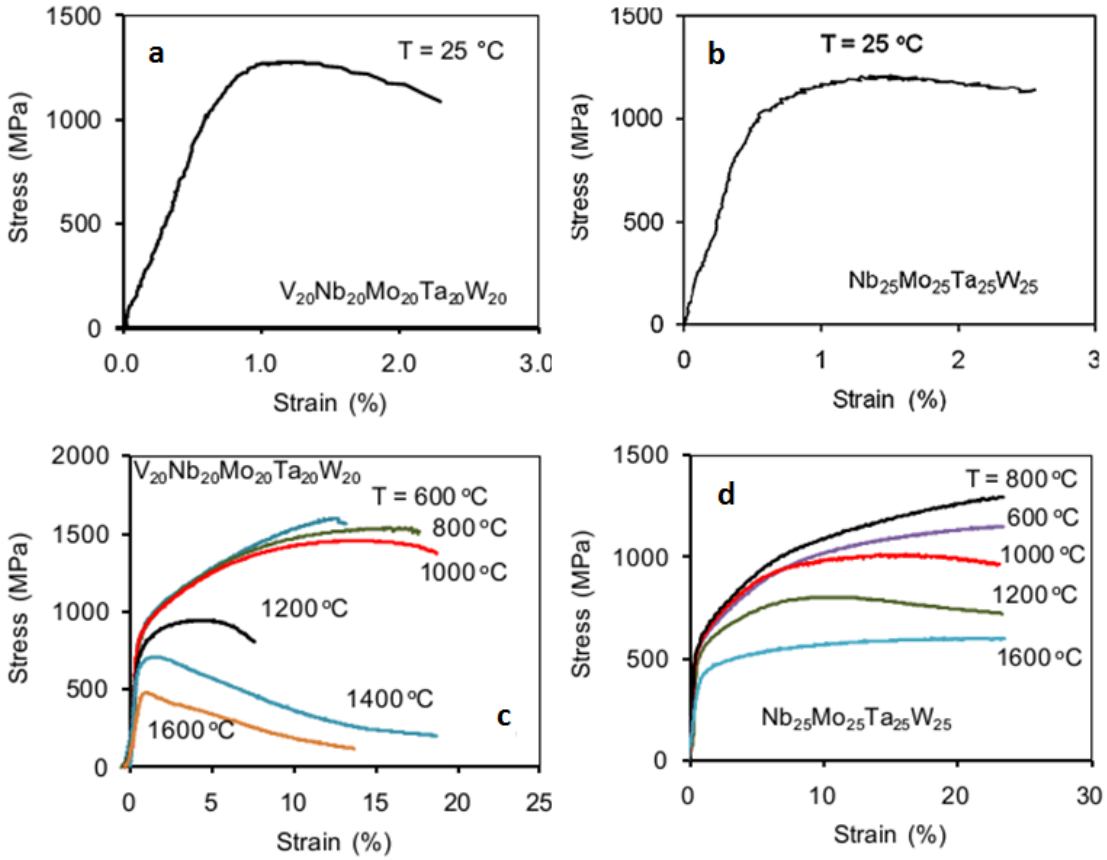

Figure 13. Compressive engineering stress-strain curves of NbMoTaW and VNbMoTaW HEAs at room and high temperatures. Literature results from [21]

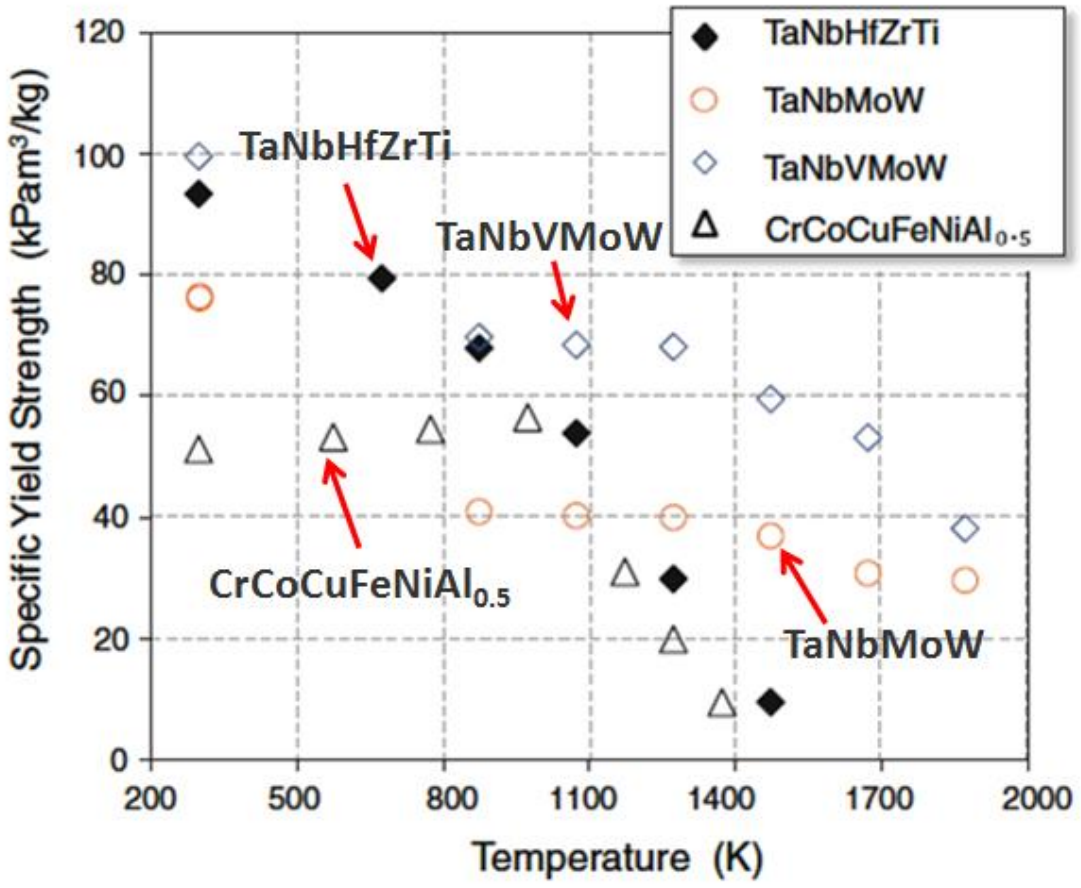

Figure 14. The temperature dependence of the specific yield-strength of the TaNbHfZrTi alloy in comparison with those for TaNbMoW, TaNbVMoW, and CrCoCuFeNiAl0.5 cast alloys. Literature results from [26]

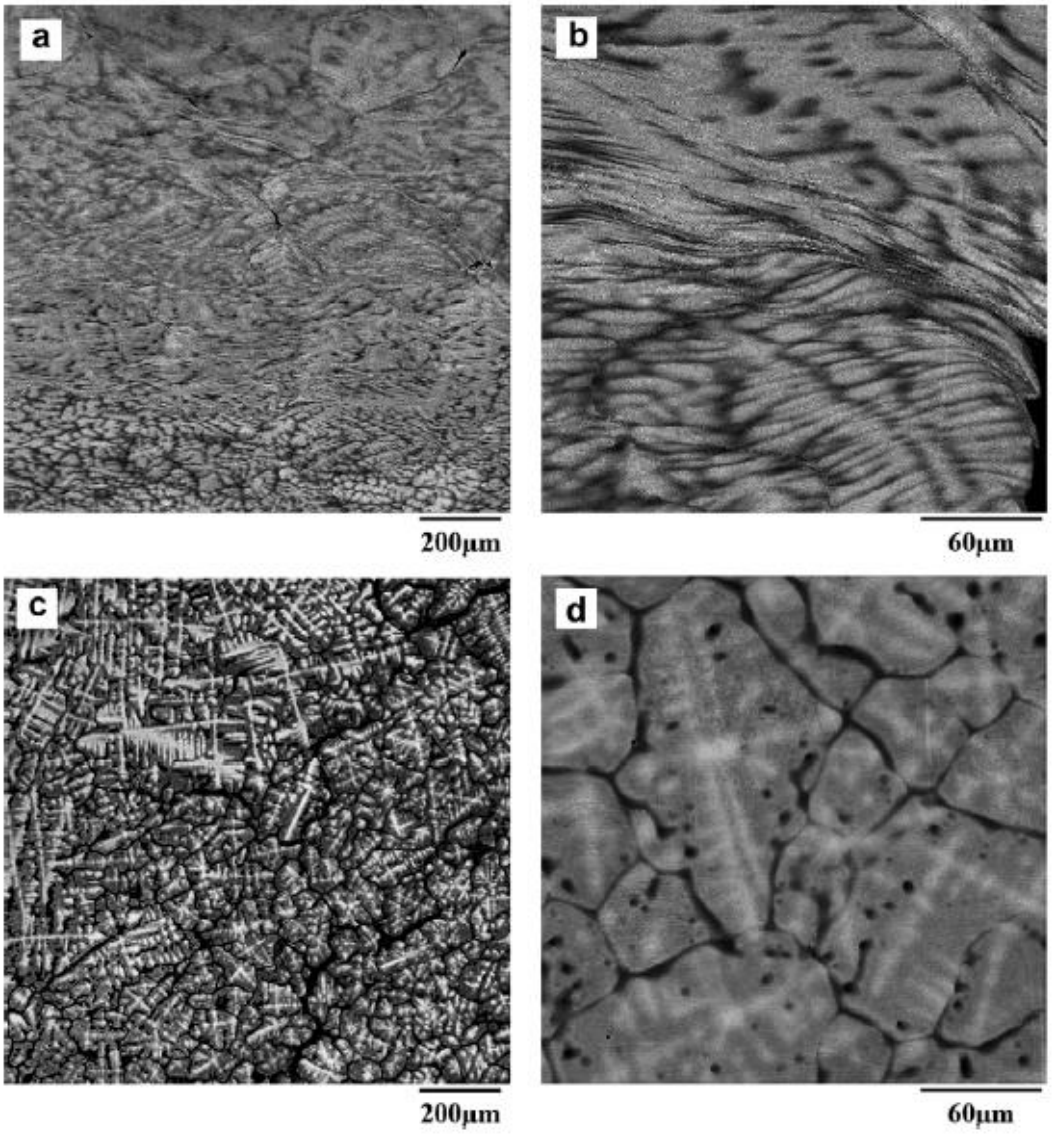

Figure 15. SEM backscatter images of the (a, b) Nb25Mo25Ta25W25 and (c, d) V20Nb20Mo20Ta20W20 alloys after compressive deformation at 1,673 K. Depicted crosssection are parallel to the loading direction (vertical) and located halfway between the surface and center of the samples. Literature results from [21]

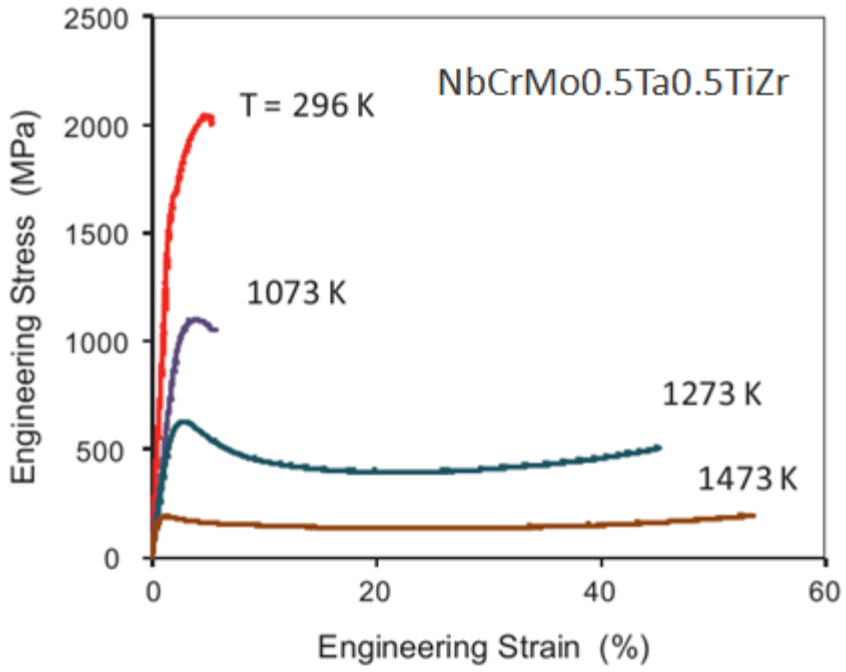

Figure 16. The engineering stress-strain compression curves of the NbCrMo0.5Ta0.5TiZr alloy samples after HIP at 296 K, 1,073 K, 1,273 K, and 1,473 K. Literature results from [58]

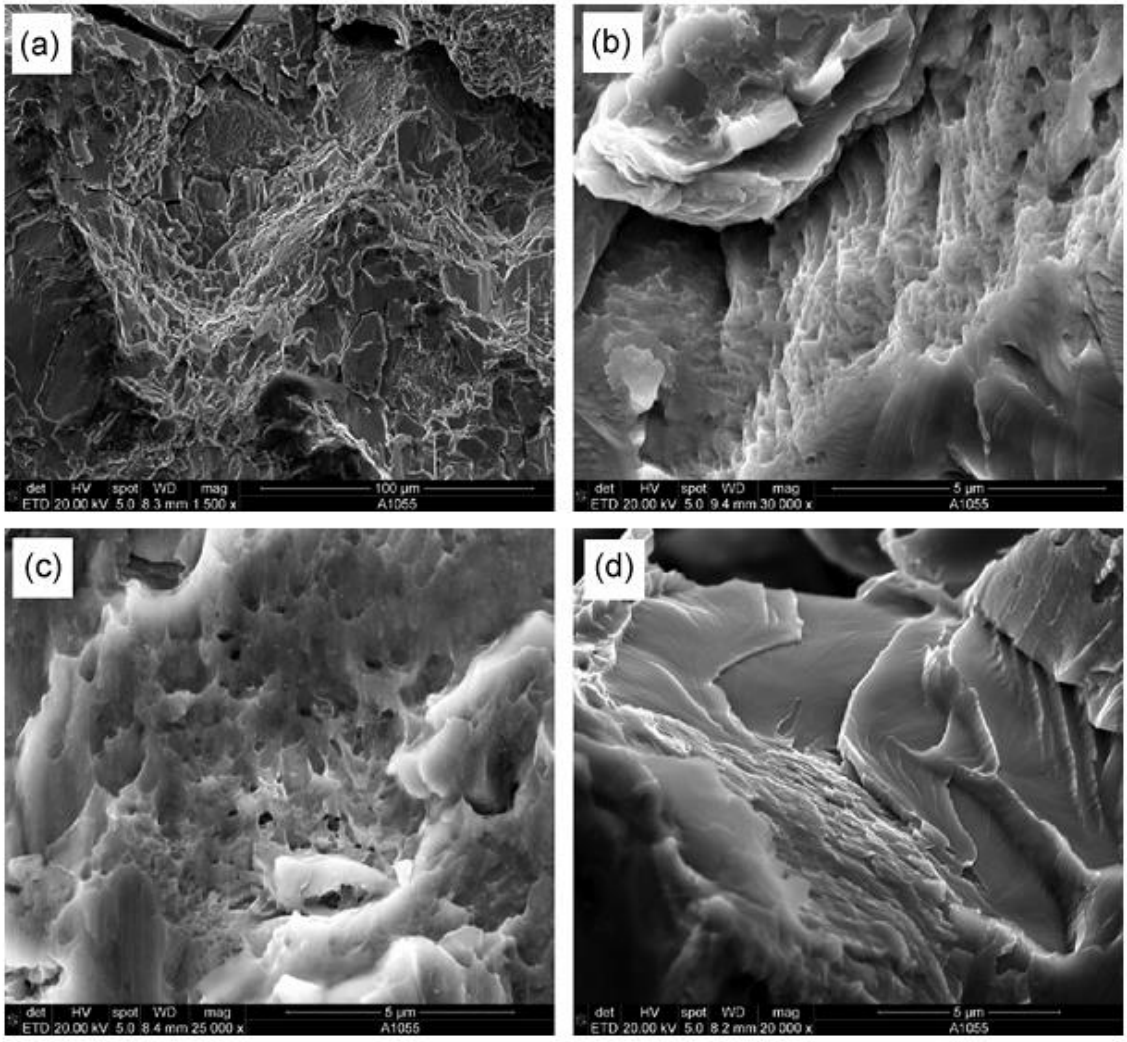

Figure 17. SEM secondary electron images of the fracture surface of a NbCrMo0.5Ta0.5TiZr alloy sample after compression deformation at room temperature. Literature results from [58]

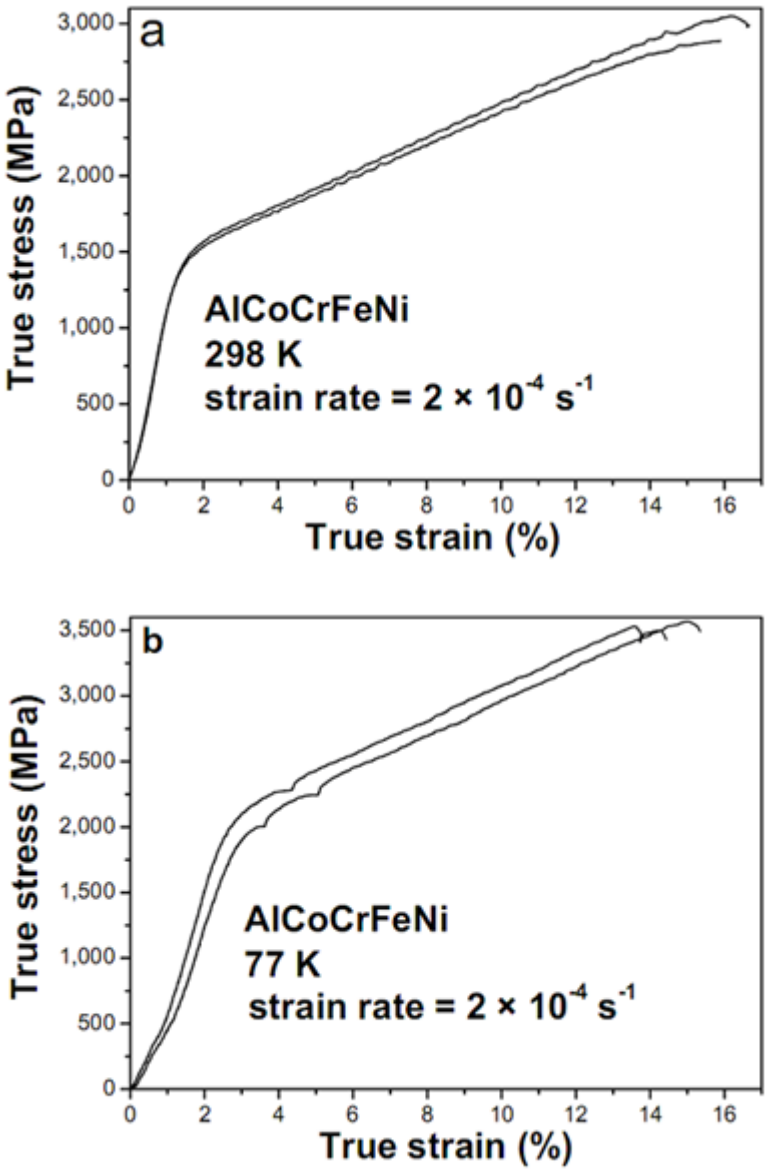

Figure 18. The compressive true stress-strain curves of the AlCoCrFeNi HEA at (a) 298 K and (b) 77 K. The yield strengths and fracture strengths at cryogenic temperatures increase distinguishably, compared to the corresponding mechanical properties at ambient temperature. Literature results from [63]

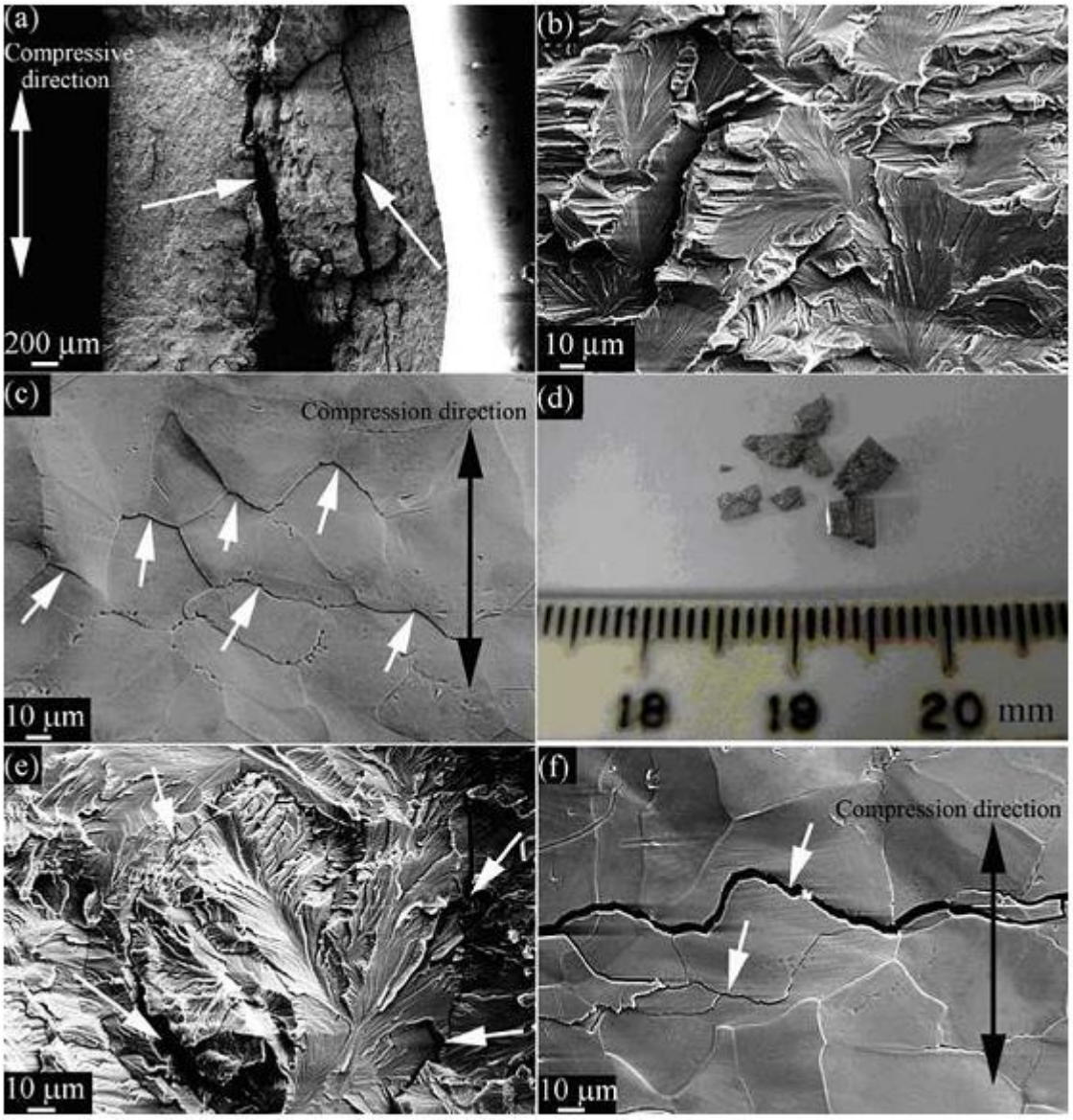

Figure 19. The low and high magnifications for the fracture surfaces of the AlCoCrFeNi HEA at 298 K shown in (a) and (b), respectively; The lateral surface of the deformed sample of the AlCoCrFeNi HEA at 298 K shown in (c); The low and high magnifications for the fracture surfaces of the AlCoCrFeNi HEA at 77 K shown in (d) and (e), respectively; The lateral surface of the deformed sample of the AlCoCrFeNi HEA at 77 K shown in (f). Literature results from [63]

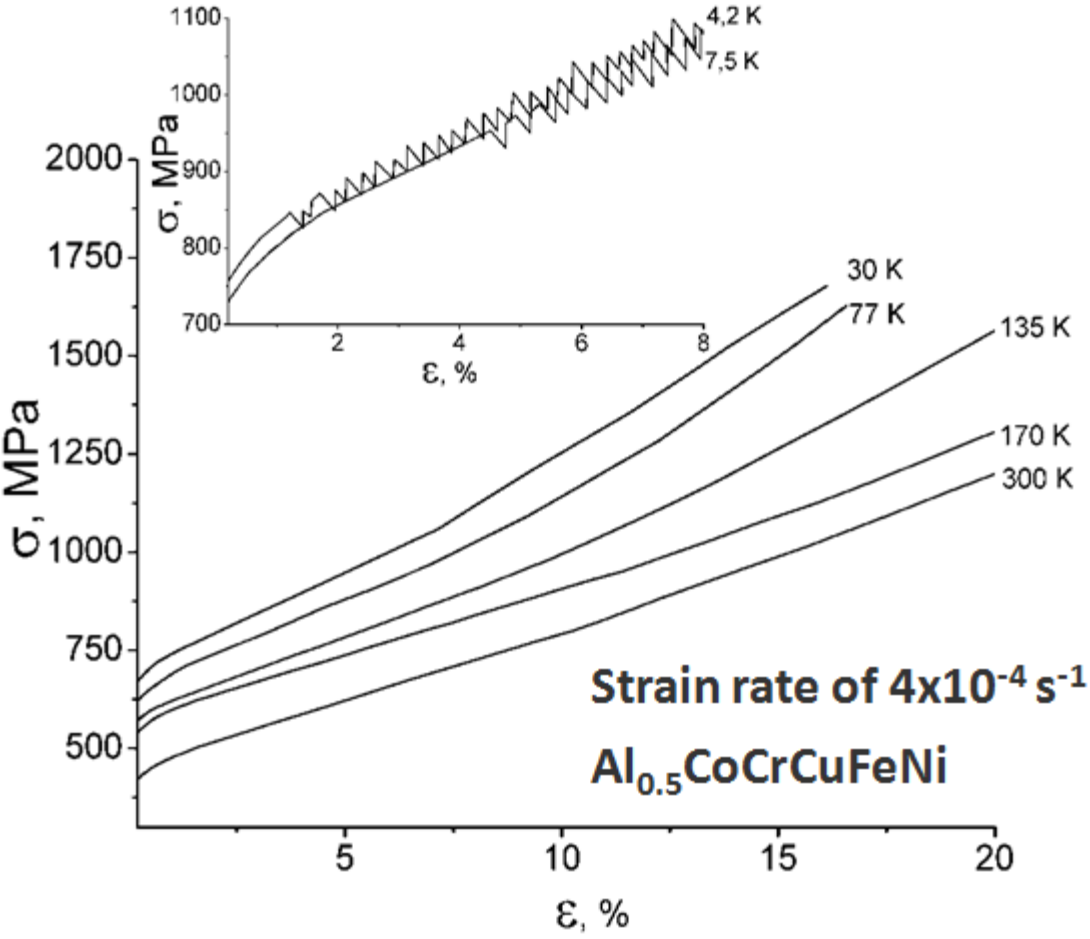

Figure 20. At all temperatures to 4.2 K, the Al0.5CoCuCrFeNi HEA possesses high plasticity under compression At temperatures below 15 K, the curves take a serrated shape. The inserted figure illustrates a typical serrated stress-strain curve. Literature results from [64]

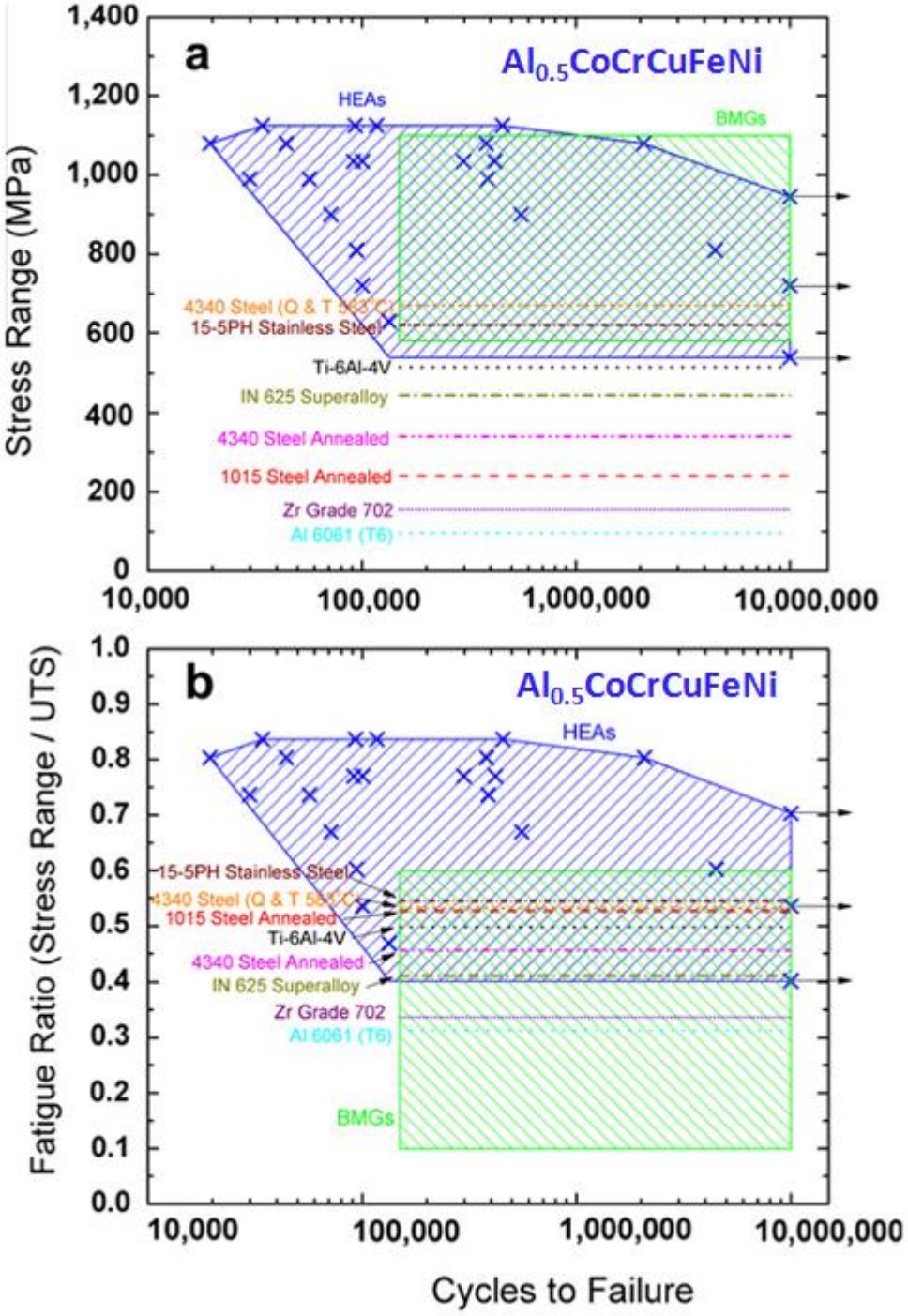

Figure 21. S-N curves comparing the fatigue ratios of the Al0.5CoCrCuFeNi HEA, other conventional alloys, and bulk metallic glasses. Literature results from [7]

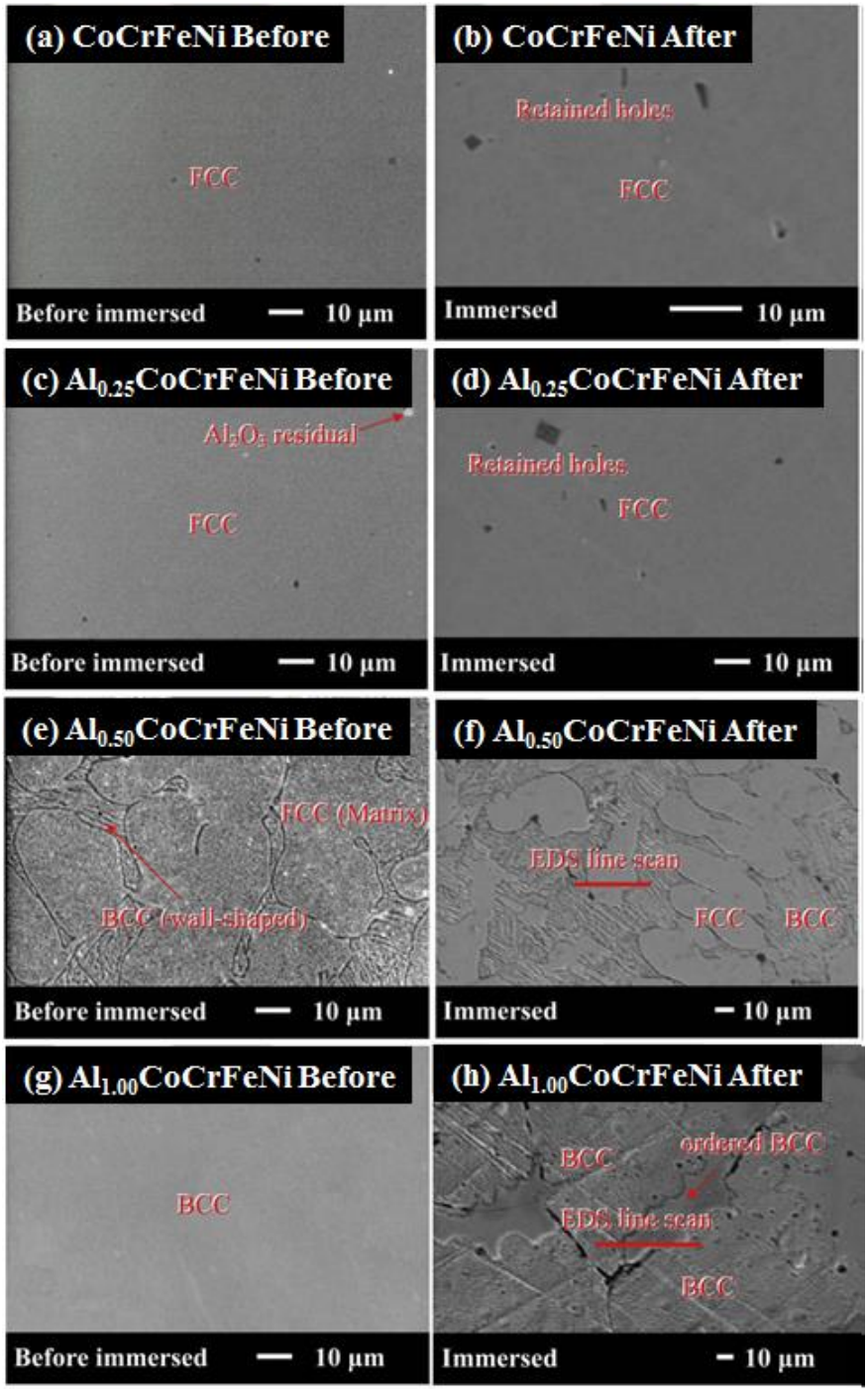

Figure 22. Microstructures of $Al_xCoCrFeNi$ before and after 3-day immersion test in 0.5 M H_2SO_4. Literature results from [51]

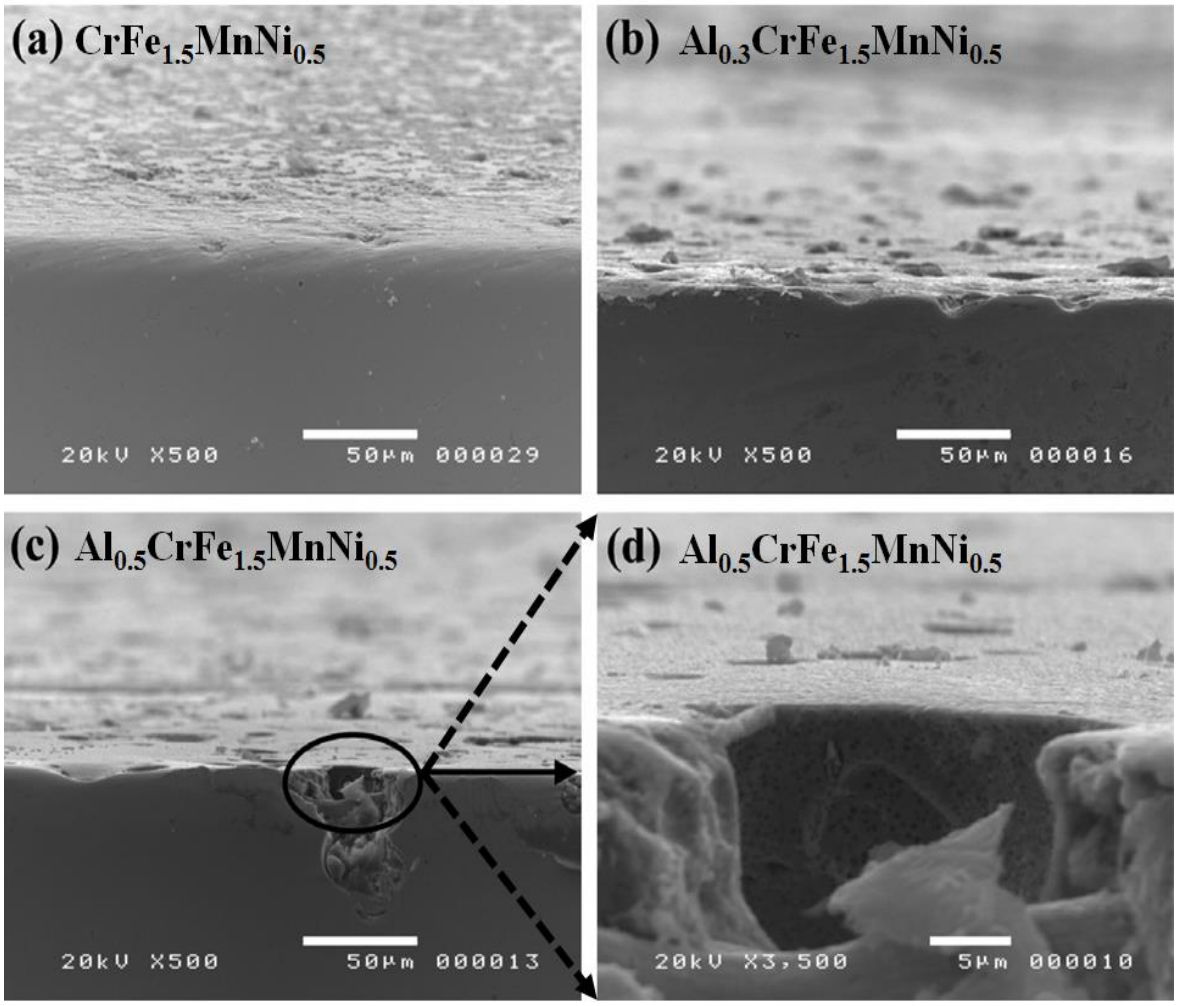

Figure 23. SEM micrographs for the $Al_xCrFe_{1.5}MnNi_{0.5}$ alloys with different Al contents (a) x = 0, (b) x = 0.3 mol, (c) x = 0.5 mol, and (d) a close-up look in the circled area of the micrograph (c), after anodic polarization exceeded the breakdown potential (> 1.25 V_{SHE}) in 0.5 M H_2SO_4. Literature results from [78]

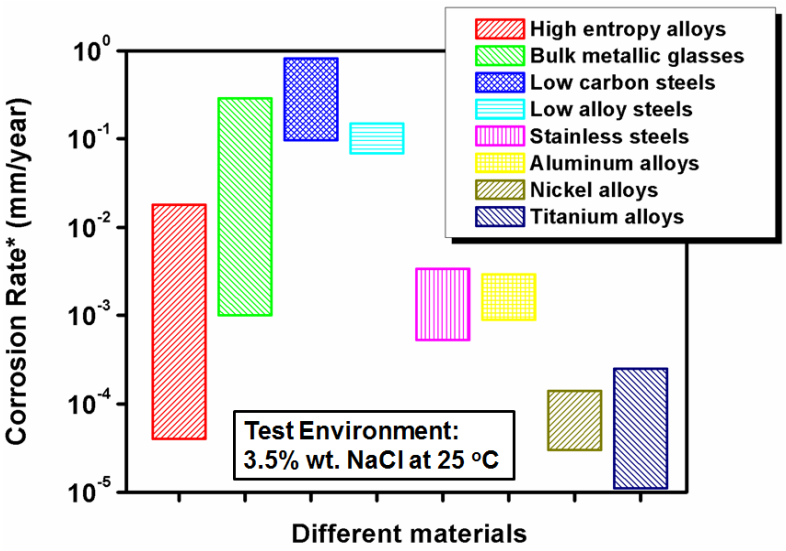

* Average corrosion rates are obtained, including electrochemical measurements and weight loss method. Some corrosion rates of conventional alloys were tested in seawater for comparison.

Figure 24. A comparison to average corrosion rates (mm/year) between HEAs and other materials in the 3.5 wt.% NaCl solution at room temperature [33, 77, 82, 154-157]

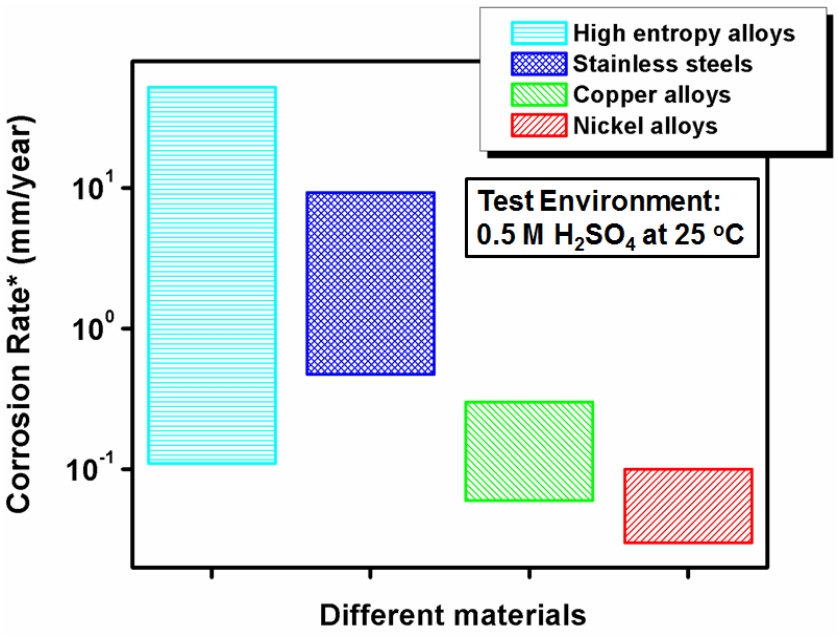

* Average corrosion rates are obtained, including electrochemical measurements and weight loss method.

Figure 25. A comparison to average corrosion rates (mm/year) between HEAs and conventional alloys in the 0.5 M H_2SO_4 solution at room temperature [51, 78, 157, 158].

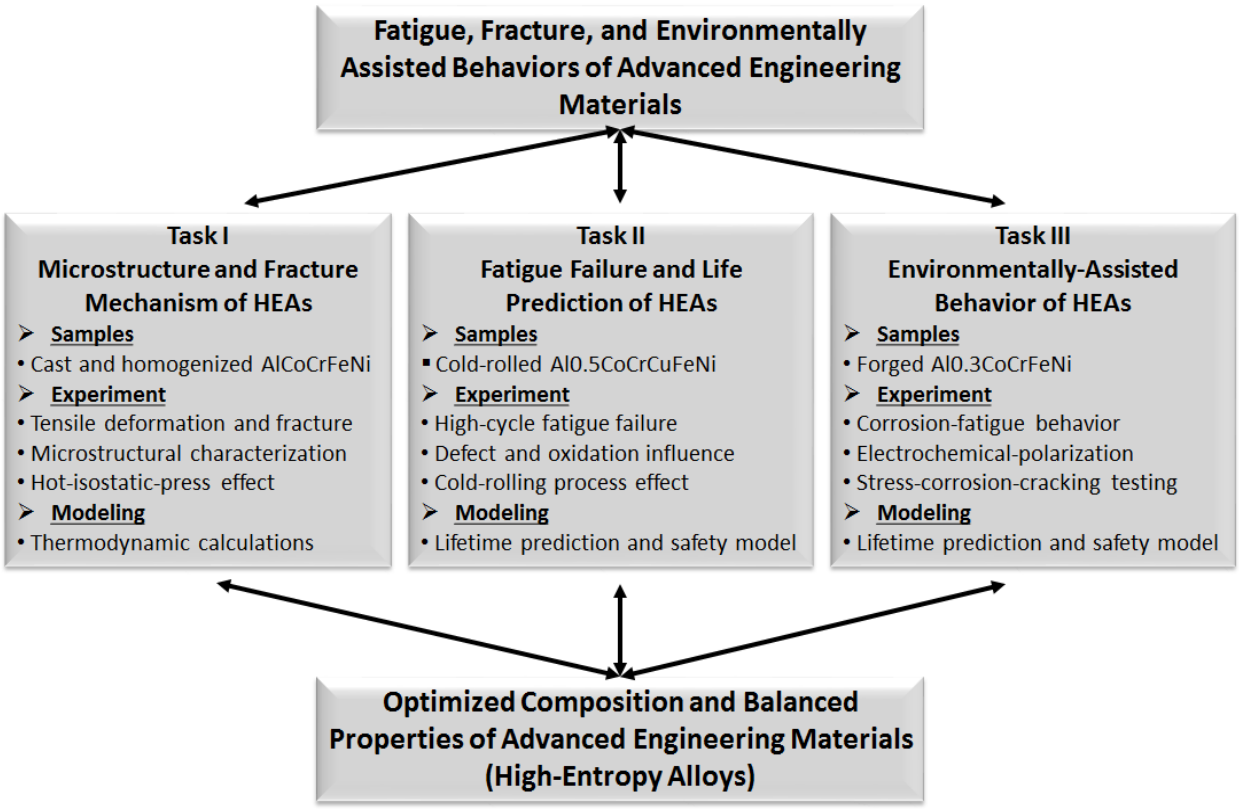

Figure 26. Overall framework for the research work

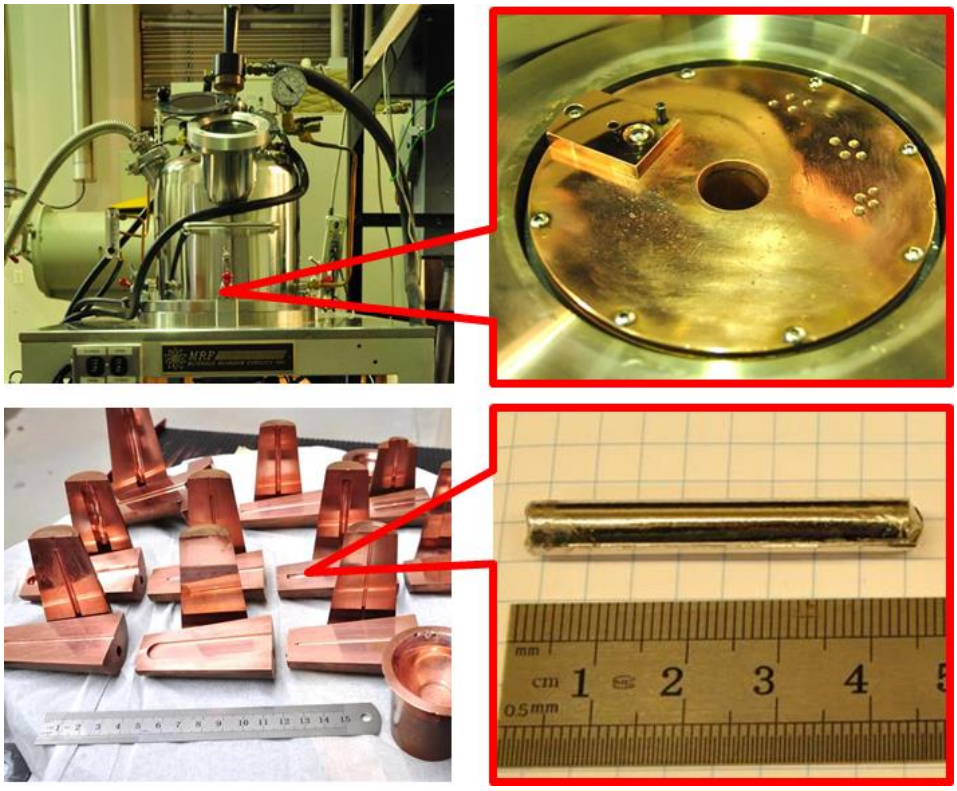

Figure 27. The fabrication process of as-cast AlCoCrFeNi samples through arc-melting and drop-casting methods.

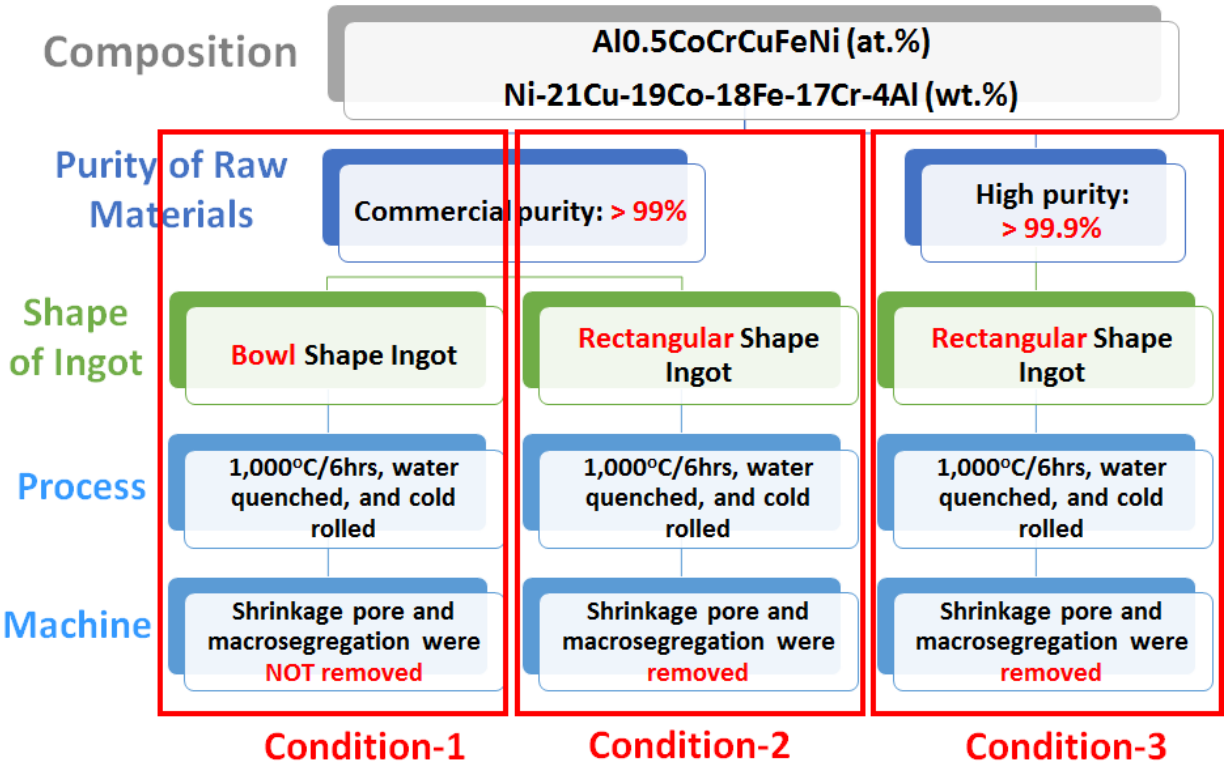

Figure 28. Three conditions of fatigue samples, prepared by different combinations of purity of raw materials, shape of ingot, processing, and machining

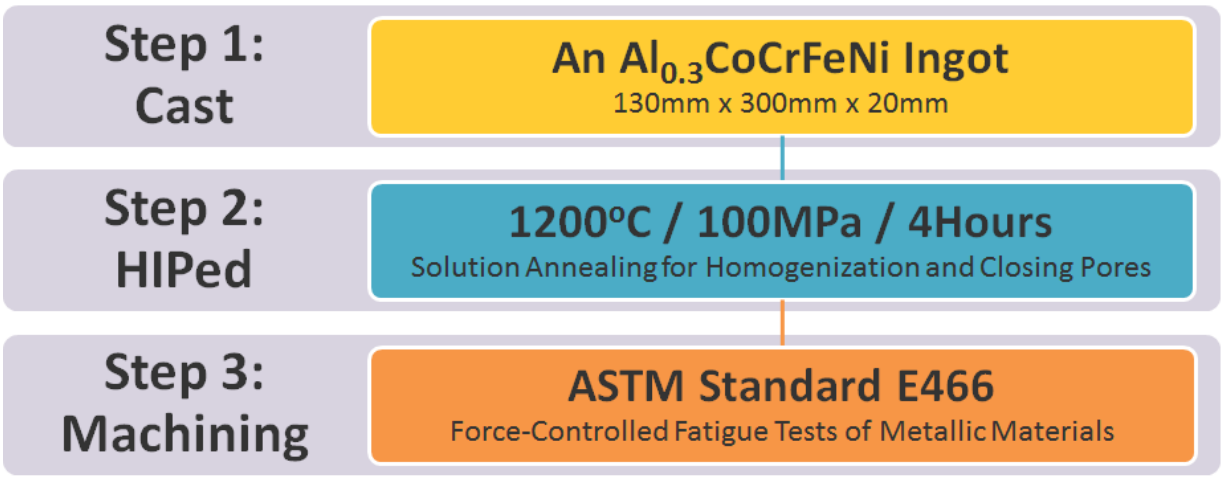

Figure 29. Material processing of the single-phase FCC $Al_{0.3}$CoCrFeNi alloy

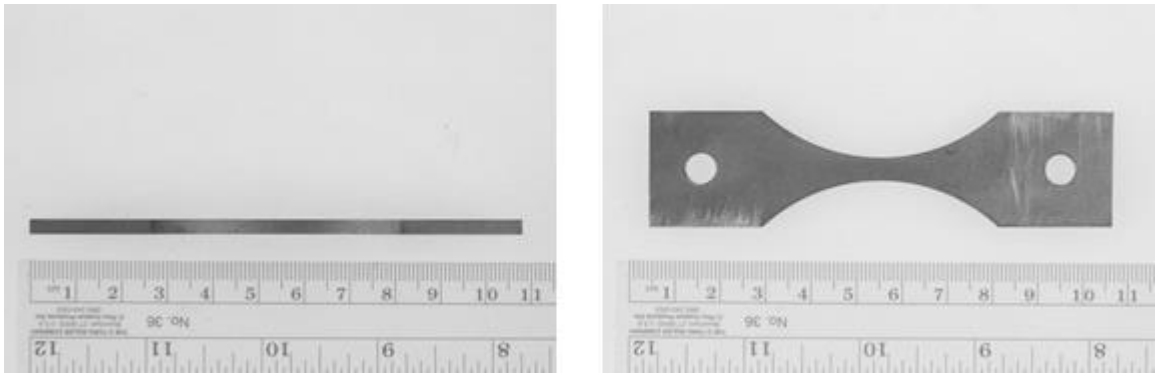

Figure 30. The flat fatigue specimen geometry with continuous radius between ends according to ASTM E466 [103]

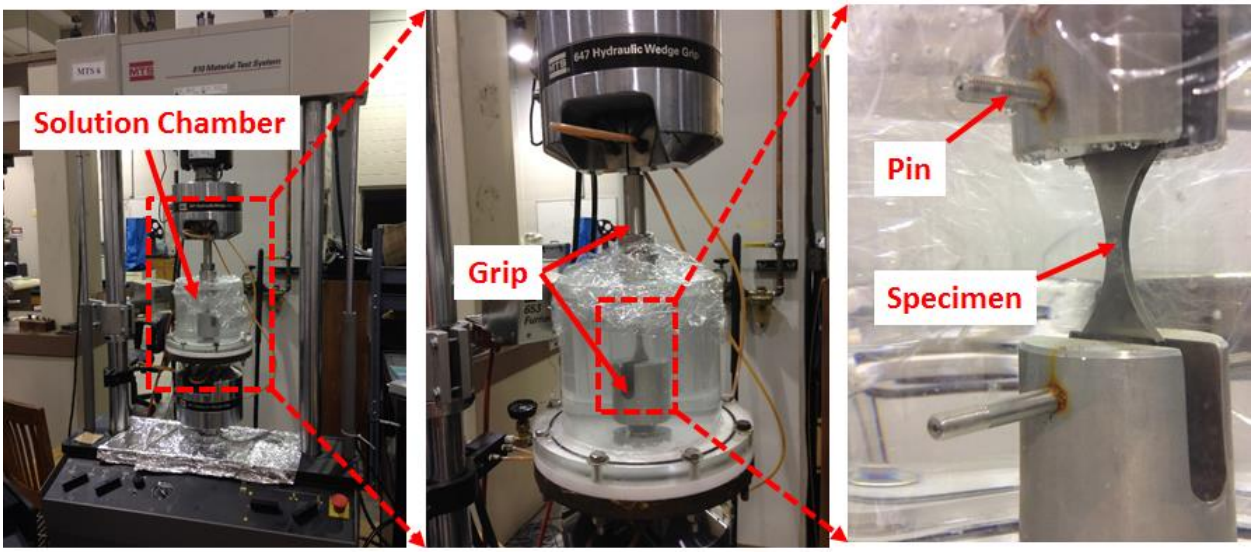

Figure 31. Diagram of corrosion-fatigue test configuration

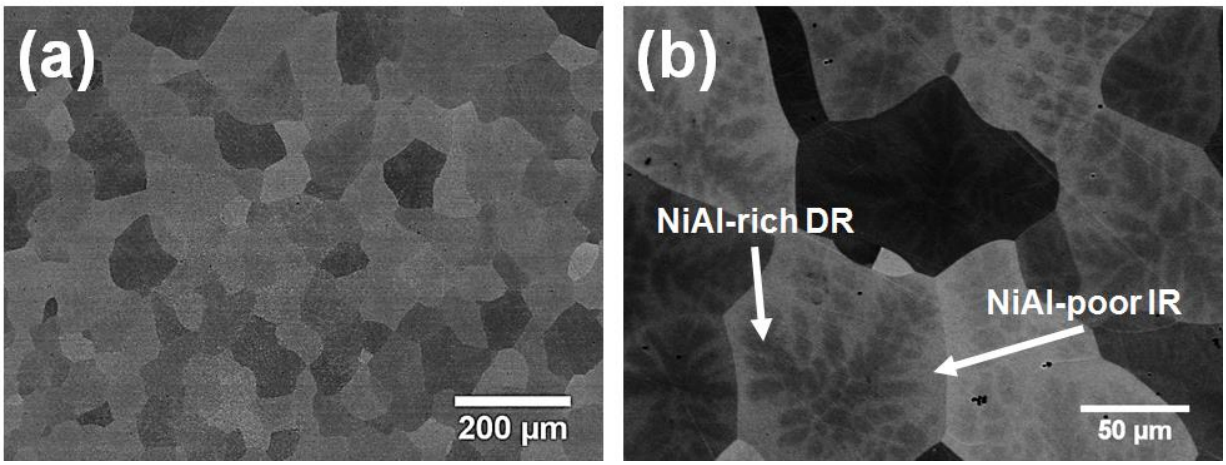

Figure 32. Back-scatter-electron (BSE) images of the as-cast alloy at two magnifications showing NiAl-rich dendrites (DR) and NiAl-poor interdendrites (IR)

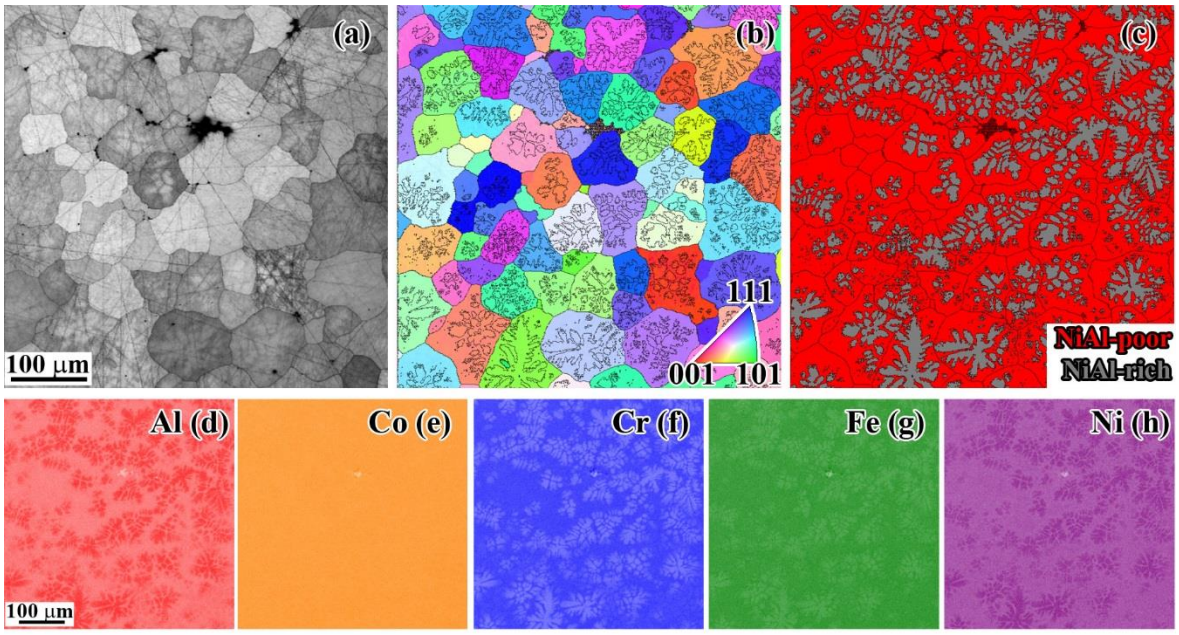

Figure 33. The EBSD (a) image-quality map, (b) inverse pole-figure map, and (c) phase map. Black lines in (b-c) are phase or grain boundaries. Simultaneously-acquired EDS (d-h) X-ray maps of the microstructures of the AlCoCrFeNi-AC alloy.

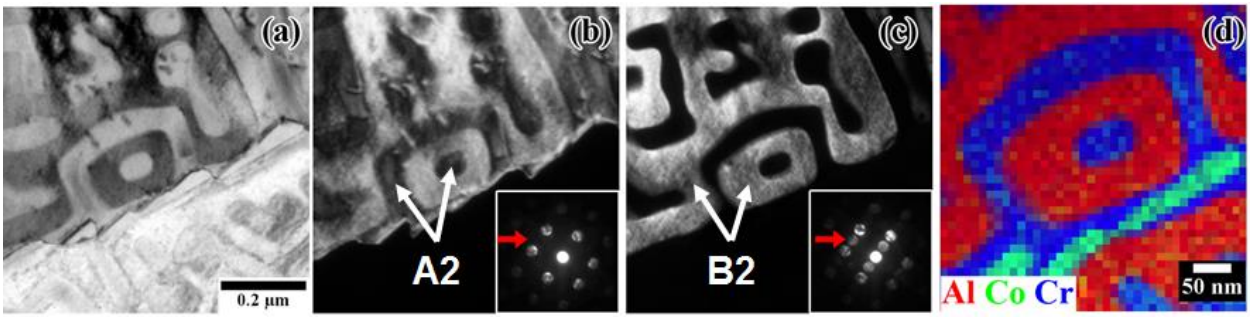

Figure 34. Bright-field and dark-field TEM images of the interior of the matrix grains: (a) is bright-field TEM, (b) fundamental A2 dark-field TEM, and (c) superlattice B2 dark-field TEM images. Insets to (b-c) are convergent beam electron diffraction patterns from A2 and B2, respectively. Arrows denote the superlattice position of B2. (d) is a false-color STEM-EDS map showing Al (red), Co (green), and Cr (blue).

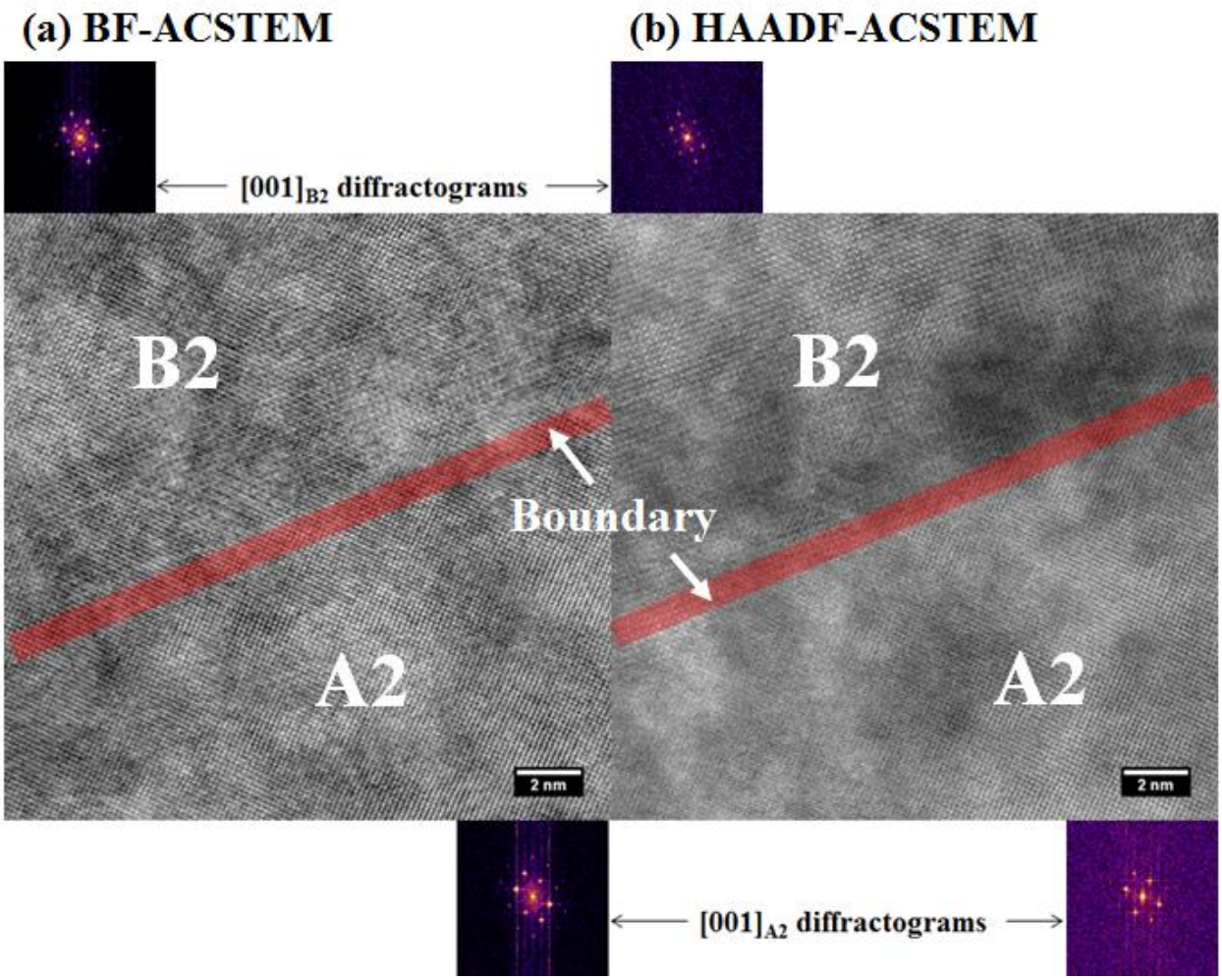

Figure 35. A BF-HAADF pair of AC-STEM images for the as-cast alloy showing A2+B2 structures

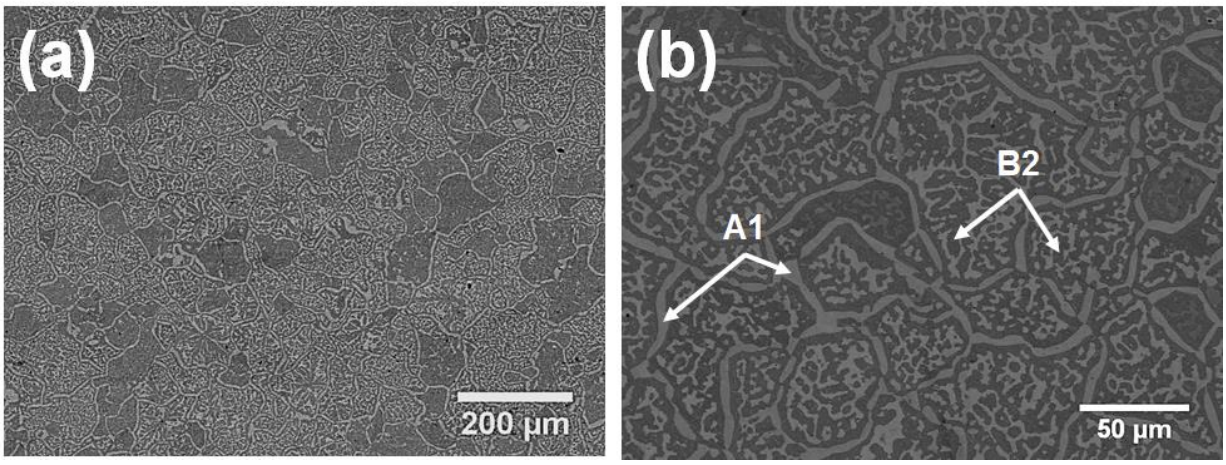

Figure 36. Back-scattered-electron (BSE) images of the homogenized alloy at two different magnifications.

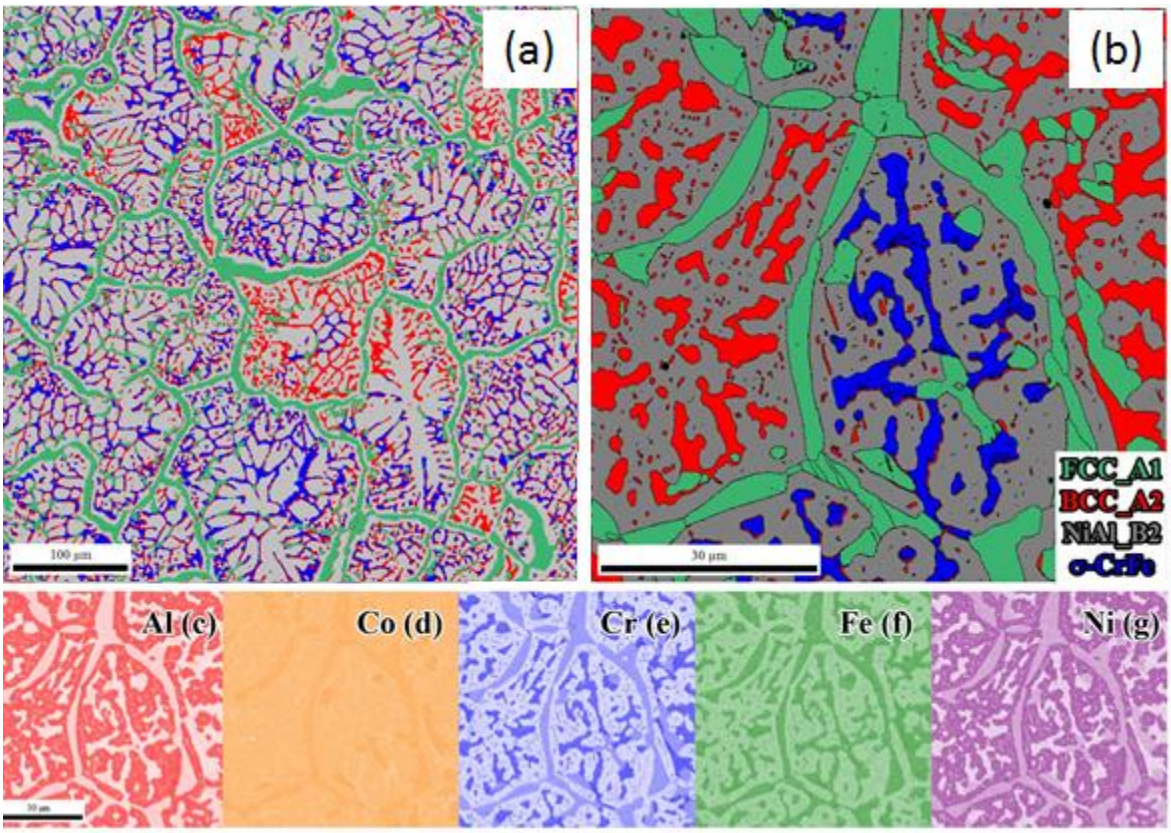

Figure 37. The phase-map microstructures of the AlCoCrFeNi-HP alloy. EBSD + EDS-derived phase map (a) low magnification and (b) high magnification. The EDS maps are presented in (c-g): B2 [(grey color in (a)], A2 [(red color in (a)], σ phase [(blue color in (a)], and A1 [(green color in (a)].

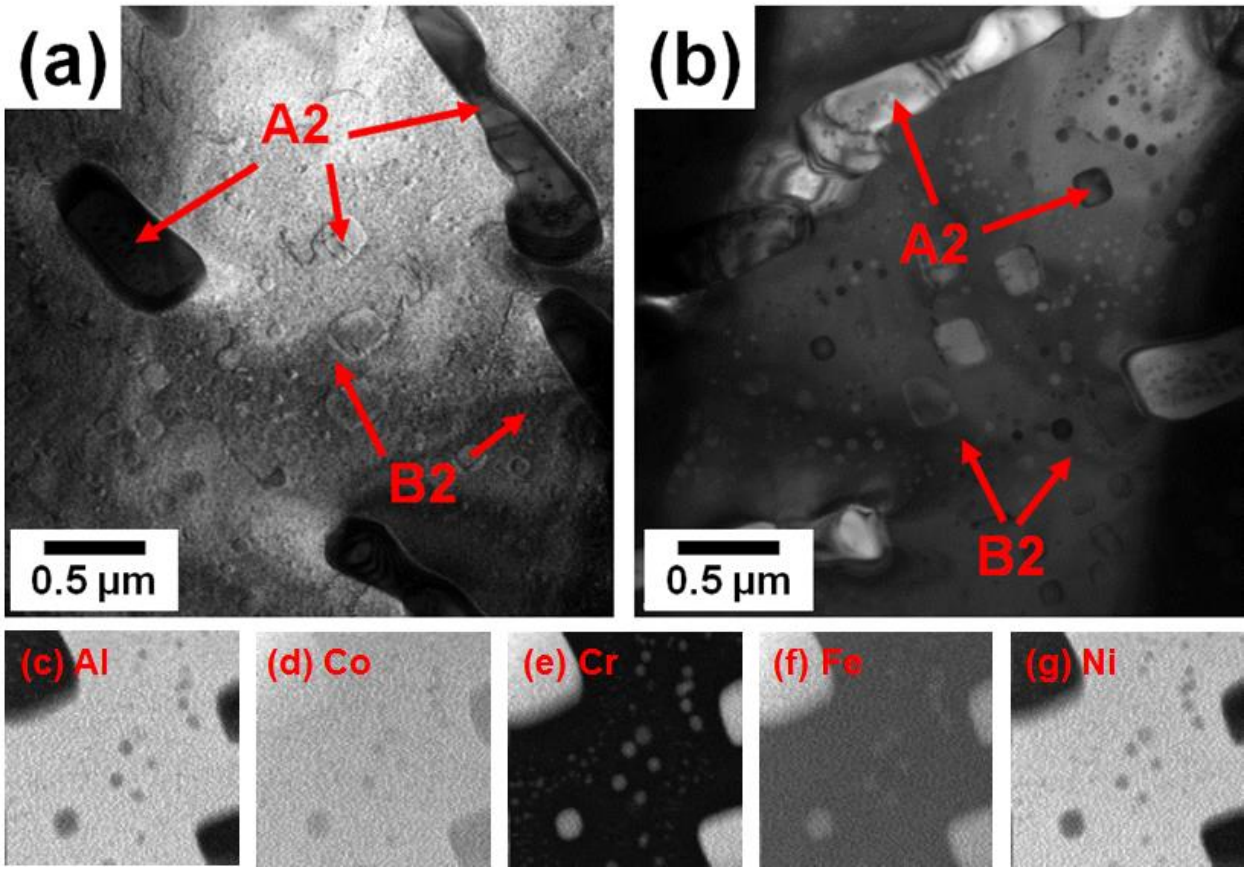

Figure 38. Bright-field (a) and dark-field (b) TEM images of the AlCoCrFeNi-HP alloy. Simultaneously-acquired STEM-EDS (c-g) X-ray maps of the microstructures of the AlCoCrFeNi-HP alloy confirm that the nanoprecipitates are enriched with Co, Cr, and Fe, while the matrix are enriched with Ni and Al.

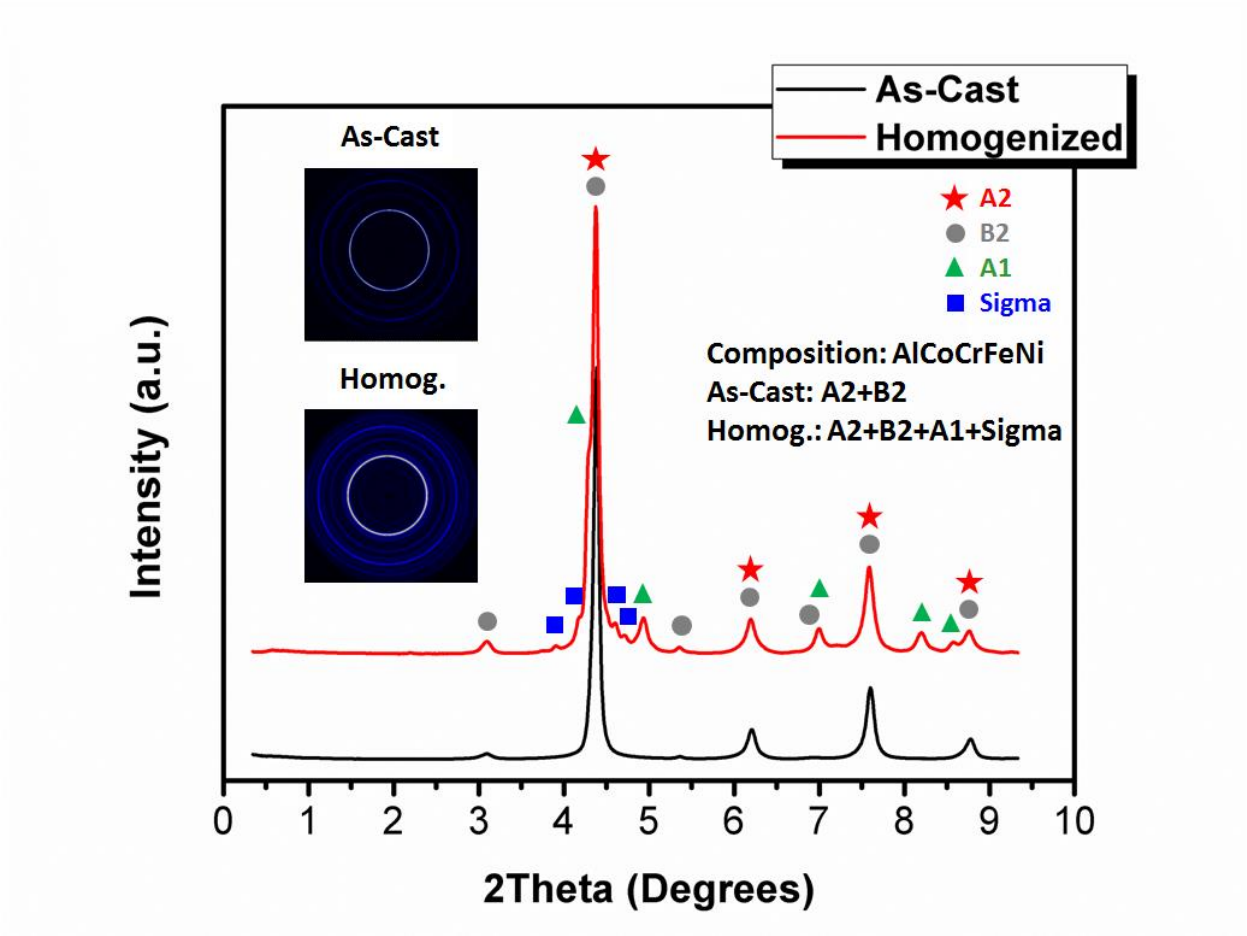

Figure 39. The high-energy synchrotron X-ray diffraction patterns of as-cast and homogenized conditions. The identified phases are shown in the legend. For the Sigma (σ) phase, the following lattice parameters were used: a = 8.800 Å, c = 4.544 Å. Two insets show the diffraction rings for as-cast and homogenized conditions, corresponding to the synchrotron X-ray diffraction pattern.

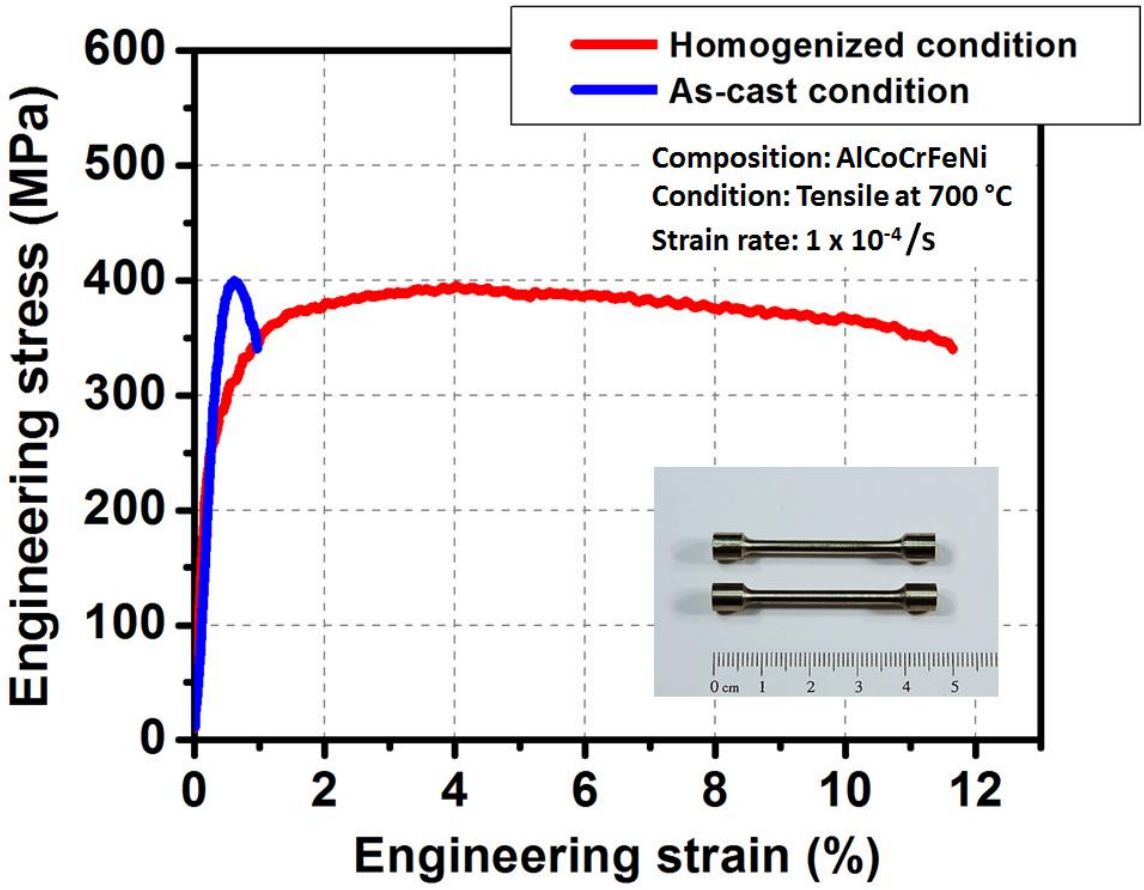

Figure 40. The tensile engineering stress-strain curves of the AlCoCrFeNi alloy, both in as-cast (AlCoCrFeNi-AC) and homogenized (AlCoCrFeNi-HP) conditions, at the temperature of 700 ℃. The inserted figure illustrates the cylindrical dog-boned sub-size specimens for tensile tests.

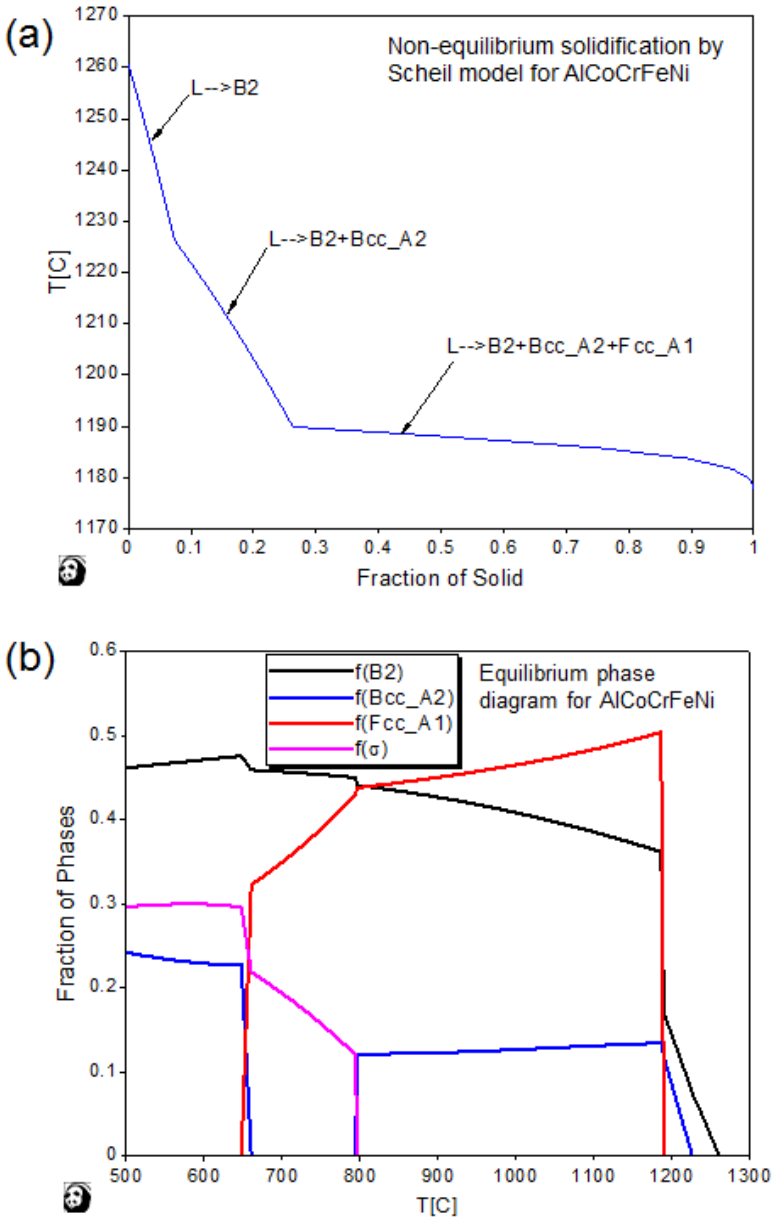

Figure 41. Thermodynamics modeling of (a) non-equilibrium solidification (fast cooling) by Scheil model [112] and (b) an equilibrium phase diagram

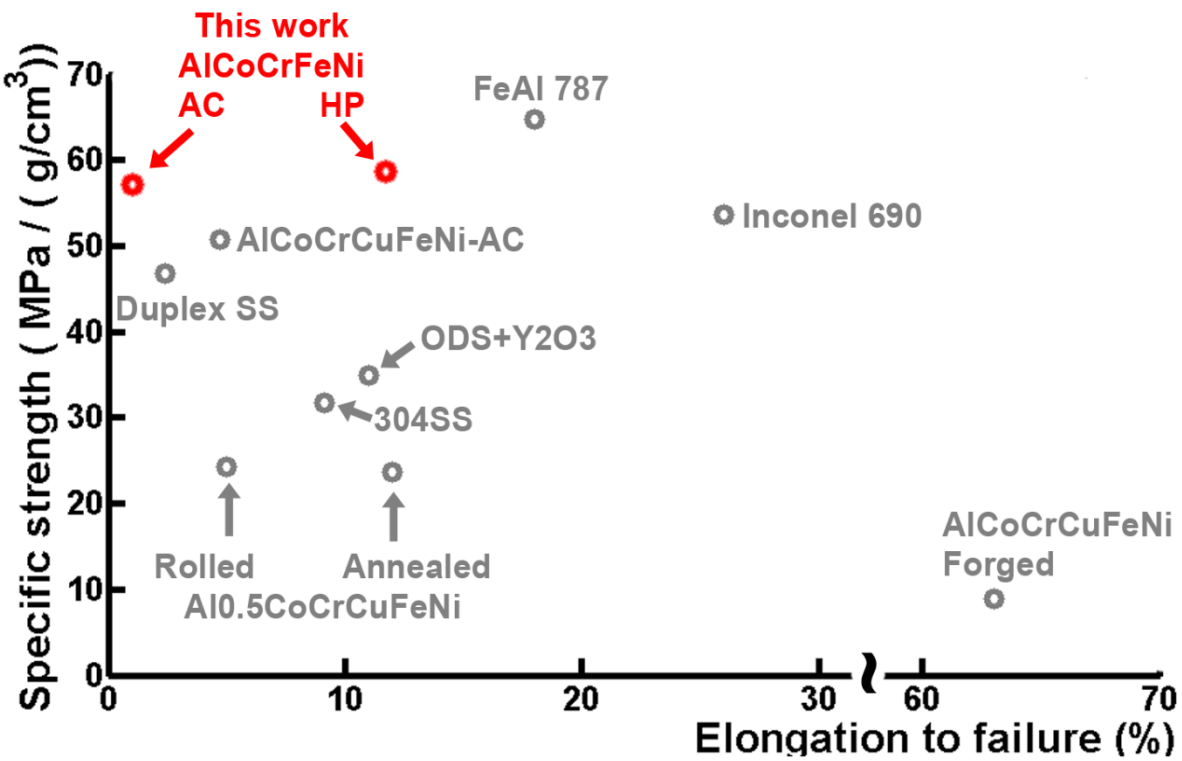

Figure 42. A scatter plot showing the specific strengths and elongations to failure of the AlCoCrFeNi-AC and AlCoCrFeNi-HP, and other high-temperature structural materials at 700 ℃ [35, 39, 159-167]. Compared to conventional structural alloys, the AlCoCrFeNi-HP has a comparable combination of mechanical properties at elevated temperatures

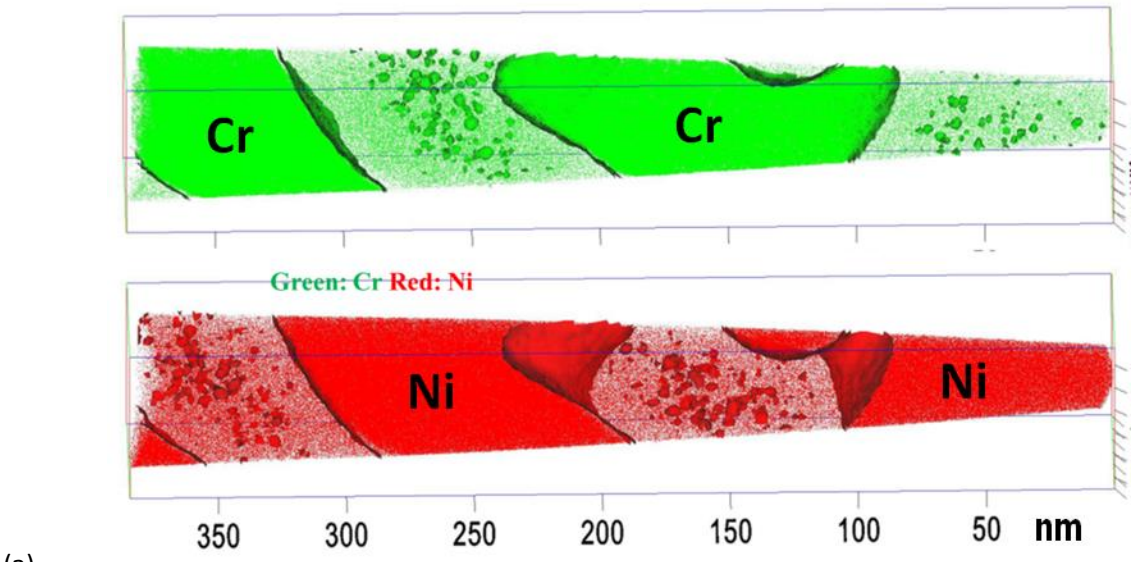

(a)

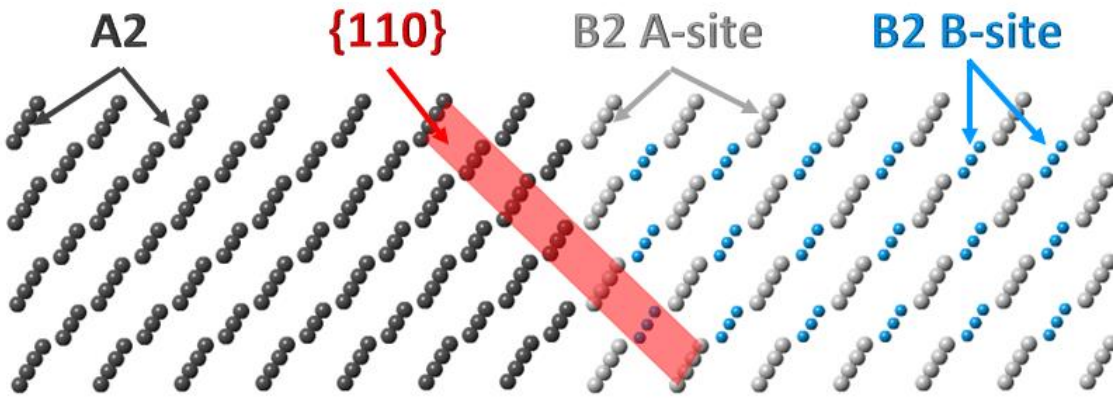

(b)

Figure 43. (a) Atom probe tomography (APT) of the AlCoCrFeNi-AC alloy, and (b) corresponding sketch of different atom clusters, such as A2 and B2

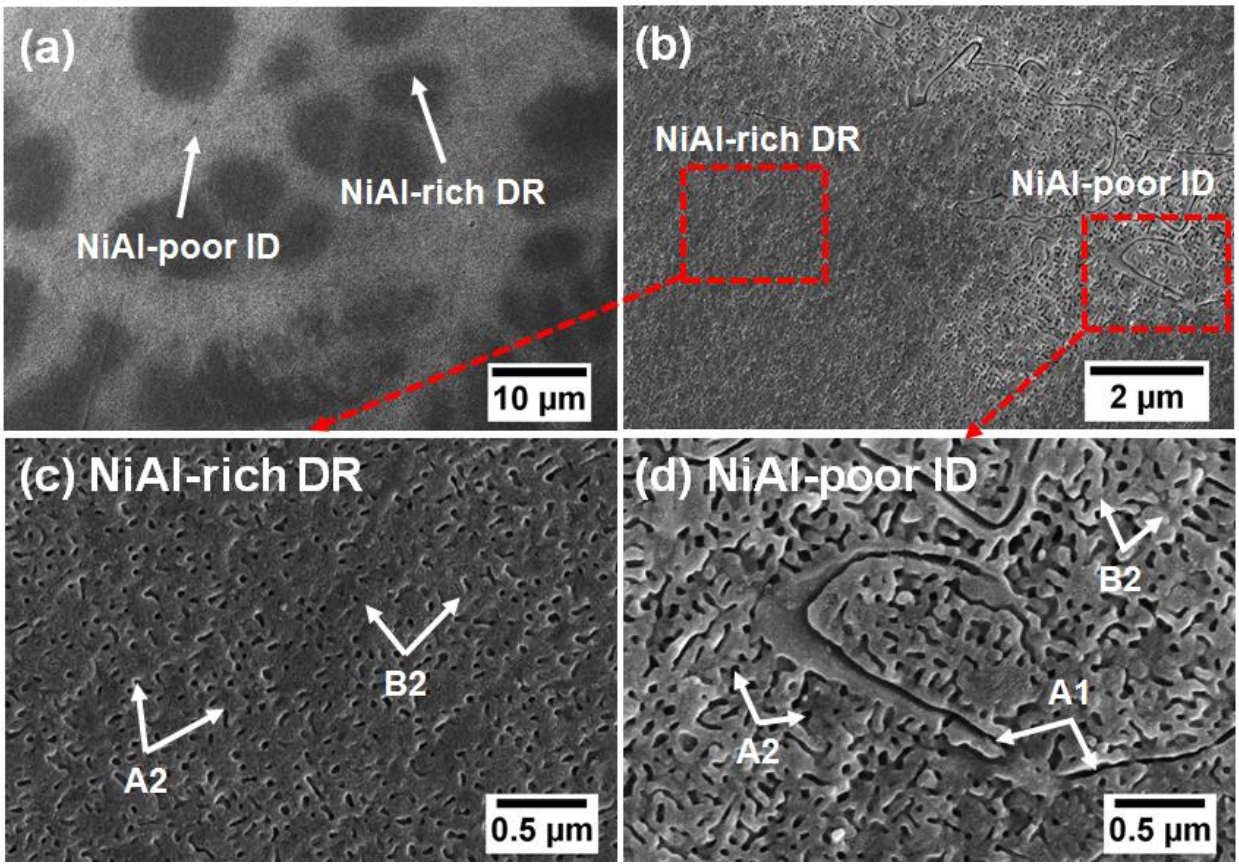

Figure 44. SEM images of the AlCoCrFeNi-AC alloy after applying selected etching using Kalling's No. 2.

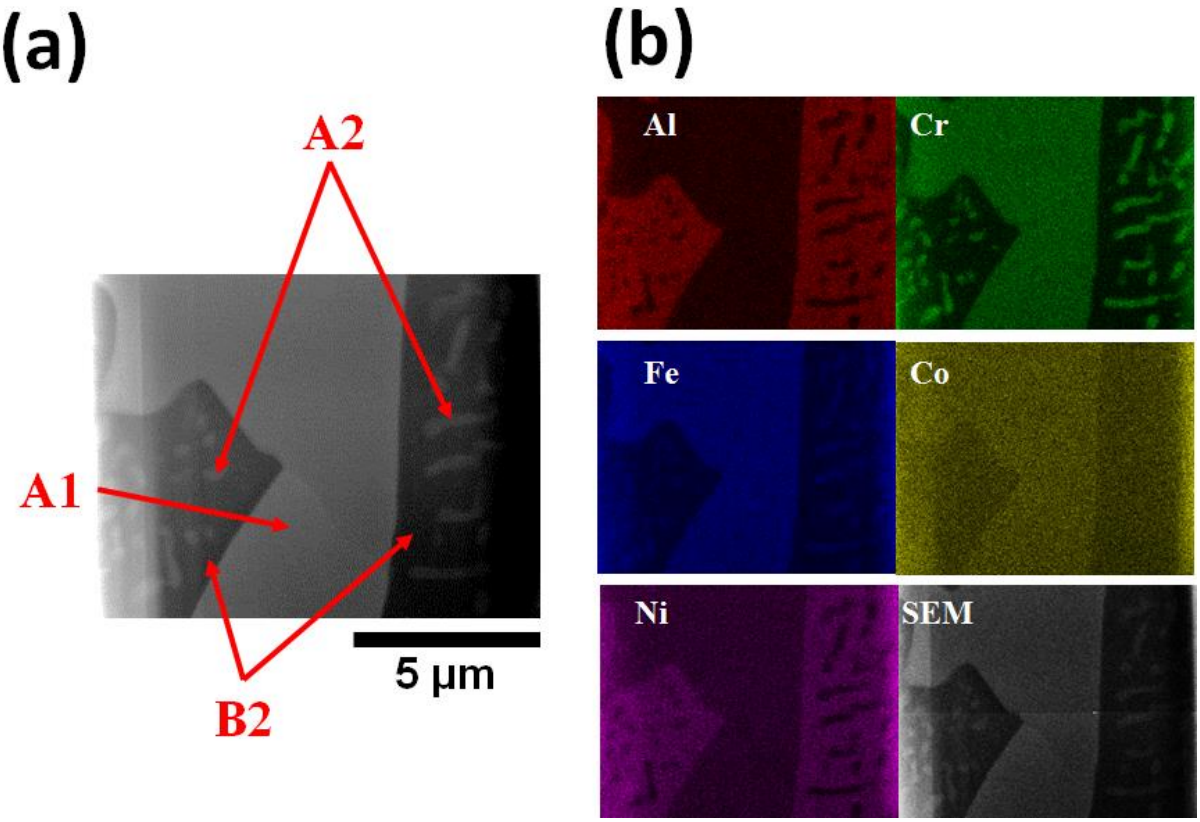

Figure 45. A high-resolution SEM image of a focused ion beam (FIB) sample in the AlCoCrFeNi-HP alloy. The EDS maps are presented in (b).

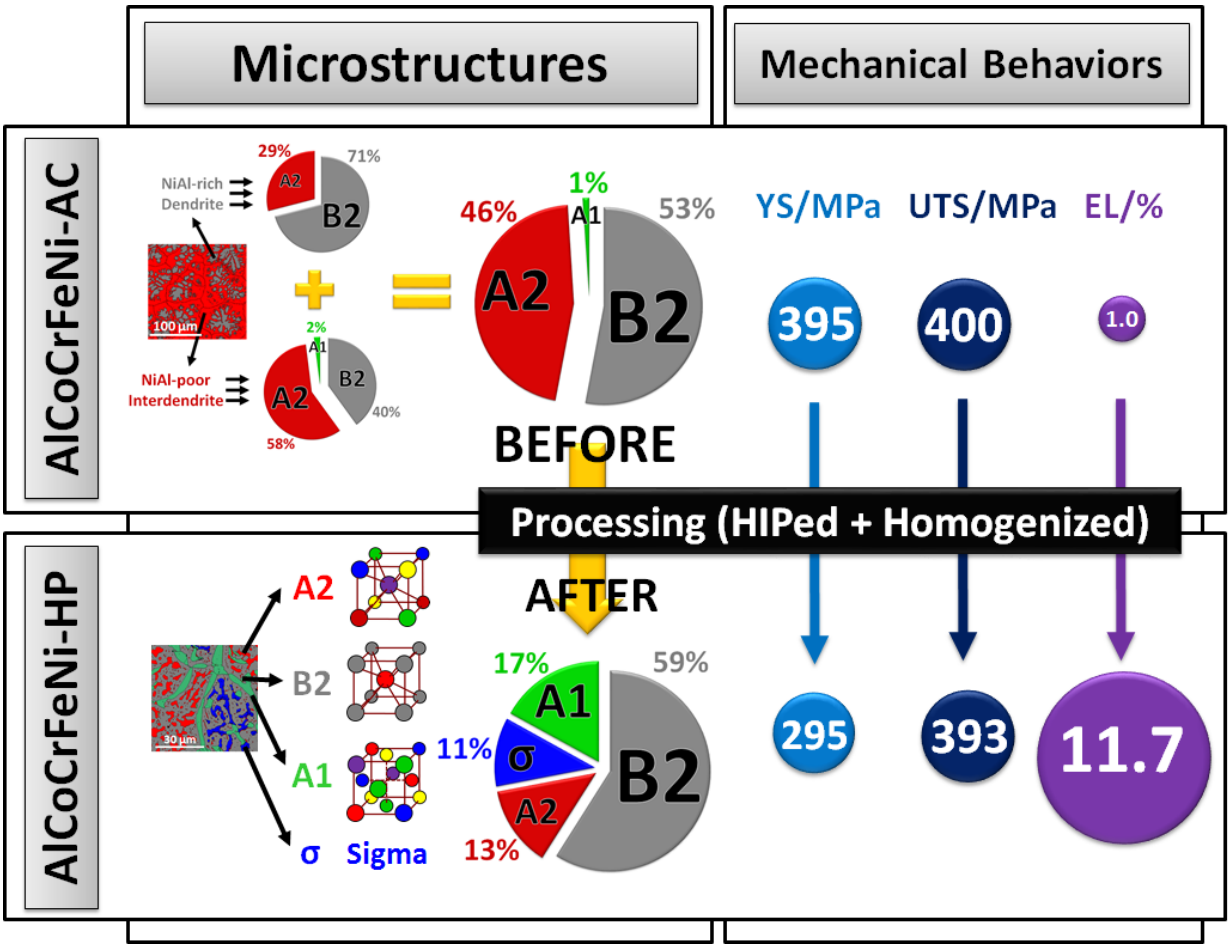

Figure 46. A summary cartoon of all major results in the present study

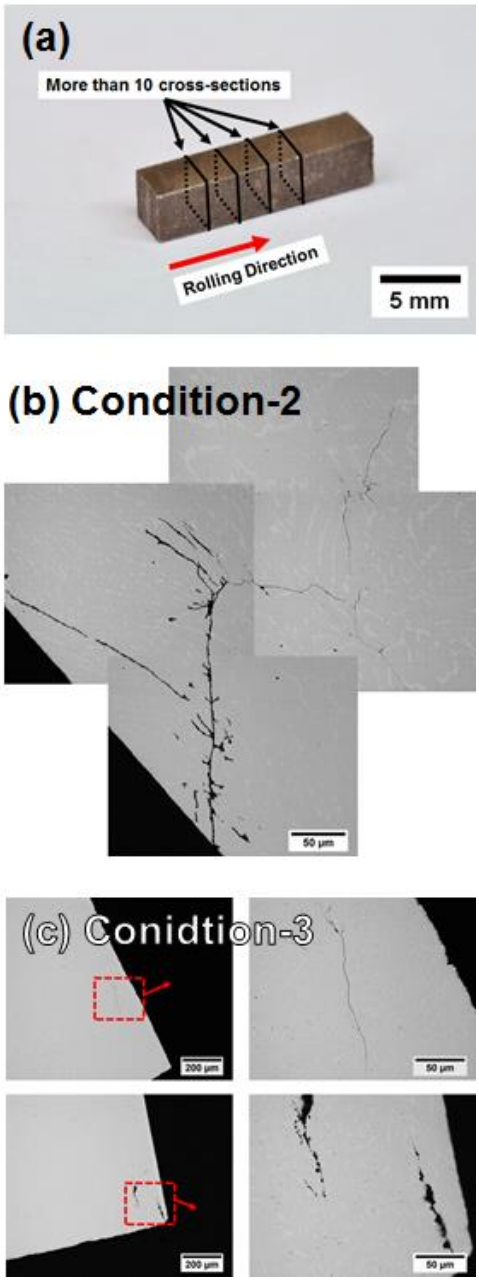

Figure 47. (a) A macrograph showing cross-sectional examination conducted in the as-received condition (before fatigue testing), and preexisting cracks in (b) Condition-2 and (c) Condition-3, examined by optical microscopy.

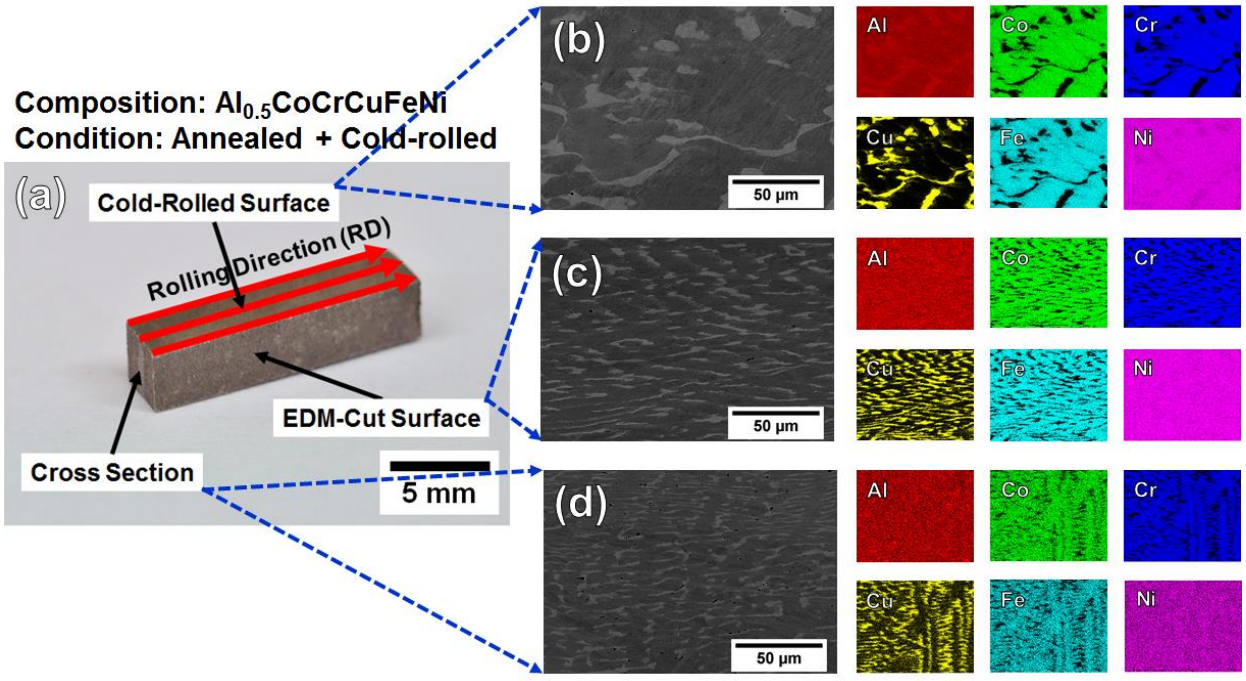

Figure 48. Macrograph (a) of a Condition-3 cold-rolled $Al_{0.5}CoCrCuFeNi$ HEA and micrographs of three sides [(b) cold-rolled surface, (c) Electric-Discharge-Machining (EDM) cut surface, and (d) cross section] with SEM-EDS elemental mapping of six principal elements, including Al (red), Co (green), Cr (blue), Cu (yellow), Fe (cyan), and Ni (magenta)

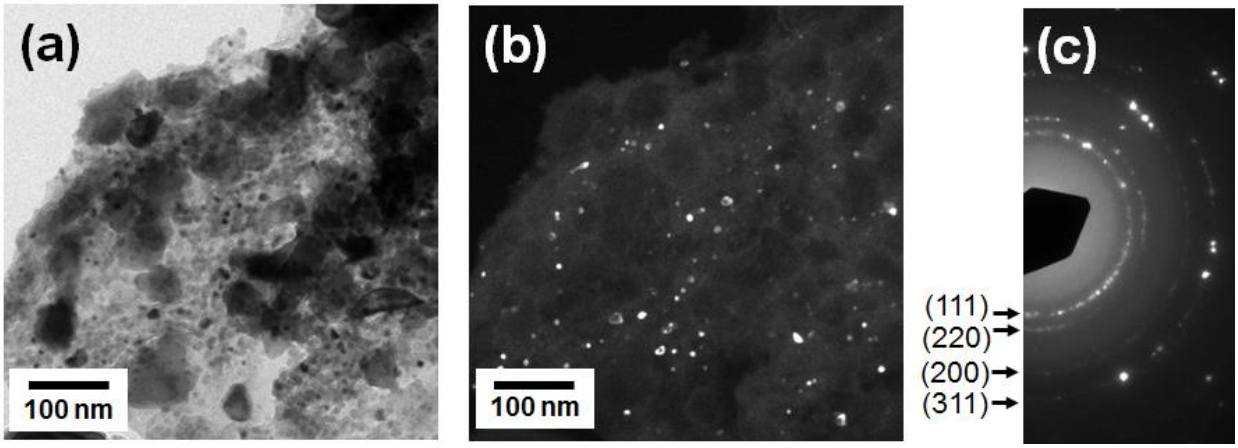

Figure 49. Bright-field TEM image (a) and dark-field TEM image (b) show that the Cu-rich phase has a nanostructure with nano-grain size of 5-10 nm. The diffraction pattern (c) confirms that the phase is FCC.

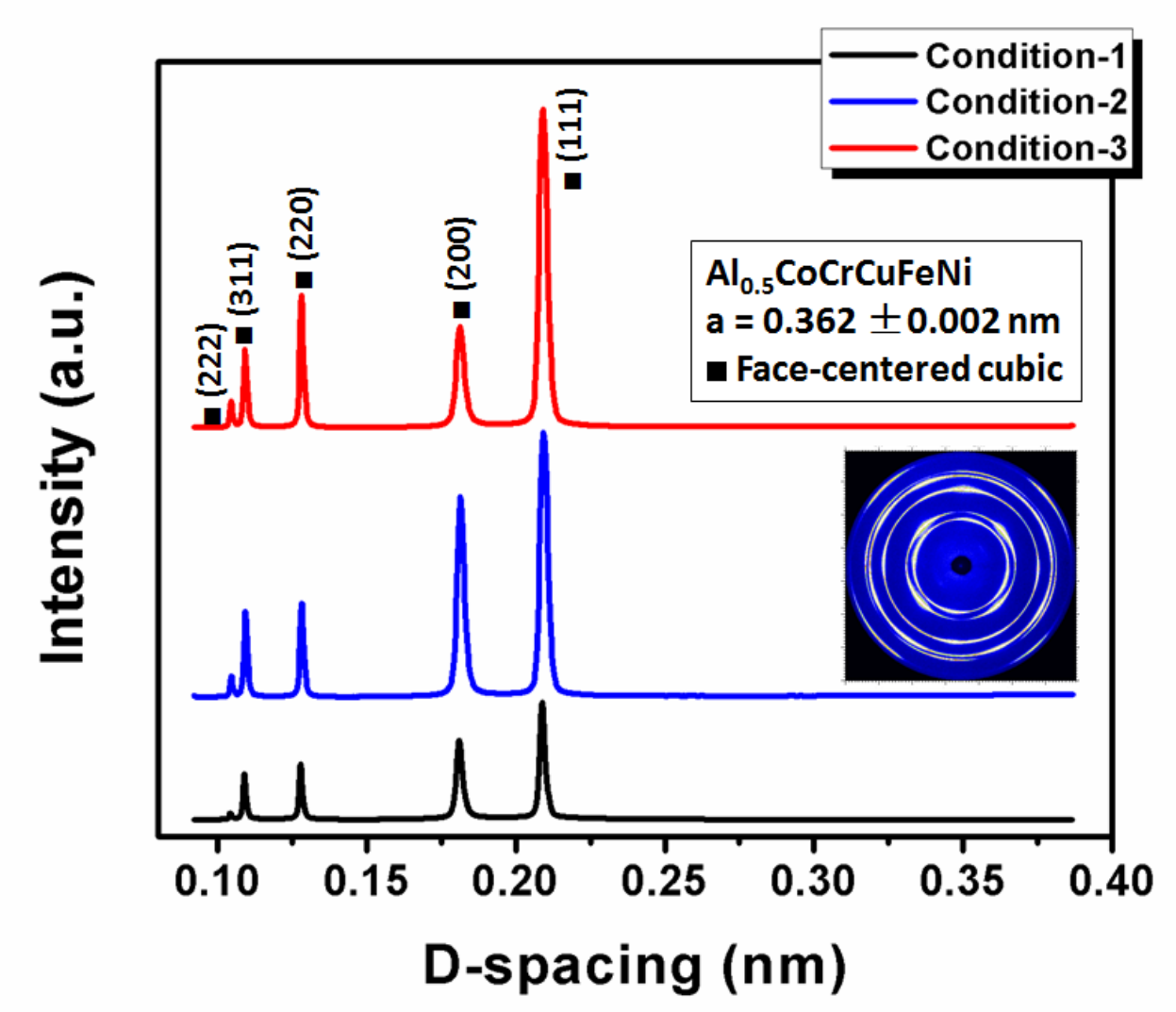

Figure 50. Synchrotron X-ray line profiles of three $Al_{0.5}$CoCrCuFeNi conditions. HEA specimens show FCC structures with a lattice parameter of 0.362 ±0.002 nm. The inserted Synchrotron 2-D diffraction pattern indicates a texture in the sample. The results of the Condition-1 from literature [7].

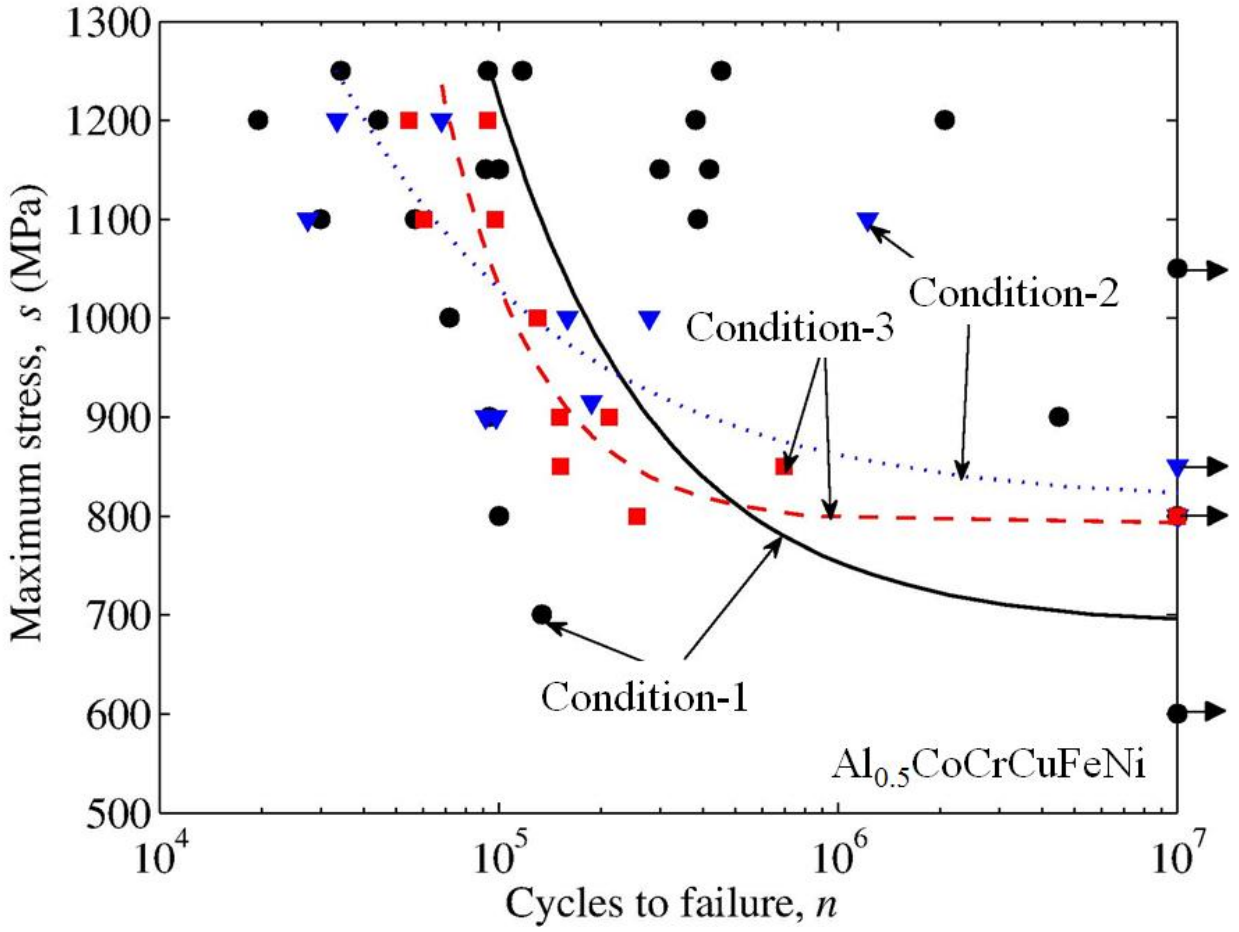

Figure 51. The S-N curves of $Al_{0.5}CoCrCuFeNi$ HEA under high-cycle four-point-bending fatigue with an R ratio of 0.1 in air at room temperature are shown. Note that the arrow indicates a run-out without failure. The dashed line shows modeling-predicted median fatigue life vs. stress relationship for the three conditions of HEAs.

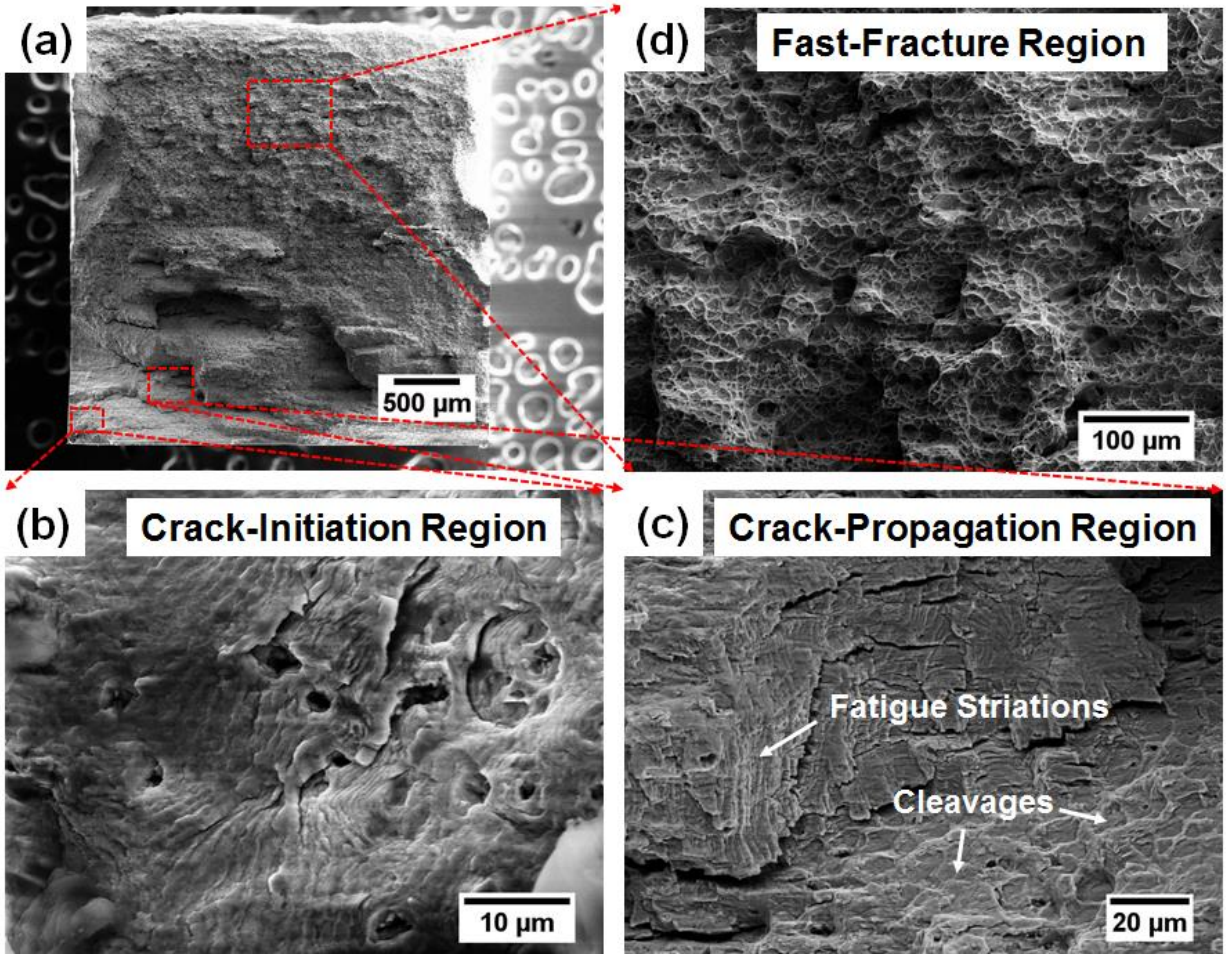

Figure 52. Fracture morphologies of a Condition-3 $Al_{0.5}CoCrCuFeNi$ specimen failed at a maximum stress of 1,100 MPa, R = 0.1, room temperature, in air, fatigue life of 97,715 cycles, and 10 Hz: (a) overview, (b) crack-initiation region with a mixed morphology of fatigue striations and pores, (c) crack-propagation region with fatigue striations and cleavages, and (d) fast-fracture region with dimples

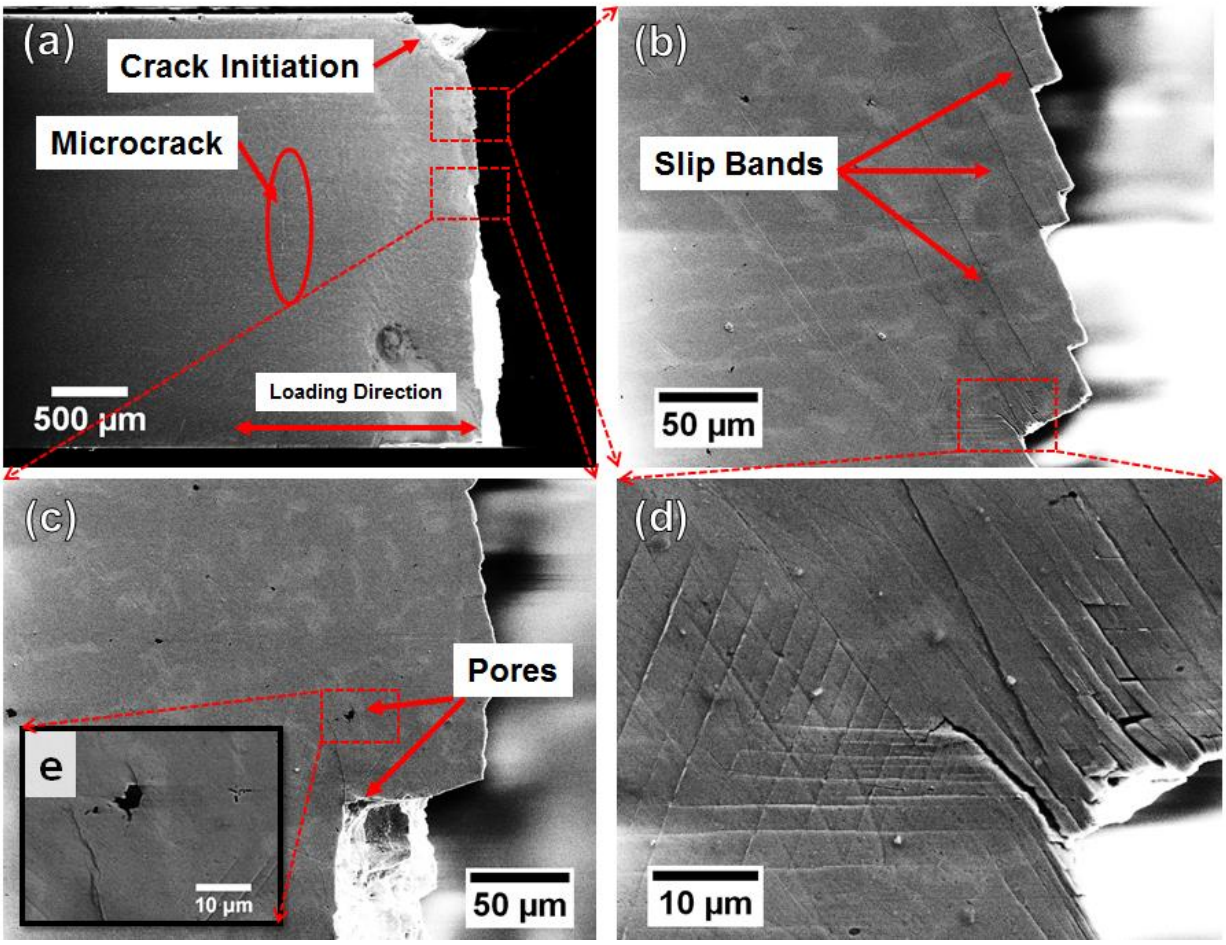

Figure 53. The tensile-stress surface of a Condition-3 $Al_{0.5}CoCrCuFeNi$ specimen failed at a maximum stress of 1,100 MPa, R = 0.1, room temperature, in air, fatigue life of 97,715 cycles, and 10 Hz: (a) overview of the tensile-stress surface; (b) high magnification of (a) showing slip bands; (c) high magnification of (a) showing shrinkage pores; (d) high magnification of (b); (e) high magnification of (c).

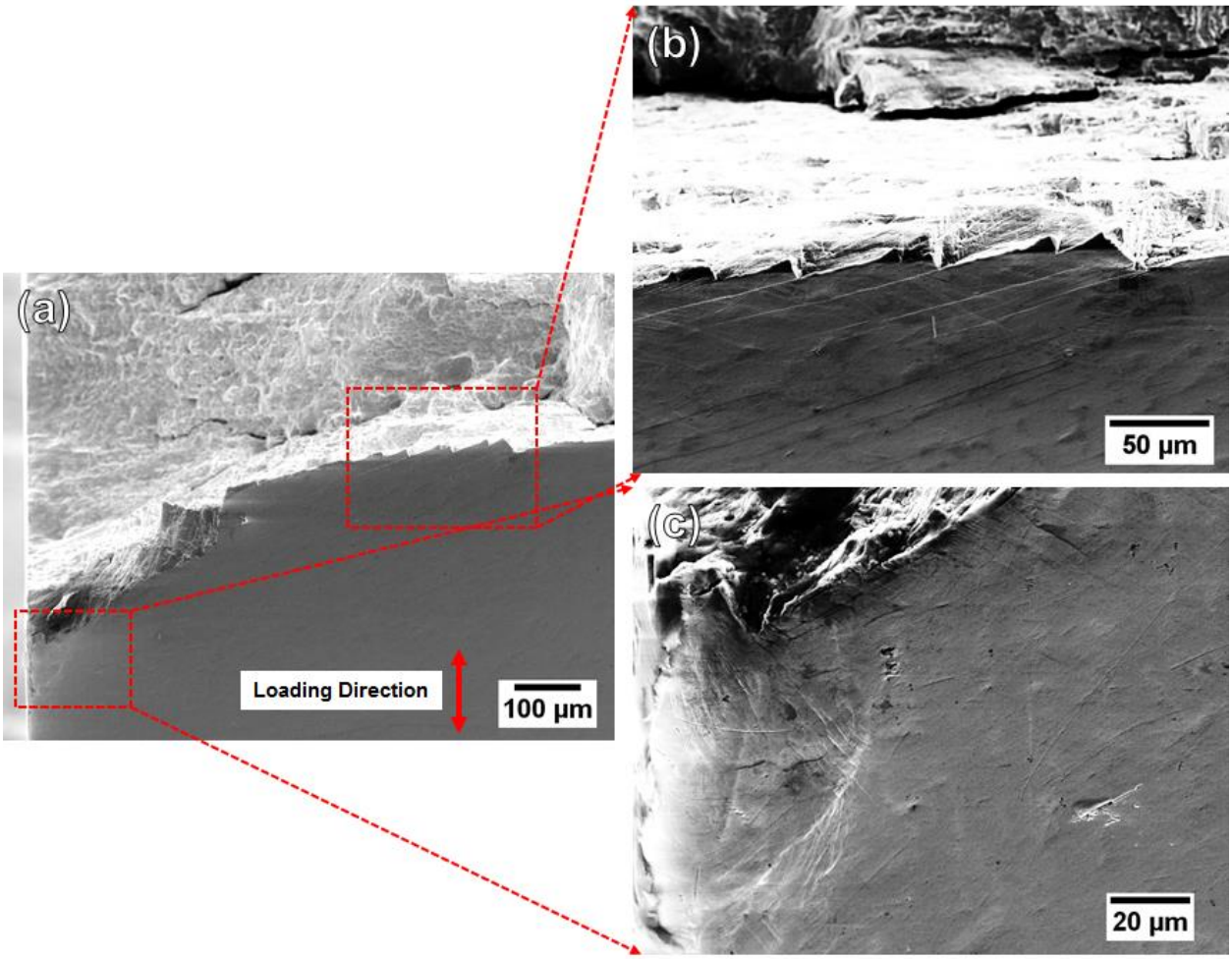

Figure 54. Crack initiation of a Condition-3 $Al_{0.5}CoCrCuFeNi$ specimen failed at a maximum stress of 1,100 MPa, R = 0.1, room temperature, in air, fatigue life of 97,715 cycles, and 10 Hz: (a) overview of a crack-initiation region; (b) high magnification of (a) showing slip bands; (c) high magnification of (a) showing extensive plastic deformation

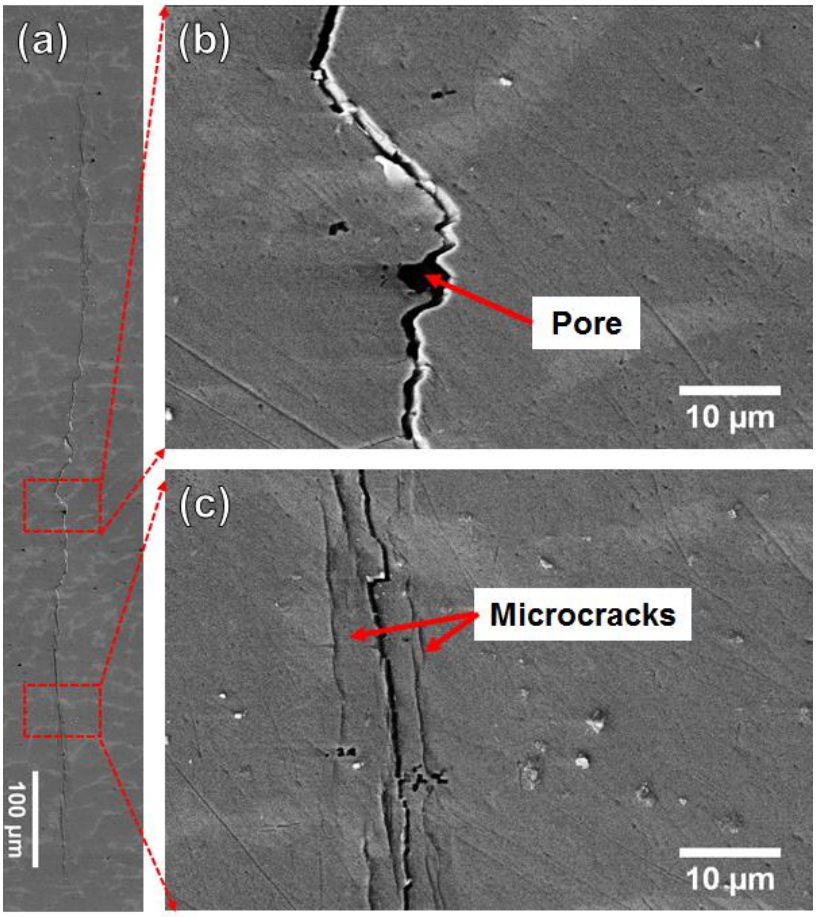

Figure 55. High magnification of a microcrack (a) in Figure 53a on the tensile stress surface of the $Al_{0.5}CoCrCuFeNi$ HEA sample after four-point-bending fatigue: (b) high magnification of (a) showing a pore; (c) high magnification of (a) showing microcracks

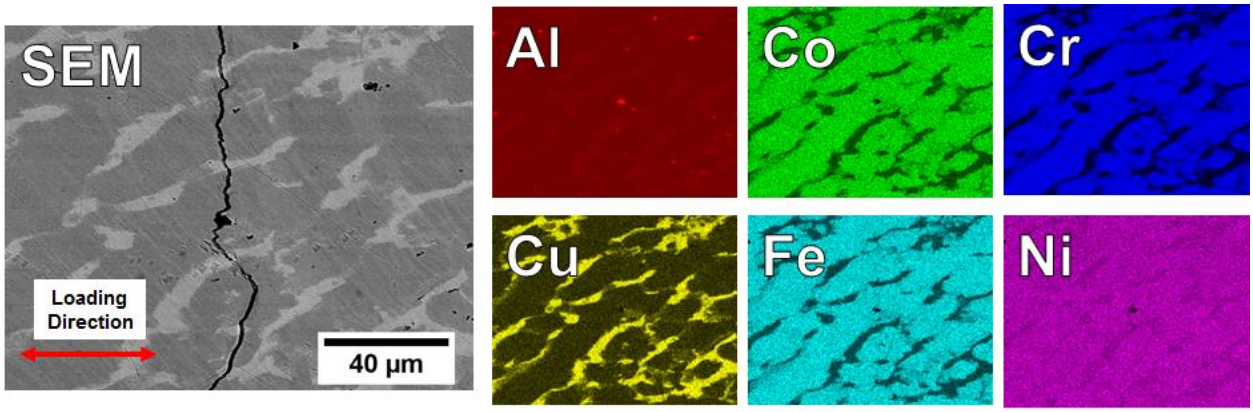

Figure 56. SEM images with EDS elemental mapping of six principal elements, including Al (red), Co (green), Cr (blue), Cu (yellow), Fe (cyan), and Ni (magenta)

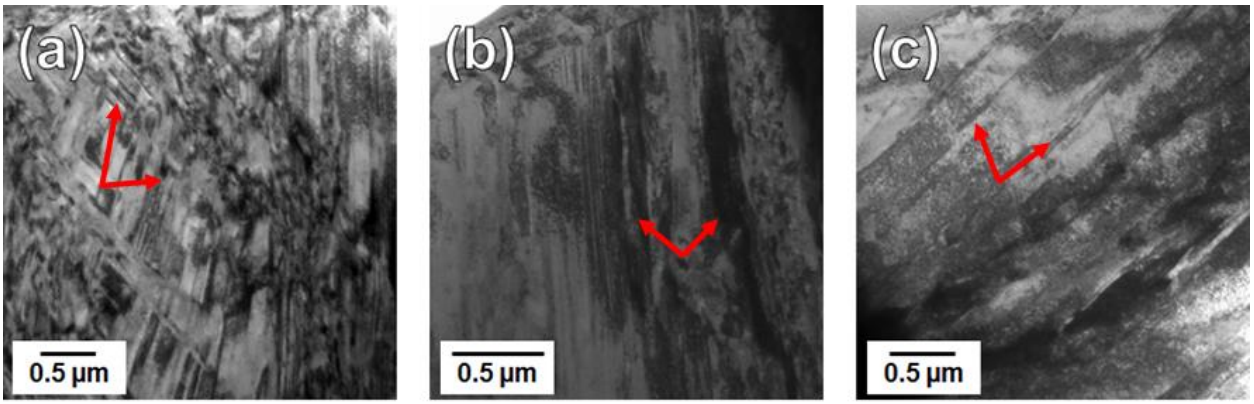

Figure 57. TEM-FIB images removed from a fatigue-failed specimen with a lifetime of 2,069,447 cycles at 1,200 MPa in Condition-1 at three different locations, including (a) at the crack initiation site, (b) adjacent to the crack-initiation site, and (c) away from the crack initiation site. Tangled dislocations and nanotwins (indicated by arrows) coexist in the microstructure.

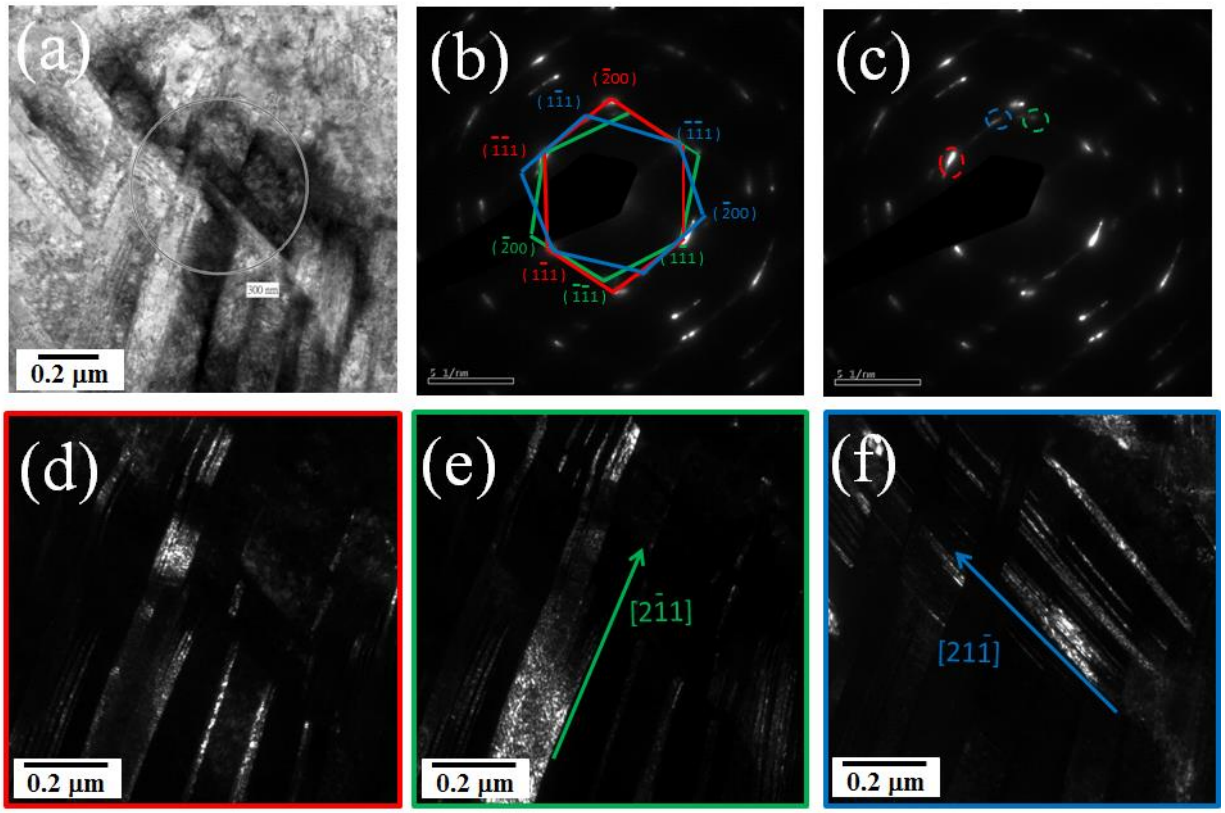

Figure 58. Two different-orientation sets of dense nanotwins with a high density of tangled dislocations (a) are clearly identified. Three sets of diffraction patterns with zone axis [011] (b), matrix and two orinetaions of twins, are indicated. Three chosen spots (c) for dark-field images are also indicated. Three dark-field images are the matrix in combination with first set of twins (red color) (d), first set of twins (green color) (e), and second set of twins (blue color) (f).

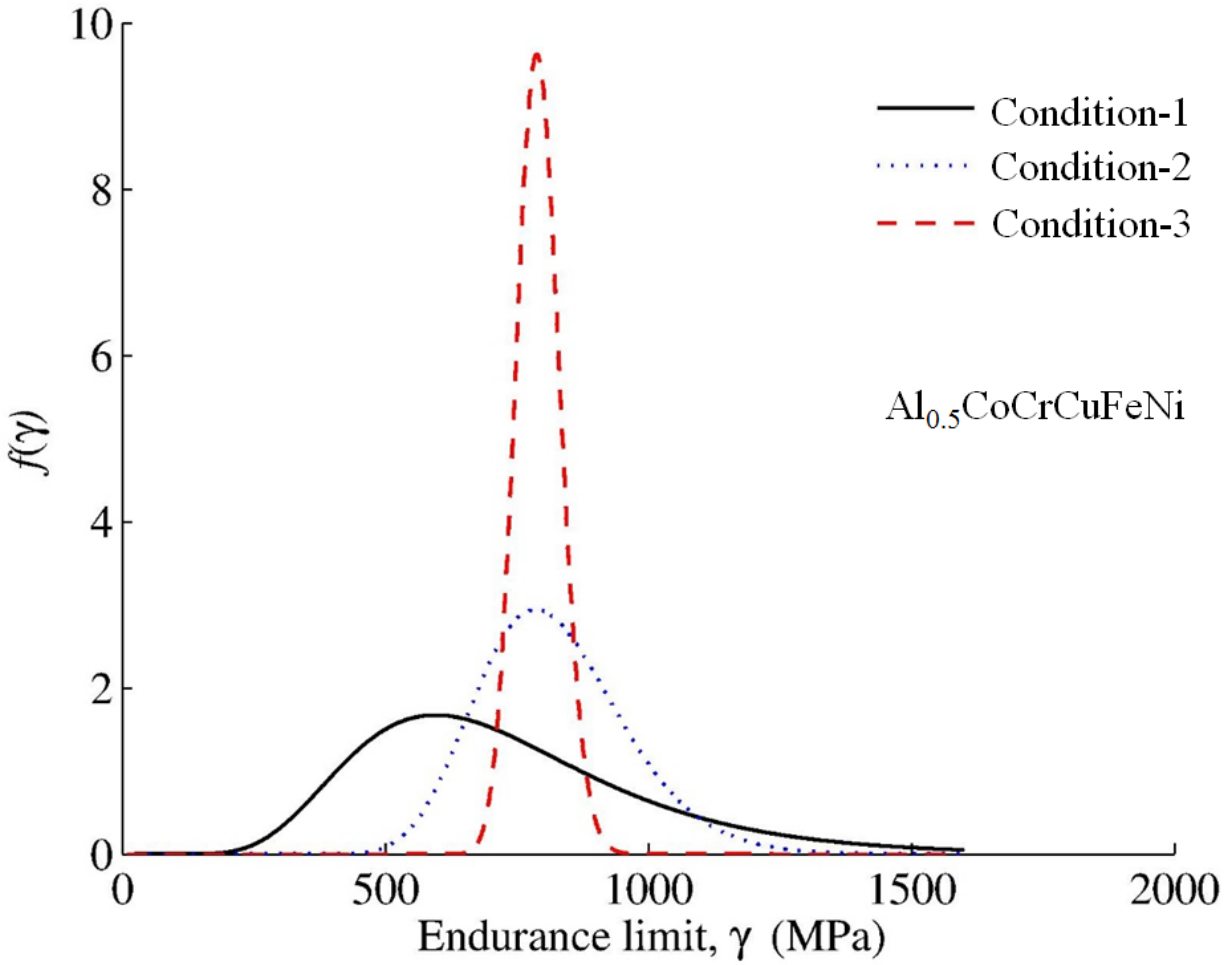

Figure 59. Probability distributions of the endurance limits for the three conditions of HEAs

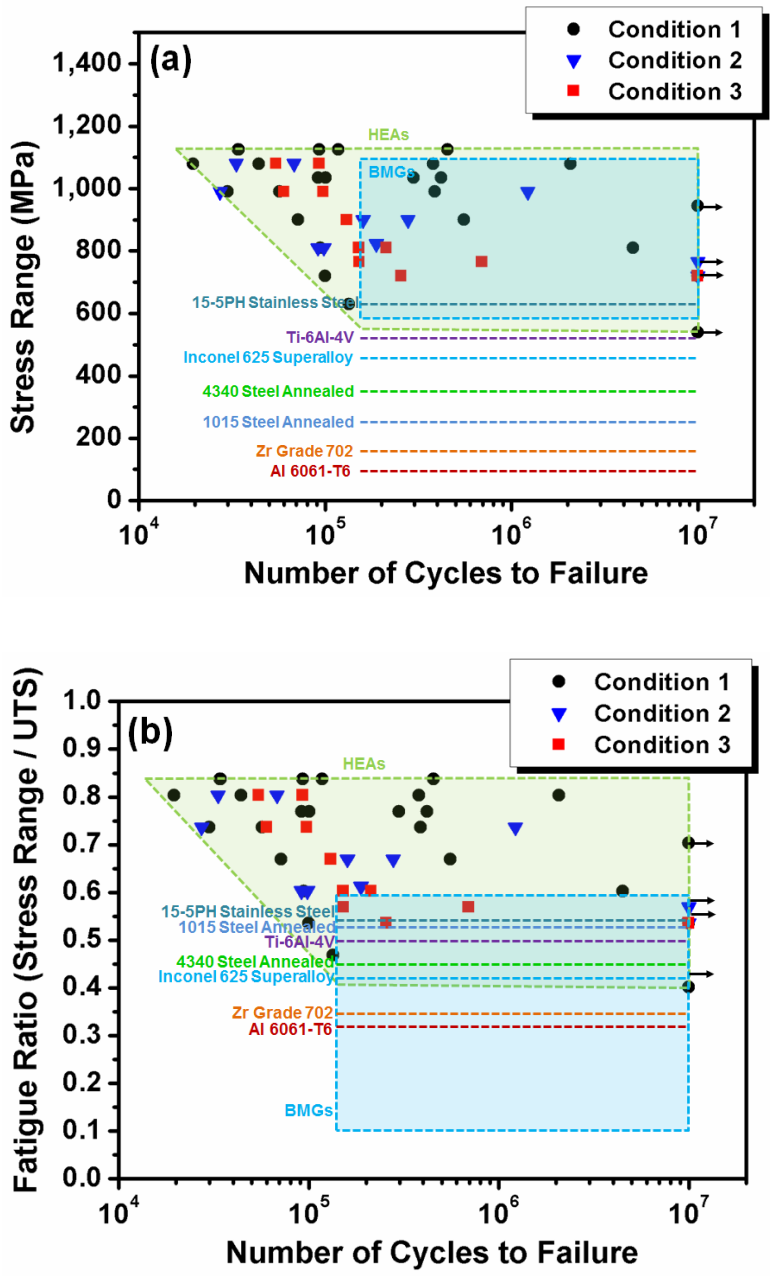

Figure 60. S-N curves comparing (a) the fatigue endurance limits at 10^7 cycles and (b) the fatigue ratios of the $Al_{0.5}CoCrCuFeNi$ HEA, other conventional alloys, and BMGs. Colored dashed lines denote the endurance limit of each alloy [7].

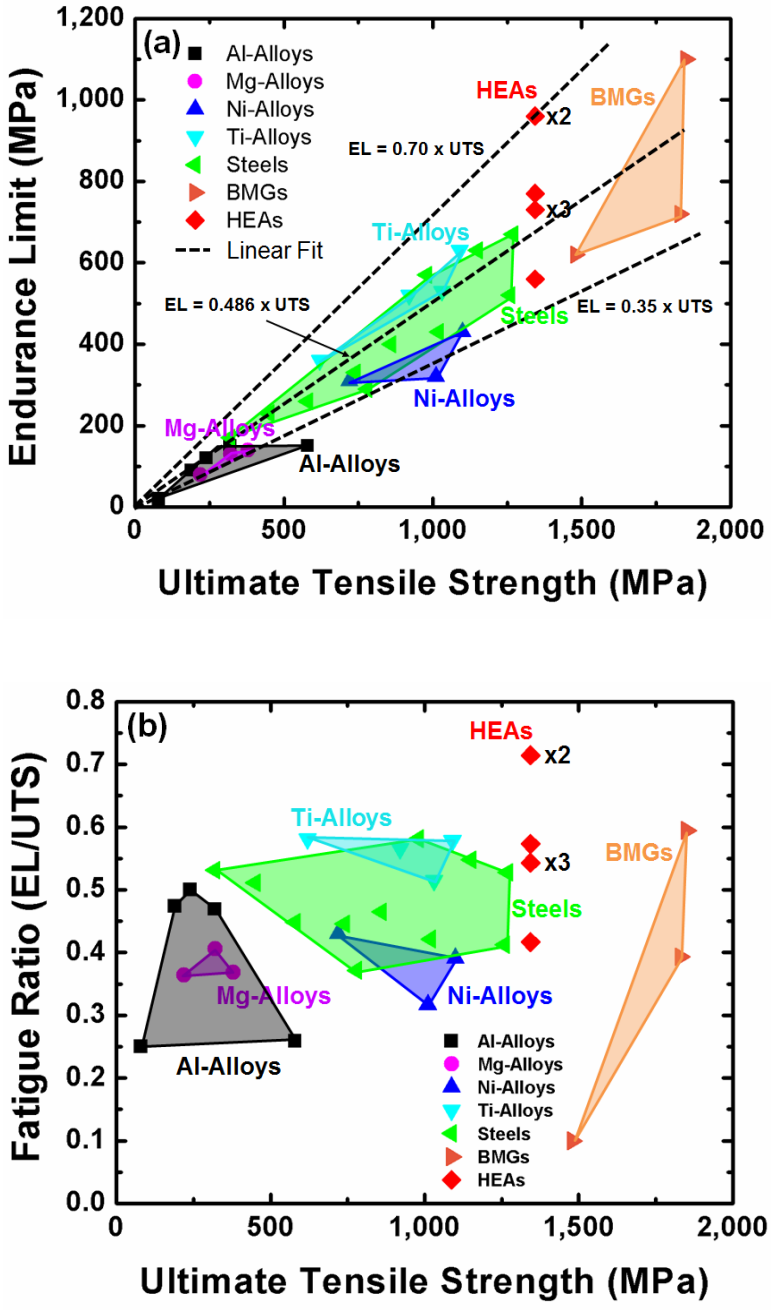

Figure 61. Plots comparing (a) the endurance limits and (b) the fatigue ratios of the $Al_{0.5}CoCrCuFeNi$ HEA as a function of the UTS of other structural materials and BMGs [7].

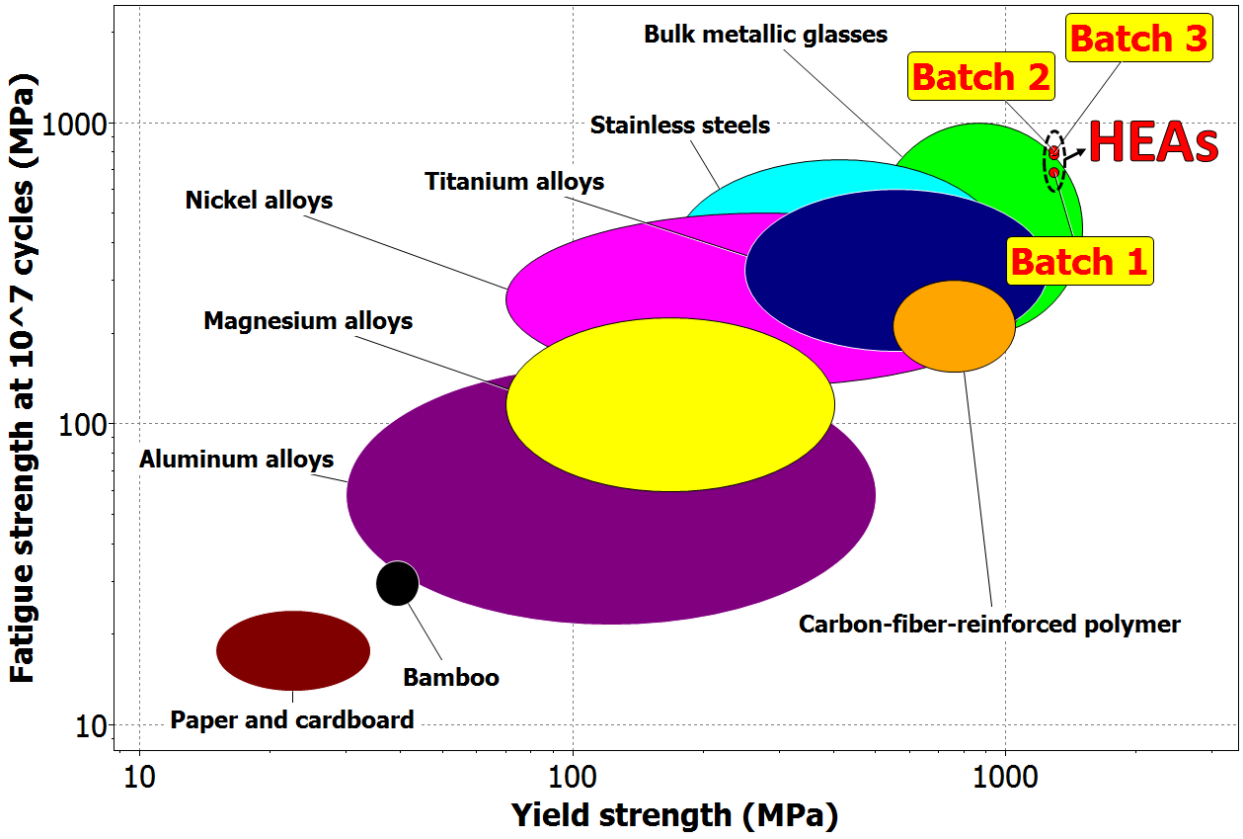

Figure 62. An Ashby map shows the range of fatigue strength at 10^7 cycles versus yield strength at room temperature for three conditions of HEAs and other materials. The black-dashed ellipse indicates the family of HEAs [22, 148]. HEAs have a better combination of mechanical properties of both fatigue and yield strengths, compared with conventional structural counterparts.

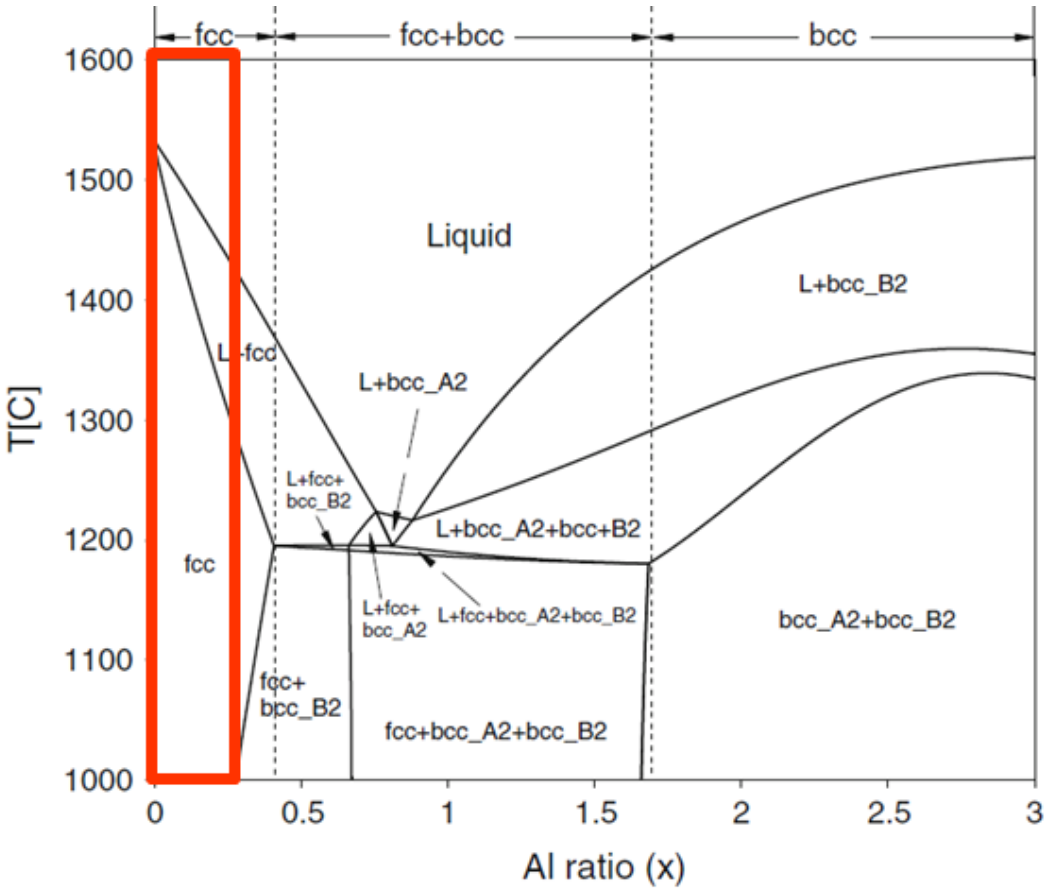

Figure 63. The calculated isopleth of the AlxCoCrFeNi alloys with x = 0 – 3 using the current thermodynamic description. Literature results from [57]

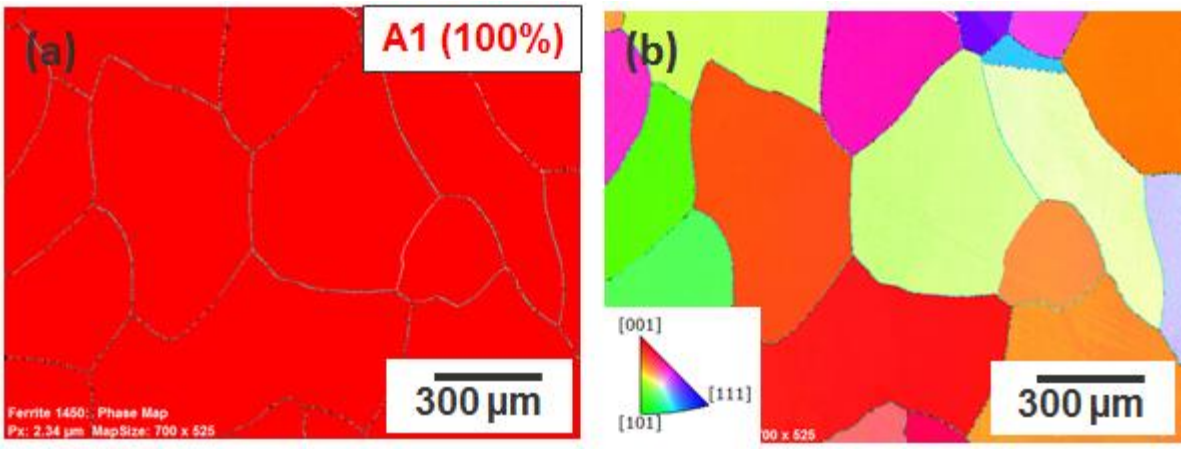

Figure 64. EBSD (a) phase map and (b) inverse pole figure map of the Al0.3CoCrFeNi alloy

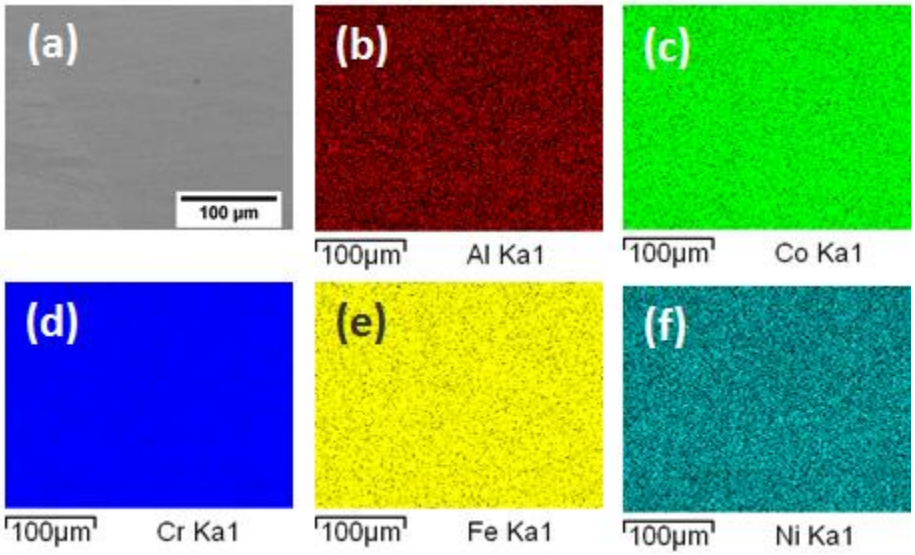

Figure 65. A back-scattered SEM image (a) and EDS X-ray maps (b-f) of the Al0.3CoCrFeNi alloy

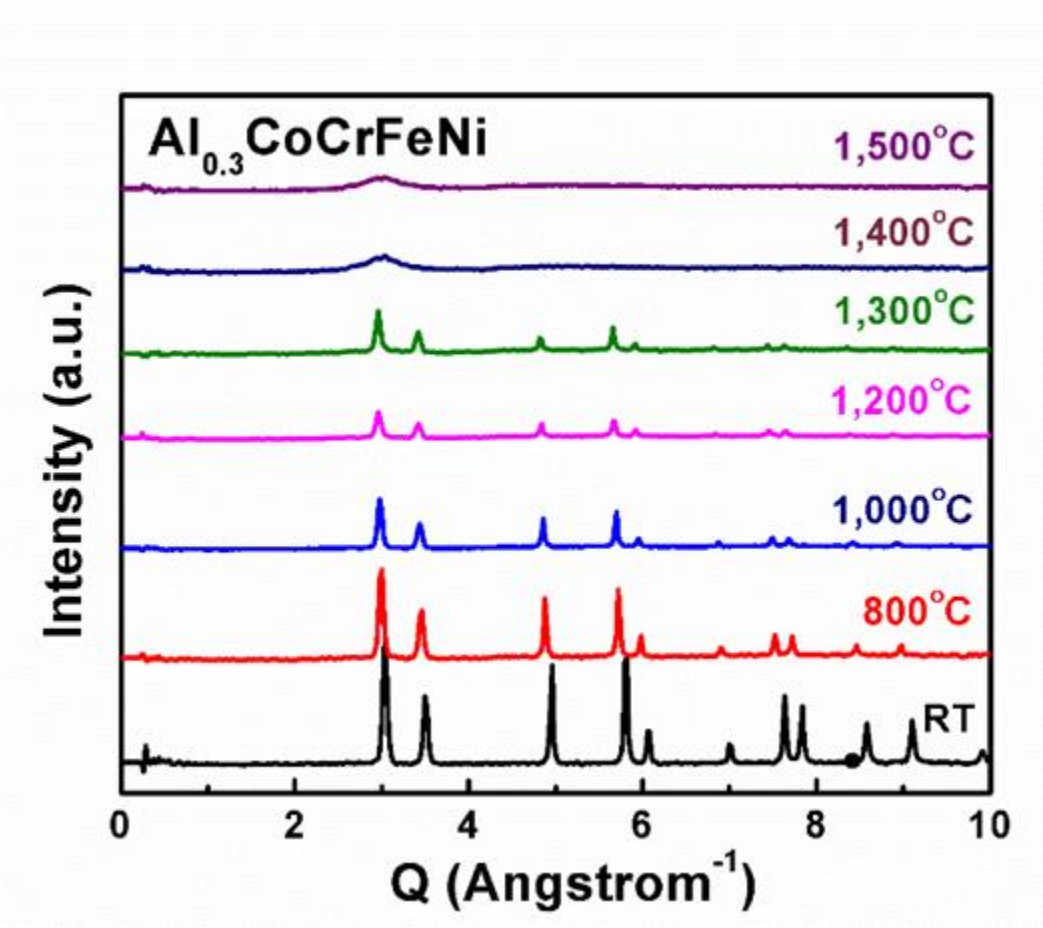

Figure 66. In-situ neutron diffraction of Al0.3CoCrFeNi

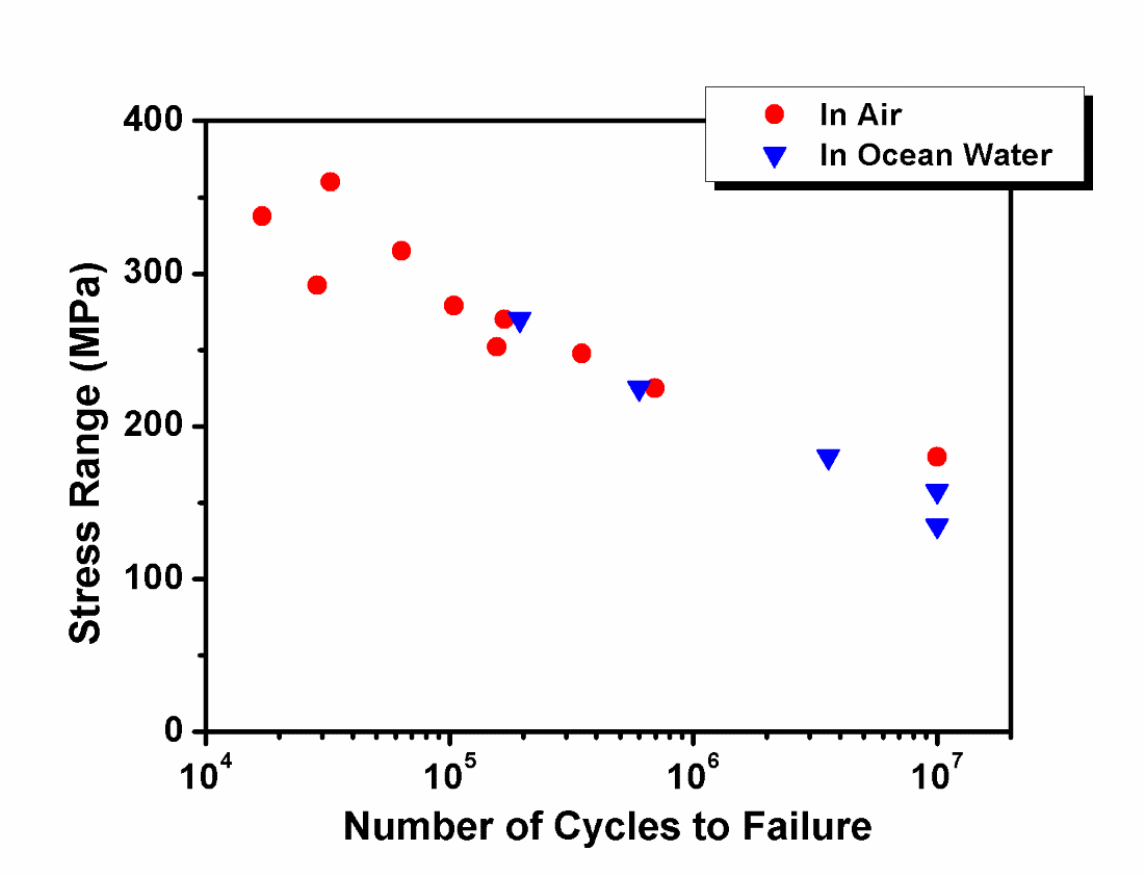

Figure 67. The stress-life (S-N) curve of Al0.3CoCrFeNi under tension-tension cyclic loading

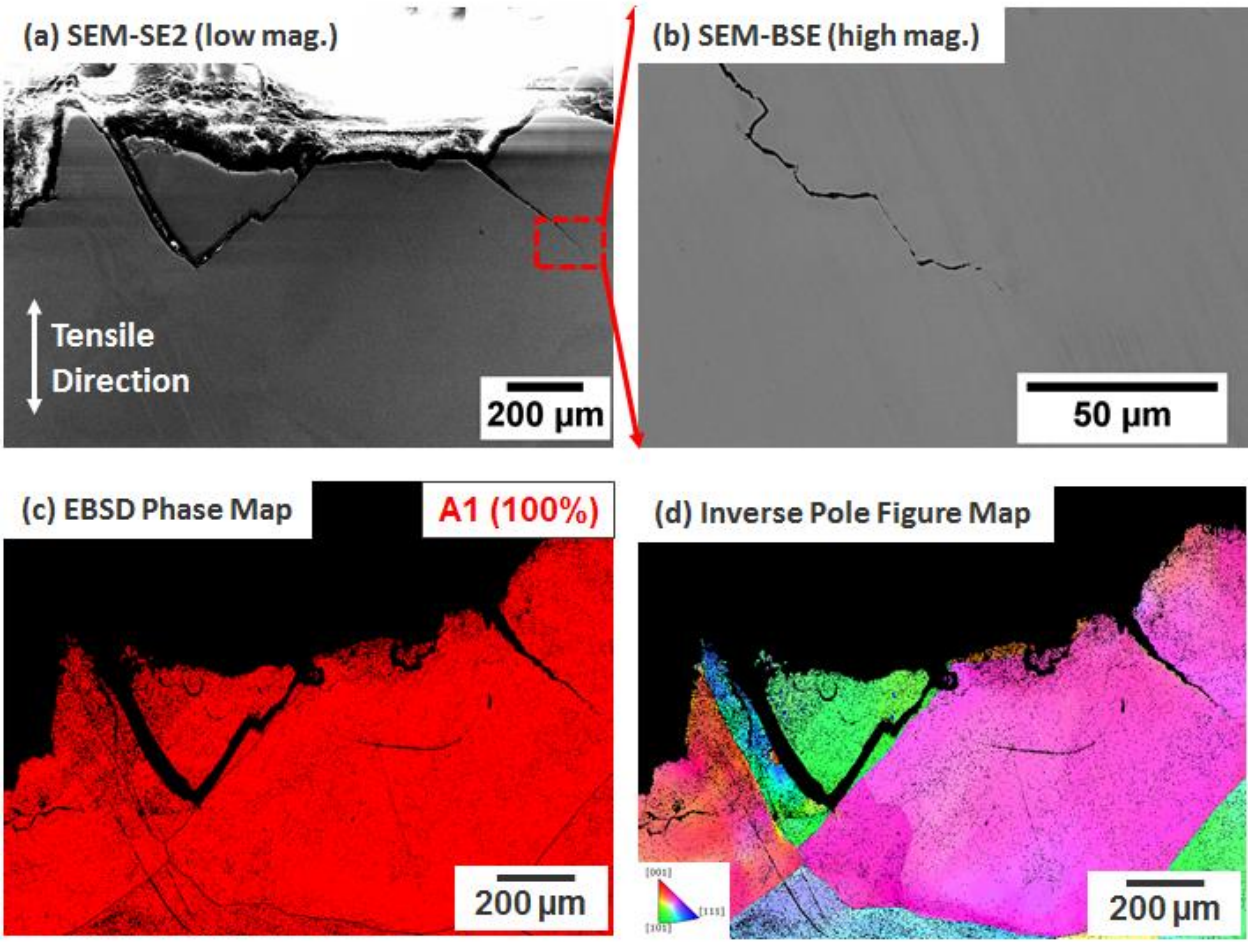

Figure 68. A longitudinal cross-sectional SEM and EBSD images below the fracture surface of the corrosion-fatigued Al0.3CoCrFeNi in the ocean water environment

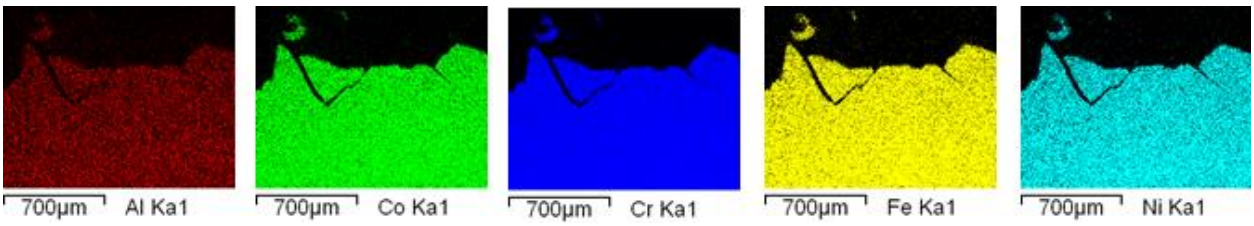

Figure 69. A longitudinal cross-sectional EDS X-ray maps below the fracture surface of the corrosion-fatigued Al0.3CoCrFeNi in the ocean water environment

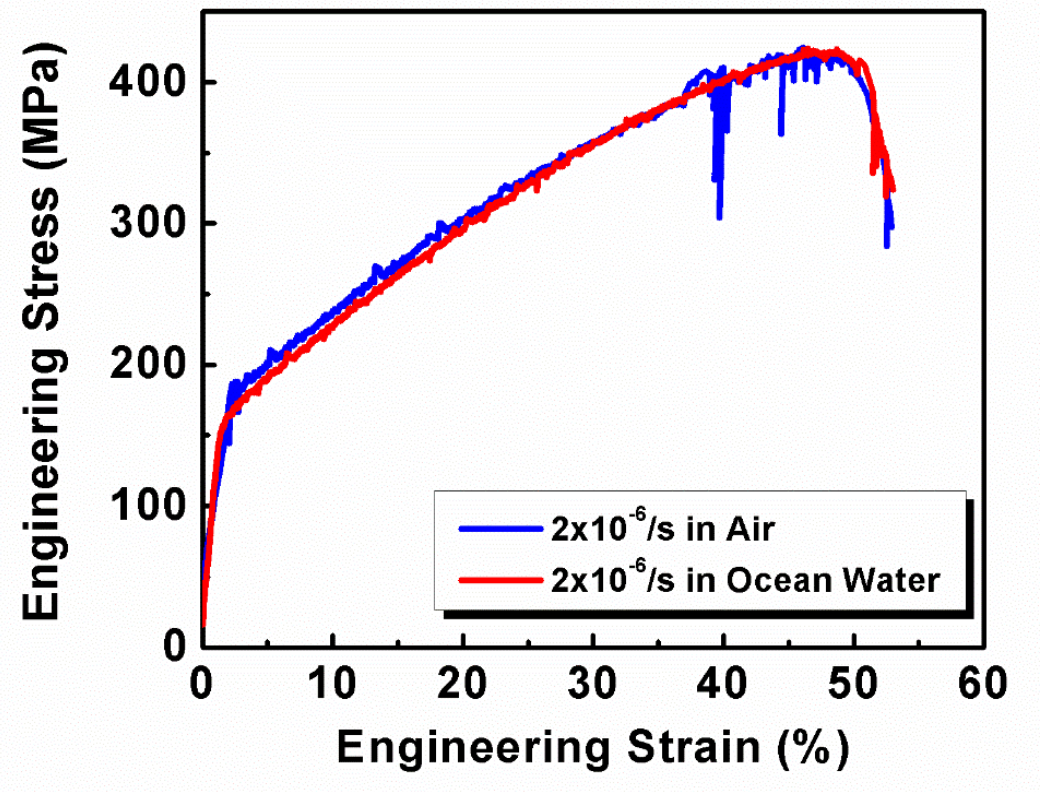

Figure 70. Slow strain rate testing of the Al0.3CoCrFeNi in air and ocean water at a strain rate of 2 x 10^{-6}/s

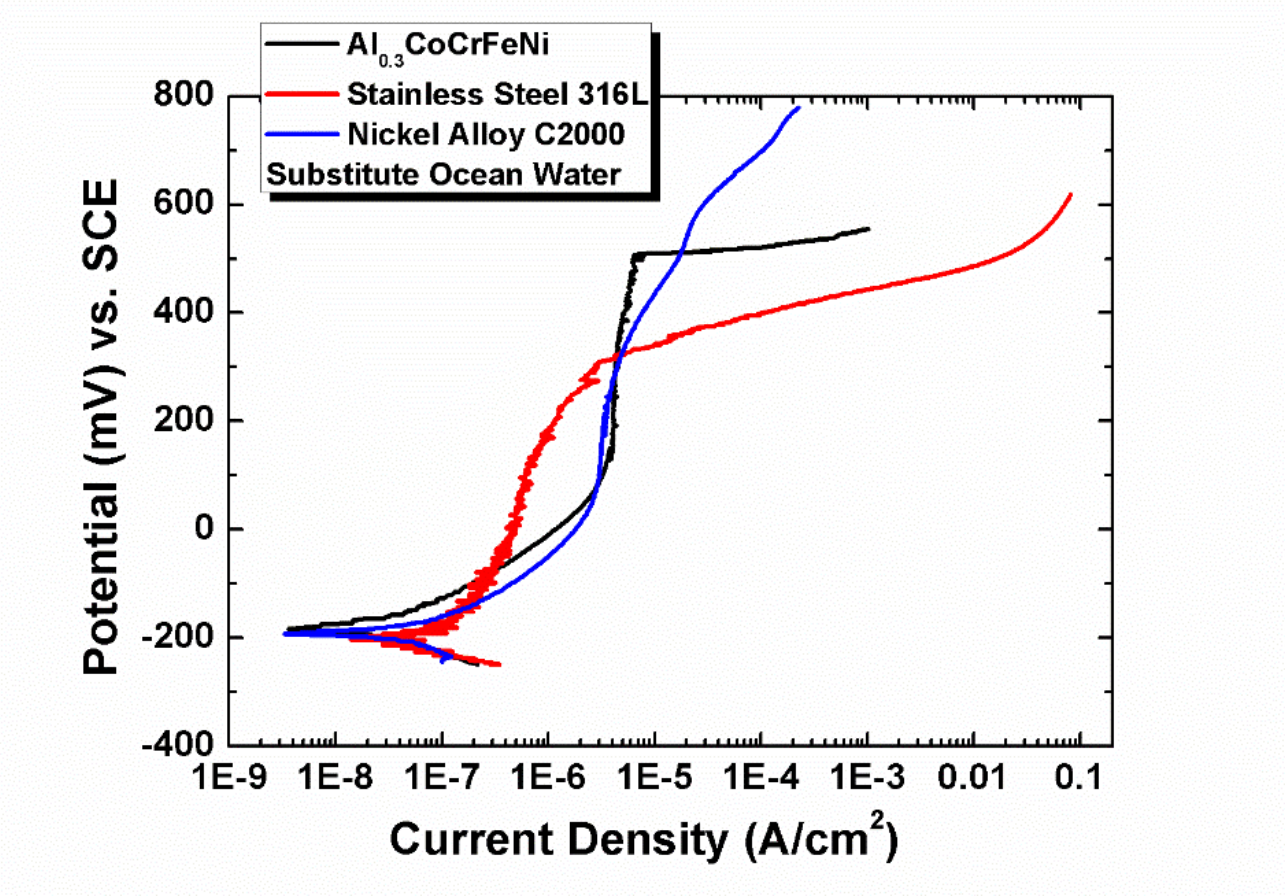

Figure 71. Anodic Polarization of the Al0.3CoCrFeNi alloy, 316L stainless steel, and C2000 nickel alloy

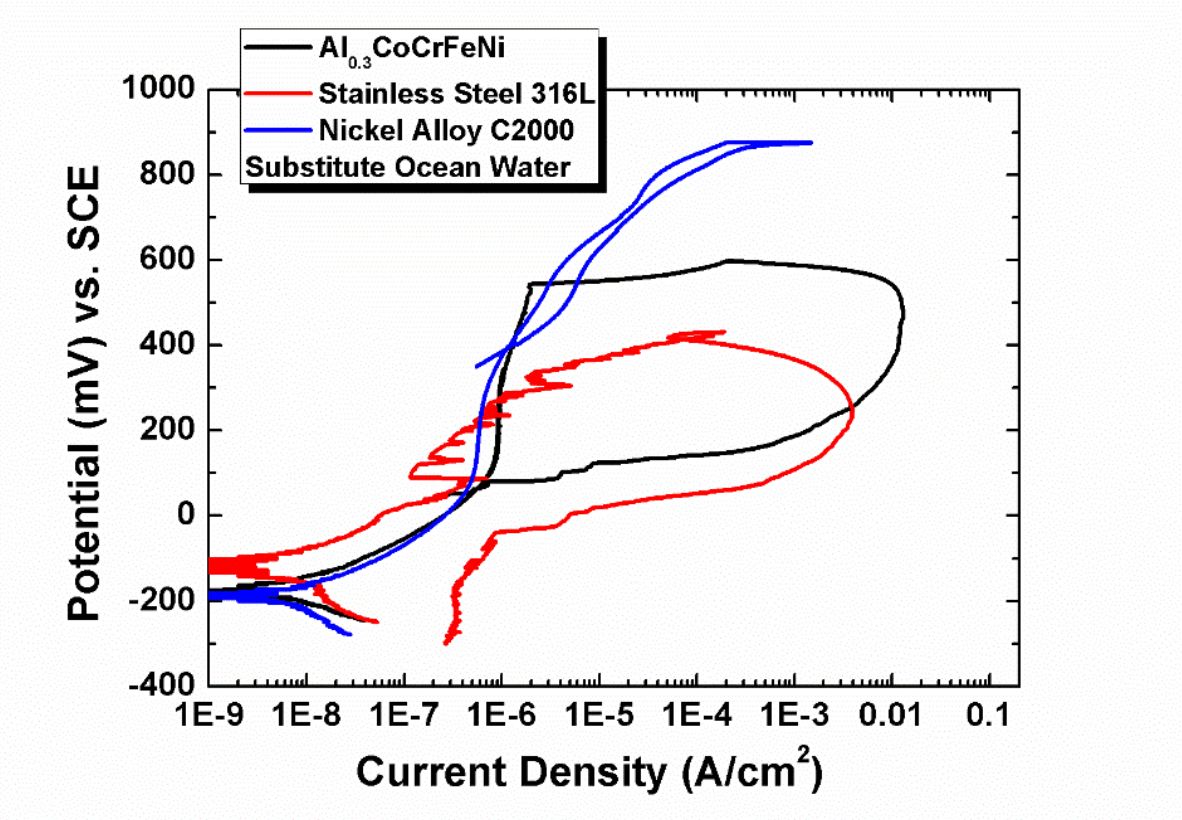

Figure 72. Cyclic Polarization of the Al0.3CoCrFeNi alloy, 316L stainless steel, and C2000 nickel alloy

Vita

Zhi Tang was born and grew up in the city of Changsha, Hunan Province, China. He graduated from the High School Attached to Hunan Normal University in July 2006. He graduated with a Bachelor of Science degree from the Department of Materials Science and Engineering at University of Science and Technology Beijing in July 2010. He came to the University of Tennessee, Knoxville, and enrolled in Materials Science and Engineering Department in August 2010. The Master of Science degree and the Doctor of Philosophy degree were received in December 2012 and December 2014, respectively.